Optical Design and Calibration of the Arctic Weather Satellite

Inaugural dissertation
of the Faculty of Science,
University of Bern

presented by

Roland Albers

from Oelde, Germany

Supervisors of the doctoral thesis: Dr. Axel Murk
Institute of Applied Physics

Optical Design and Calibration of the Arctic Weather Satellite

Inaugural dissertation
of the Faculty of Science,
University of Bern

presented by

Roland Albers

from Oelde, Germany

Supervisors of the doctoral thesis: Dr. Axel Murk
Institute of Applied Physics

Accepted by the Faculty of Science.

The Dean:

Bern, 29. November 2024 Prof. Dr. Jean-Louis Reymond

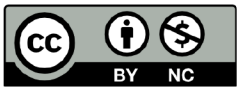

Summary

This thesis covers the quasi-optical design and calibration targets of the microwave radiometer on the Arctic Weather Satellite (AWS), which was launched on the 16th of August 2024. AWS is a prototype mission for a constellation called EUMETSAT Polar System Sterna (EPS-Sterna) consisting of 6 AWS models in 3 orbital planes which will be used operationally for numerical weather prediction (NWP). The radiometer operates in the 54, 89, 183 and 325 GHz bands in a cross-track scanning configuration.

While the lower three frequency bands are common to other operational radiometers currently flying, it is the first spaceborne instrument to provide sounding data at 325 GHz. Another novel feature of the instrument is the wedge shaped Onboard Calibration Target (OBCT) with a new epoxy based absorber mixture. It is also the first radiometer to use a feedcluster that is directly illuminating a cross-track scanning mirror, instead of the conventional approach of using a Quasi-Optical Network (QON) to co-align the antenna beams.

This approach allowed for a much more compact design at a lower cost compared to other microwave sounders, suitable for hosting on a smaller dedicated satellite platform and therefore enabling production in larger quantities for a constellation. However, this approach also introduced scan dependent performance variations, beam pointing offsets and elliptical beam contours, which need to be considered for the instrument calibration and accurate geolocation.

Chapter 1 contains a brief summary of relevant concepts enabling microwave radiometry and gives an overview of radiometer receivers. It is focussed on providing the background information for the rest of the thesis and can be skipped by readers familiar with the subject matter.

Chapter 2 describes the AWS mission in greater detail and puts it in context of other contemporary missions and the ultimate goal of the EPS-Sterna constellation. It also states the thesis objectives and shows first light data of the instrument from orbit.

A detailed overview of the quasi-optics is provided in Chapter 3. The quasi-optics were simulated using the TICRA Tools software and this chapter elaborates on the output from the simulations. Firstly, the optimisation efforts of each component using Physical Optics (PO) simulations is described. The effect of the instrument structure is then considered by means of Method of Moments (MoM) simulations. The chapter ends with a presentation of the AWS farfield performance.

Chapter 4 covers the calibration of the AWS radiometer. It describes the OBCT as well as Onground Calibration Targets (OGCTs), which have been designed and manufactured at the Institute of Applied Physics (IAP). A discussion of their performance concerning return loss and thermal aspects is provided.

A conclusion of the thesis and recommendations for further work concerning the AWS quasi-optics is provided in Chapter 5, followed by the three peer-reviewed publications accompanying this thesis in Chapter 6.

FIGURE 1: The Arctic Weather Satellite Radiometer. Courtesy of OHB Sweden.

Contents

Introduction

1.1 Microwave Radiometry

This section provides a brief and non-exhaustive overview of the principles of microwave radiometry relevant to this thesis. For a more detailed and technical background the reader is directed to the books by Ulaby [1], Goldsmith [2] and Pozar [3].

1.1.1 Atmospheric emission spectra

Microwave radiometry is the measurement of electromagnetic radiation in or near the 0.3 - 300 GHz (λ = 1000 - 1 mm) band. In the context of atmospheric measurements from satellite it is radiation emitted or reflected by the earth's surface which is attenuated by the constituents of the atmosphere [1].

The attenuation is caused by a discrete energy transitions of the molecules. The three possible mechanisms for energy transitions are electronic, vibrational and rotational transitions. Absorption in the microwave frequency range are caused by rotational transitions of the molecule changing from a lower to a higher energy state. The absorbed frequency is a function of the quantised energy difference between the two states. The molecule can also undergo a rotational transition to a lower energy state by emitting this energy difference. For a single molecule in isolation, each transition corresponds to a discrete frequency, or so called absorption line. In practice, the molecule is interacting with its surrounding which broadens the absorption line. There are a number of broadening mechanisms, but the most relevant for atmospheric measurements is pressure broadening. Pressure broadening occurs due to the collision between molecules, which reduce or increase the energy of the rotational transition. Consequently, the absorption line is broadened which can be expressed by a Lorentzian profile. Since the vertical pressure profile of the atmosphere is known this broadening can be used to retrieve information of the vertical structure of the atmosphere. Another broadening mechanism is caused by the movement of the molecule relative to the observer which induces a doppler shift of the absorption line. Since real measurements observe a very large number of molecules with different movements, the absorption line is broadened by a Maxwell-Boltzmann distribution. Although doppler broadening depends on the temperature of the molecule and therefore varies as a function of altitude, the temperature variation is small and therefore doppler broadening variations throughout the atmosphere are small.

Since the atmosphere is not homogenous, the magnitude and shape of the absorption lines change along the path from the surface to the satellite. Furthermore, the atmospheric constituents emit thermal radiation themselves which is attenuated along the path to the satellite. The superposition of the various aforementioned effects from different transitions and molecules is called the emission spectrum. A frequency range in the spectrum where there is very little to no attenuation by the atmosphere is called an atmospheric window and enables direct measurements of the thermal radiance of the earth's surface.

Figure 1.1 shows the simulated emission spectrum over the Arctic Weather Satellite (AWS) frequency range for a satellite looking nadir, meaning the viewing angle is perpendicular to the atmosphere. The emission spectrum was simulated using the Atmospheric Radiative Transfer Simulator (ARTS) [4, 5]. The dominant features in the spectrum originate from O_2 [6] and H_2O [7, 8], but other species also contribute to the spectrum. The shaded areas mark the frequency bands covered by the AWS microwave radiometer.

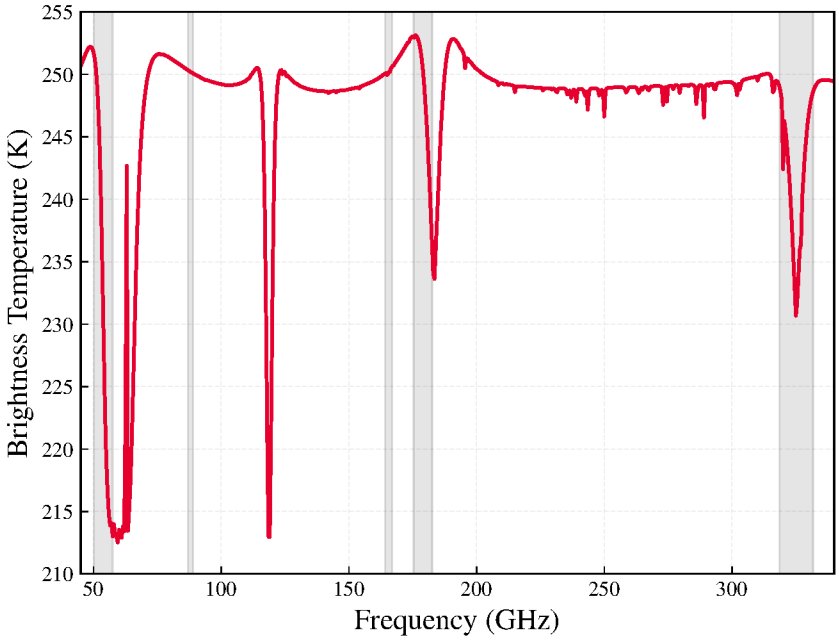

FIGURE 1.1: Emission spectrum covering the Arctic Weather Satellite bands (marked in grey) looking down on a forest with emissivity 0.9 simulated by ARTS.

1.1.2 Brightness temperature

The measured quantity by a microwave radiometer is the radiance I_f, which is the intensity received per steradian and area for a given frequency f. It is usually expressed as a brightness temperature T_B, which is equivalent to the physical temperature T a blackbody would have for a given radiance. A blackbody, as defined by Kirchhoff, is an idealised object with complete absorption. For the blackbody to remain in thermal equilibrium it has to also be a perfect emitter in order to shed the energy it absorbs. Planck's law describes the radiance emitted by a blackbody at a temperature T:

$$B_f(T) = \frac{2hf^3}{c^2} \cdot \frac{1}{e^{\frac{hf}{kT}} - 1} \tag{1.1}$$

where c is the speed of light, h is Planck's constant and k is Boltzmann's constant. The brightness temperature is defined as:

$$T_B = B_f^{-1}(I_f) \tag{1.2}$$

The Planck function acts as a non-linear scaling factor of the the radiance, converting it to a more intuitive value for everyday use. A common approximation is the Rayleigh-Jeans brightness temperature equivalent which is defined as

$$T_B^{RJ} = \frac{c^2}{2f^2k} \cdot I_f \qquad \text{for} \quad hf \lll kT \tag{1.3}$$

However, this approximation only holds true for certain frequency and temperature ranges. A comparison is presented in Figure 1.2. The solid lines are radiances emitted by a blackbody of a specific physical temperature according to Planck's law. The chosen temperatures correspond to relevant temperatures for the calibration and scene temperatures of the AWS radiometer and the frequency range (x-axis) covers the complete AWS bands. The dashed lines are the offsets in brightness temperature T_B using the Rayleigh-Jeans approximation to the physical temperatures of the blackbody. As a general trend, the brightness temperature error increases with frequency.

At very cold temperatures (e.g. cold space at 3 K) Rayleigh-Jeans is not an appropriate approximation. The absolute error looks smaller than at higher temperatures but is in fact already 33% at the lowest AWS frequency, increasing to >99% at 325 GHz. At higher physical temperatures the absolute error seems comparable, but is higher for liquid nitrogen temperature (78 K) as a percentage error, than for 200 K and 300 K. For example, for 165 GHz the absolute offset is similar for all three physical temperatures but the percentage errors are very different at 5%, 2% and 1.3% for 78 K, 200 K and 300 K, respectively. On the whole, even at 50 GHz the absolute offset is >1 K and the Planck function should be used for radiance conversion for accurate measurements and calibration of the AWS radiometer.

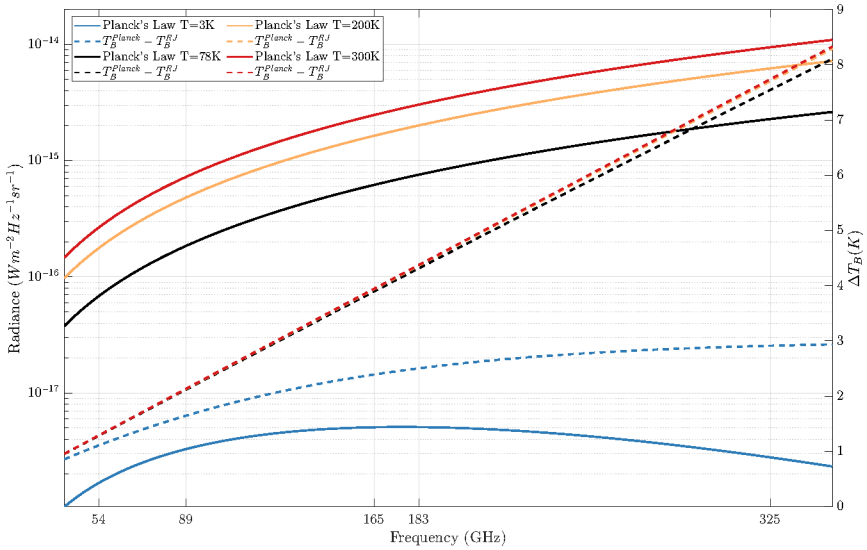

FIGURE 1.2: Radiances for a given physical temperature using Planck's law (left axis) and the absolute error in T_B using the Rayleigh-Jeans approximation (right axis) for AWS frequency range

It should be noted that most real objects or measured scenes such as the atmosphere do not behave like blackbodies and their measured brightness temperature does not correspond to a real physical temperature; They are said to behave like "greybodies". Their measured brightness temperature can also be distorted by other effects such as scattering, transmission through the object or non-thermal sources of radiation.

1.2 Total power microwave radiometers

Microwave radiometers are sensitive receivers designed to measure a weak signal originating from thermal electromagnetic radiation of a medium. They have a number of advantages over

other means of atmospheric measurements. They are part of a family of instruments which are able to measure atmospheric variables from great distances, which are called remote sensing instruments. They do not require any specific conditions such as daytime or clear sky to perform their measurements [9]. The atmospheric variables that can be retrieved using radiometry such as temperature and water vapour content have a high impact on numerical weather prediction (NWP) [10, 11]. A radiometer system can broadly be split into three parts, which are: the quasi-optics, front-end and back-end of the receiver. This thesis focuses on the optics, but a brief description of AWS relevant architecture of the front- and back-end is provided in the following paragraphs, accompanied by the sketches Figure 1.3.

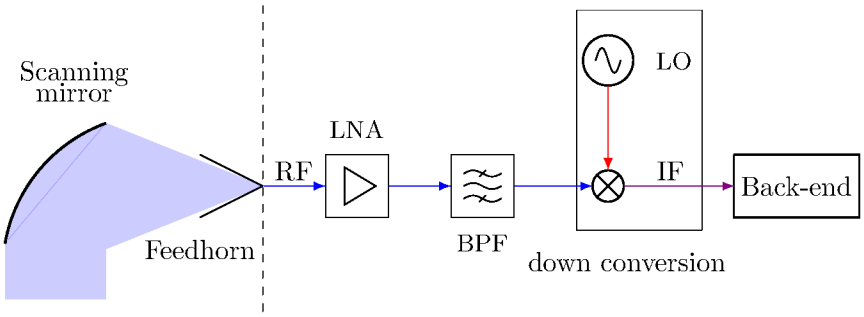

FIGURE 1.3: Sketch of radiometer receiver

1.2.1 Radiometer receivers

The front-end begins at the antenna of the radiometer, which captures the thermal electromagnetic radiation directed into it by the quasi-optics. Typically a high gain antenna design is used; most commonly a feedhorn antenna. Since the signal is very weak, it needs to be amplified while minimising additional thermal noise from the antenna, other components or the amplifier itself. An appropriately named low noise amplifier (LNA) is the first component after the feedhorn for this purpose. After the LNA, the broadband signal is limited by a bandpass filter (BPF) to the frequency range relevant for the measurement. Depending on the available components this signal can be fed directly into the back-end, where it is processed further. However, it is often necessary or desirable to downconvert the original radio frequency (RF) signal to an intermediate frequency (IF) using a mixer. The mixer convolves the RF band signal with an additional local oscillator (LO) single frequency signal synthesised in the instrument. The outgoing IF signal due to the is:

$$\begin{aligned} f_{IF_1} &= f_{RF} - f_{LO} \\ f_{IF_2} &= f_{RF} + f_{LO} \end{aligned} \tag{1.4}$$

The two outgoing frequencies are called the lower sideband (LSB) and upper sideband (USB). By including a low pass filter behind the downconversion stage, the undesirable LSB is eliminated and the receiver is operated as single sideband (SSB). For the purposes of down-conversion, the chosen f_{LO} should be relative close to, but smaller than the measured frequency band f_{RF}. One disadvantage of this method is that it might not be possible to cover both wings of an absorption line of the chosen RF band, since it is too broadband.

One method to measure both sides of an absorption line with a single LO signal is to use a double sideband (DSB) receiver. For this downconversion architecture the LO frequency is fixed at the absorption line center and the resulting IF band is

$$f_{IF} = f_{RF_{usb}} - f_{LO}$$

$$f_{IF} = f_{LO} - f_{RF_{lsb}} \tag{1.5}$$

resulting in the two wing spectra being in superposition in the same IF band. The downside of this method is that the line center is eliminated and only information about the line wings remain. A common feature of both approaches is that the non-linear diodes in the mixers generate not only the desired frequencies listed in Equations (1.4) and (1.5), but harmonics of f_{LO}, f_{RF}, f_{IF} and their sums etc. Some mixers are designed to exploit this and are optimised to produce a strong $2f_{LO}$ signal, enabling downconversion of higher RF frequencies; they are called subharmonic mixers. The downside of this intrinsic property of the mixers is that undesirable harmonics can propagate through the receiver and show up in measurement channels. Especially for multi-band instruments such as AWS the f_{LO} signals need to be carefully chosen to avoid this issue.

A third approach is to skip the downconversion and feed the RF signal straight into the backend. The direct detection approach often requires an additional amplifier, since it is lacking the amplification provided by the downconversion from the LO signal. Designing the frontend architecture of a radiometer is often a trade-off between cost and availability of components. High frequency LNA or conventional amplifiers may not be available at all or not compatible with the desired bandwidth. Alternatively, backend components might be deciding factor if direct detection is feasible.

Radiometer back-end

The back-end finally converts the measured signal into a voltage using a power-meter which is subsequently converted by the analogue-to-digital converter (ADC) to a digital quantity often expressed in counts. If the IF is not processed further, the power-meter simply measures the total power in the entire band. However, a lot of information is lost in this approach, especially when the measured band covers a line wing and not just a peak. One approach to gain more resolution within the band is to split the IF signal up into channels within the band. Each channel will have its own BPF to reduce the signal down to a subsection of the band and a power-meter behind it to measure the total power in the channel. It should be noted that the intensity of the signal actually arriving at the power-meter, called the system noise temperature T_{Sys}, is the power delivered by the feedhorn antenna T_A with the addition of the noise added by the components in the receiver. The receiver noise power P_{Rec}, which is in part thermal noise but also based on other effects that won't be discussed here, can conveniently also be expressed as an equivalent temperature T_{Rec}:

$$P_{Rec} = k \cdot T_{Rec} \cdot B \tag{1.6}$$

Where B is the bandwidth of the signal. Both T_A and T_{Rec} are noisy signals so a radiometer cannot take an instantaneous measurement to assess the true signal. Instead the signal is integrated over a certain time period τ to average out the noise. For an ideal total power radiometer, the statistically minimum detectable change can be defined as:

$$\Delta T = \frac{T_{Sys}}{\sqrt{B\tau}} = \frac{T_A + T_{Rec}}{\sqrt{B\tau}} \tag{1.7}$$

However, for a real instrument there are other factors to consider, such as gain variations $\frac{\Delta G}{G}$ in the receiver components and the number of calibration samples N and their integration time τ_c, which leads to the following definition for the noise equivalent radiometric sensitivity $NE\Delta T$ used by European Space Agency (ESA) [12]:

$$NE\Delta T = T_{Sys}\sqrt{\left(\frac{1}{B\tau}\right) + \left(\frac{\Delta G}{G}\right)^2 + \left(\frac{1}{BN\tau_c}\right)} \tag{1.8}$$

This is a key performance criteria for radiometers and specified as a requirement for the design.

1.2.2 Radiometer quasi-optics

The term quasi-optics refers to the regime where the width of a collimated beam is a relatively small number of wavelengths [2]. Consequently, the quasi-optical elements interacting with the beam will be similarly sized. This leads to diffraction effects affecting the quasi-optical system and pure ray-tracing is no longer appropriate to simulate the propagation of the beam. Instead, idealised gaussian beams can be used as a first approximation for the design of a Quasi-Optical Network (QON).

However, a gaussian beam is an idealised antenna pattern which is not realistic. In Figure 1.4 a two-dimensional gaussian antenna beam (blue) emitted from a feedhorn antenna is compared to a more realistic antenna pattern shown in red. The radius of the curves express the amount of gain of the antenna pattern in that radial direction. A gaussian beam can be designed to have close to all of its gain in the angular range covered by the reflector, which would be the intended mainbeam. But a real antenna pattern will always have sidelobes either side of the mainbeam (shown in red) and backlobes which point towards the rear of the antenna (not shown in sketch). Since not all of the antenna pattern is concentrated on the reflector, the gain in the mainbeam has to decrease. The part of the antenna pattern that is not illuminating the intended element is called the spillover and is the region in light red. Since all real antenna patterns have sidelobes, it is impossible to completely avoid spillover. Spillover is expressed as the fraction of the power in the antenna pattern not illuminating the intended optical element and presented as a percentage of the total power in the antenna pattern.

Spillover is especially detrimental to a radiometer since the power of the received signal from the atmosphere is low and additional radiances from e.g. the spacecraft structure or cold space degrade the signal to noise ratio. For an antenna in transmission spillover is of course still a concern but a less significant issue since the power of the signal is significantly higher.

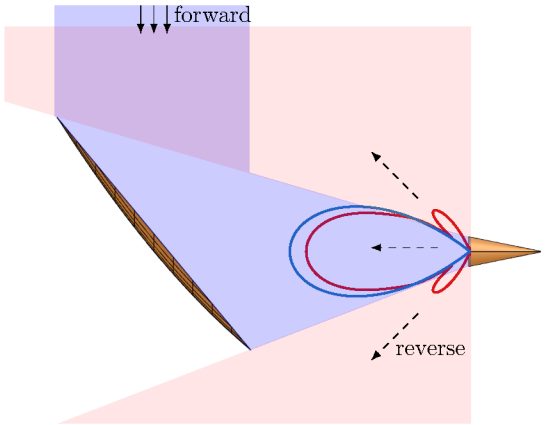

FIGURE 1.4: Sketch of gaussian beam vs beam with sidelobes and reflector illumination.

Reciprocity

An important concept for the design of quasi-optics and antennas in general is reciprocity. In real use the radiometer is using e.g. a reflector to focus the signal from the atmosphere into the feedhorn antenna, which is also receiving unwanted signals from its surroundings due to spillover; this is called the forward mode [2]. However, when laying out quasi-optics using

gaussian beams or using software packages such as TICRA Tools, the antenna is assumed to be in transmission and emitting a signal onto its surroundings and illuminating the reflector which is then redirected onto the atmosphere. Another way to phrase it is, that the transmitting is actually a time reversal of the forward mode and is hence called the reverse mode. Reverse mode is more intuitive and straightforward as it only requires projecting the antenna pattern of the receiving antenna onto its environment. The arrow annotations in Figure 1.4 highlight the directions of the signal for forward and reverse mode. In Chapter 3 it is implicit that the design is carried out in reverse mode.

Quasi-optical components

With respect to spaceborne radiometers, the need for quasi-optics arises from the restricted space and the wide frequency spacing required. There is no possibility to cover e.g. the complete AWS frequency range using a single feedhorn antenna. Therefore separate antennas and receiver chains are required. The knock-on effect is that if each of these antennas had their own scan mirror they would also require individual calibration targets, motors for the mirrors etc. Irrespective of the above, it is also desirable to overlap all the bands for combined data products where e.g. a window channel might be used to flag if the current atmospheric scene is measured with a sea or land background. An advantage of QONs is that the beams are propagating in free space, which means minimal losses. The components typically also have very low insertion losses so there is very little attenuation from adding QON components, which is crucial due to the low signal power levels. A limited number of components are described here, which are relevant to the QON designs of spaceborne radiometer missions.

The most fundamental quasi-optical component is the reflector/mirror with both terms being used interchangeably. They can be used to collimate or focus the beam from the feedhorn antenna (reverse mode). A collimated beam is a beam which has minimum divergence as it propagates. This is desirable for a radiometer, since a collimated beam will have the consistently smallest spot size for any altitude in the atmosphere. The curvature of the reflector determines the effect it has on the beam. A parabolic curvature (such as in Figure 1.4) will collimate the incident beam, as long as the phase center of the beam is positioned in the focal point of the parabola. An elliptical mirror has two focal points and will focus the beam emitted from one focal point onto the other focal point. The focused beam rapidly expands after reaching the focal point. This can be a useful feature for temporarily reducing the beam diameter inside the QON for other elements. Similar effects can be achieved with lenses, but they are not relevant for the systems discussed in this thesis. A sequence of mirrors can be designed to be frequency independent, guaranteeing a consistent collimated beamwidth exiting the final mirror. Reflectors can be made of any material that is a good electrical conductor or can be coated with one.

In order to co-align several beams for different antennas, further components are necessary. Frequency selective surfaces (FFSs) change their behaviour depending on whether the incident beam is above/below a certain cut-off frequency or inside/outside a band [13]. They consist of periodic metallic structures in a dielectric substrate which are designed and tuned to either act in transmission or reflection, both with minimal losses. However, they are not a universal solution and performance varies depending on e.g. incidence angle and frequency range often requiring custom solutions per use case. A flat reflector made from a FFS can have an antenna positioned behind it, transmitting its beam through the FFS at the same angle as another beam of a different frequency reflecting of the surface. They are then co-aligned on the next component in the QON.

Another method of co-aligning two beams is the use of polarising grids. They consist of a frame around which conductive wires a wound at a precise spacing. The spacing and the

diameter of the wires should be significantly smaller than the wavelength of the highest frequency in the relevant frequency range [14]. If this is the case, the grid will act as a reflector for any electric field which is polarised parallel to the wire orientation, while transmitting the electric field which is polarised perpendicular to the wire orientation. With regard to beam co-alignment, it can be used in the same configuration as an FFS, provided the two beams have orthogonal polarisations. The obvious disadvantage being that this method can only be used if it is sufficient to measure those particular bands in a single polarisation.

1.3 Space based radiometers

This section provides a short overview of some relevant missions and their quasi-optics setup in the context of AWS. A distinction can be made between missions which are used for everyday weather forecasting (used operationally) and missions which are technology pathfinders and scientific missions. Radiometers typically include a rotating mirror for scanning the earth and atmosphere in order to increase the coverage of the instrument. There are two overall design architectures for scanning mirrors into which the missions are divided; cross-track scanning and conical scanning radiometers[15].

1.3.1 Cross-track scanning

For cross-track scanning the scanning mirror is an off-axis parabolic reflector rotating independently of the rest of the antenna or quasi-optics. The rotation axis of the mirror is parallel to the flight direction of the satellite, also called the flight track direction, as seen in Figure 1.5. Consequently, the scan plane of the reflector is perpendicular to the flight direction, scanning across the flight track. This geometry results in a wide swath covered in a single scan rotation, but comes with two trade-offs. Firstly, due to projection effects the footprint of the beam changes with scan angle θ_{sc} and deforms from an ideal circular beam in nadir to a wide ellipse. For an idealised spherical earth, the distance to ground and therefore the overall footprint size also increases since the earth is curving away from the satellite. Requirements on footprint size, beam symmetricity, mainbeam efficiency etc. for cross-track scanning radiometers are typically stated for nadir scan angle only. The second disadvantage is that the orientation of the beam polarisation will change relative to ground along the swath as a function of θ_{sc}. This architecture is not usable if the polarisation should be consistent between measurements.

1.3.2 Conical scanning

For conical scanners, the antennas/quasi-optics usually rotate with the parabolic scanning mirror so there is no relative movement between the two. The beam is reflected towards earth at a fixed angle, unchanging during the full scan rotation. The incidence angle dictates the radius of the scan circle and hence the width of the swath (see Figure 1.6). There is a trade-off between the width of the swath and the deformation of the beam footprint due to projection effects, but in general the swath width will be less than that of a cross-track scanning radiometer. However, the footprint geometry and polarisation orientation will remain constant for all scan angles.

1.3.3 Advanced Technology Microwave Sounder

The Advanced Technology Microwave Sounder (ATMS) is the American state of the art radiometer, currently in operational use by National Oceanic and Atmospheric Administration (NOAA). There are currently 3 ATMS used operationally in orbit [16]. It shares common

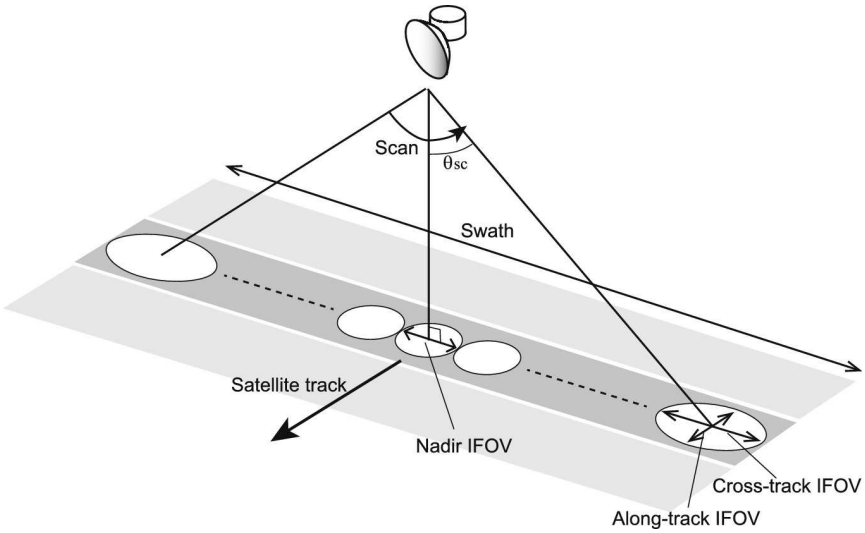

FIGURE 1.5: Sketch of crosstrack scanning geometry. Reproduced with permission from Springer Nature [15].

channels with its predecessor Advanced Microwave Sounding Unit (AMSU) [17], covering a frequency range from 23.8 to 183.3 GHz separated into 22 channels using 4 feedhorns. It uses two sets of compact QON with identical architectures [18]. The two low frequency horns (24-31 GHz and 54 GHz) form the first set and are co-aligned onto a static off-axis parabolic reflector by means of a polarising grid (see Figure 1.7). The scanning is achieved by a flat reflector which covers the earth swath, cold space and an internal view towards a hot calibration target. The calibration target consists of a pyramidal array and is positioned in the zenith view of the instrument. The same architecture is mirrored for the two high frequency horns (89 GHz and 165-183 GHz) with their own dedicated scanning mirror, sitting "back to back" with the other scanning mirror. A second calibration target is included for this QON, also positioned in zenith. The two scanning mirrors are driven by the same motor and synchronised, meaning although there is a small offset between the two scanning mirrors, the footprints practically overlap. The beam footprints are 75, 32 and 16 km for the 24-31, 50-90 and 165-183 GHz channels respectively.

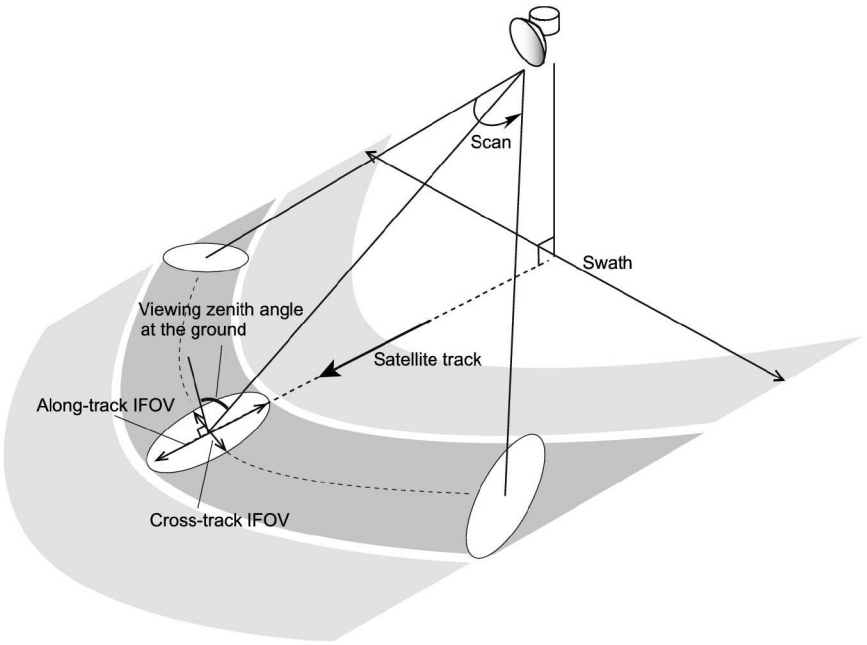

FIGURE 1.6: Sketch of conical scanning geometry. Reproduced with permission from Springer Nature [15].

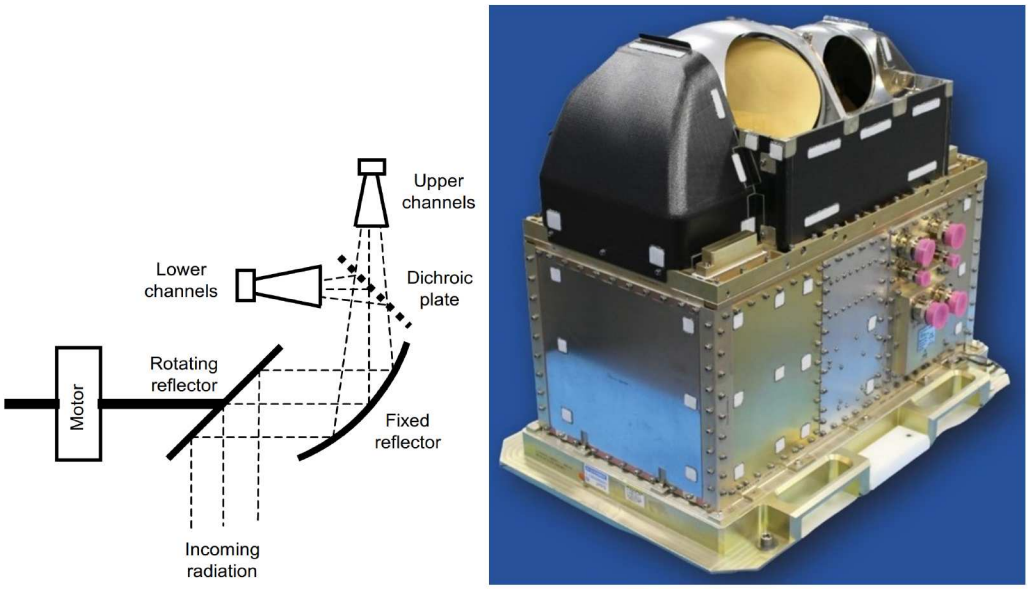

FIGURE 1.7: Sketch of one set of ATMS quasi-optics (left) [19]. Picture of ATMS instrument (right). Retrieved from
https://www.northropgrumman.com/space/advanced-technology-microwave-sounder

1.3.4 Instruments similar to ATMS

The ATMS design (or a very similar architecture) is used for a number of instruments which are briefly mentioned here. The ATMS predecessor is AMSU, which actually consisted of several modules called AMSU-A1, AMSU-A2 and AMSU-B [17] which together covered the ATMS frequency range. The early models A1 and A2 used dedicated parabolic mirrors and calibration targets per feedhorn and AMSU-B along with later derivatives such as the Chinese built Micro-Wave Humidity Sounder (MWHS) 1 and 2 for Fēngyún-3 (FY-3) [20] use the

ATMS approach of polarising grids or FFSs to co-align at least two feedhorns, reducing the overall instrument volume.

1.3.5 Microwave Sounder from MetOp-SG

The Microwave Sounder (MWS) is part of the primary mission Meteorological Operational Satellite - Second Generation (METOP-SG) for the EUMETSAT Polar System (EPS) [21]. It is the current European state of the art radiometer, due to launch in 2025 for operational use. It covers a frequency range from 23.8 to 229 GHz separated into 24 channels using 6 feedhorn antennas. A seventh horn provides redundancy for the 54 GHz channels at orthogonal polarisation. Figure 1.8 shows the elaborate QON used to co-align all beams onto the final static parabolic mirror. The pictured assembly without the final mirror has a footprint of approximately 1 m^2. Not pictured is the additional flat scanning mirror with a 35 cm diameter sitting below (towards the bottom of the image) the parabolic mirror. The nadir direction is out of page in the image and the calibration target is located below the scanning mirror (direction into the page). The calibration target consists of a pyramidal array with epoxy based absorber and is used in combination with cold space measurements [22]. Beam co-alignment is achieved by a series of polarising grids and high/low-pass FFSs, meaning not all channels have identical polarisation. The beam footprints are 40, 20 and 17 km for the 24-31, 54 and 89-229 GHz ranges, respectively.

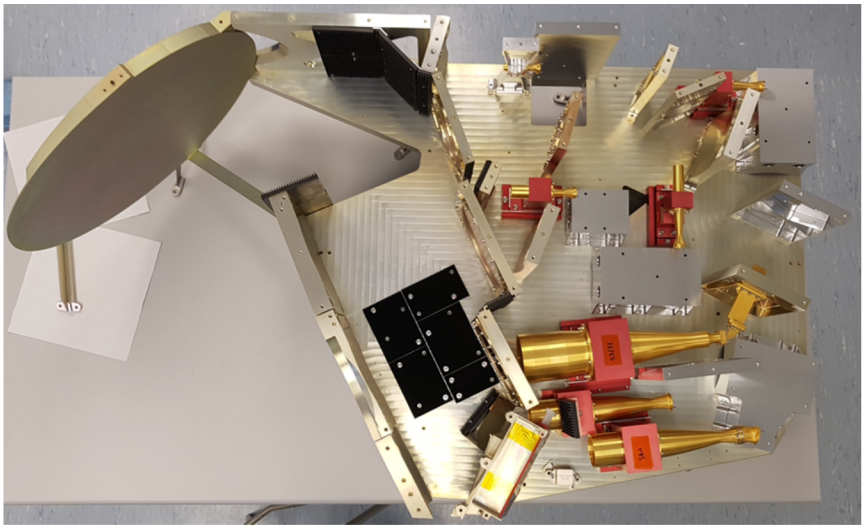

FIGURE 1.8: Image of MWS quasi-optical network. Courtesy of Adam Woodcraft, Thomas Keating Ltd.

1.3.6 Ice Cloud Imager from MetOp-SG

The Ice Cloud Imager (ICI) is also part of the METOP-SG programme for operational use and pushes to higher frequency bands in order to measure ice cloud properties [23]. It covers a frequency range from 183 to 664 GHz in 11 channels using 7 horns. The lowest channel is common with the convential cross-track scanning sounders, but the higher frequency bands at 243, 325, 448 and 664 GHz are novel additions. The 7 horns are not co-aligned, as is done for cross-track scanning radiometers, but are positioned adjacent to each other in two rows directly illuminating the scan mirror. The feedcluster is hidden in the front-end box in Figure 1.9, pointing downwards at the main reflector, which is static relative to the feedhorns. Instead, the entire structure inside the annular shield rotates and illuminates earth (upwards in picture) only for the arc defined by the cut-out in the shield. For cold calibration the

feedcluster scans across another mirror during its rotation, diverting the beams towards cold space. Another part of the rotation arc inside the instrument is used to cover a hot calibration target consisting of pyramidal arrays with epoxy based absorber [22]. Since there are no polarising grids or other quasi-optical components, any feedhorn could also be used in dual polarisation but this is only done for 2 channels (243 and 664 GHz). The footprints for each beam are all approximately 15 km and elliptical due to the scan incidence angle.

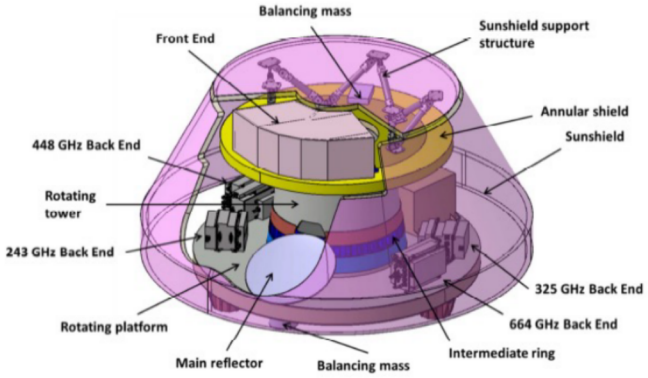

FIGURE 1.9: Annotated model of ICI instrument. Courtesy of Airbus Defence and Space, Spain.

1.4 Calibration of a total power radiometer

There are different approaches to calibrating a radiometer, but the most common method is by using a two point hot/cold calibration [17, 21, 24, 19]. It involves measuring the power received by the radiometer while looking at two known sources at different brightness temperatures before measuring a third unknown source or "scene". It requires knowledge of the brightness temperature of the two sources. Typically, one source is at a brightness temperature (T_c) lower than the bottom end of the anticipated measurement range, also called the "cold" point. The second calibration source should be at a brightness temperature T_h warmer than the measurement range. The power measured in the receiver (P_c, P_h) for these two sources is assumed to be scaling linearly, meaning the gain of the receiver is assumed to be constant for any measured T. For real radiometers non-linearity is a common issue but it will be disregarded for the purposes of this section.

Using the two calibration measurements, the scene temperature T_{sc} from a third measurement can be calculated using

$$P_{sc} = G_s \cdot T_{sc} + G_s \cdot T_{Rec} \tag{1.9}$$

where

$$G_s = \frac{P_h - P_c}{T_h - T_c} \tag{1.10}$$

$$T_{Rec} = \frac{P_c T_h - P_h T_c}{P_h - P_c} \tag{1.11}$$

The system gain factor G_s includes the receiver power gain and signal bandwidth and acts like a scaling factor between brightness temperature and power. For calibration it is assumed that both G_s and T_{Rec} are constant while the three measurements are taken.

However, there is another source of uncertainty which is the subject of this thesis; the knowledge of the true brightness temperature received by the antenna, which can be subject to a number of errors. Figure 1.10 is a general plot of the two point calibration method, where a symbolic error term ΔT is introduced. The grey area highlights the anticipated temperature range. The red shaded area expresses the error bound due to an error in the temperature measurement for the cold or hot target. A particular measured scene power can result in a range of calculated scene temperatures within the red box. Therefore, the accuracy of the instrument depends on minimising this uncertainty.

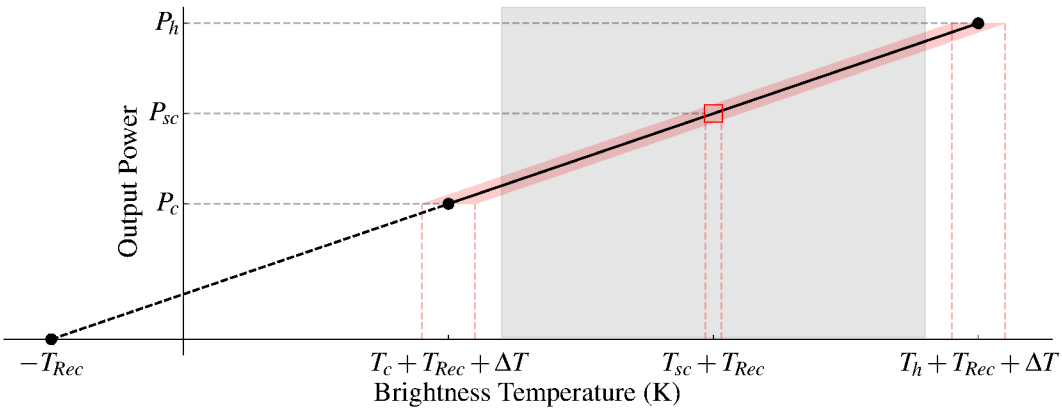

FIGURE 1.10: General schematic of hot/cold calibration scheme. The grey area shows range of possible scene temperatures.

The uncertainty contributions can be divided into either electromagnetic or thermal origin. The ideal case would be a perfect blackbody source at a known physical temperature with perfect coupling to the antenna. However, the materials used to emulate a blackbody have less than perfect absorption and therefore a reflectivity $r > 0$ and emissivity $\varepsilon < 1$. When a signal with power P_{in} is emitted into a calibration target and $\varepsilon < 1$, a reflection with power P_{refl} will occur. The attenuation of the reflected signal is called the return loss and defined as [25]:

$$\text{Return loss} = -20\log_{10}|\rho| = 10\log_{10}\left(\frac{P_{\text{in}}}{P_{\text{refl}}}\right) \tag{1.12}$$

where ρ is the complex reflection coefficient. This is the commonly accepted performance measurement of a calibration target. Often the term $|S_{11}|$ is also used, which is defined as $-\text{RL}$. Return loss/$|S_{11}|$ is not a direct measurement of the emissivity of the target. If the majority of the reflected power is scattered and not captured by the device measuring the reflection than the return loss of the target appears to be high, but the target emissivity could be very low. Only if the test setup takes this into account does a high return loss indicate that the calibration target behaviour is close to that of a blackbody.

Figure 1.11 is an illustration of a feedhorn antenna with imperfect coupling into a calibration target. One issue during this measurement is that the received radiance can reflect within the receiver due to an impedance mismatch and a standing wave forms between the two elements (shown in blue). Depending on the distance between the calibration target and the antenna, this standing wave is in constructive or destructive superposition of the specular reflection, changing the apparent brightness temperature of the target. This can be accounted for by changing the length of the path between the target and antenna by $\lambda/4$ and then taking the mean of the two positions.

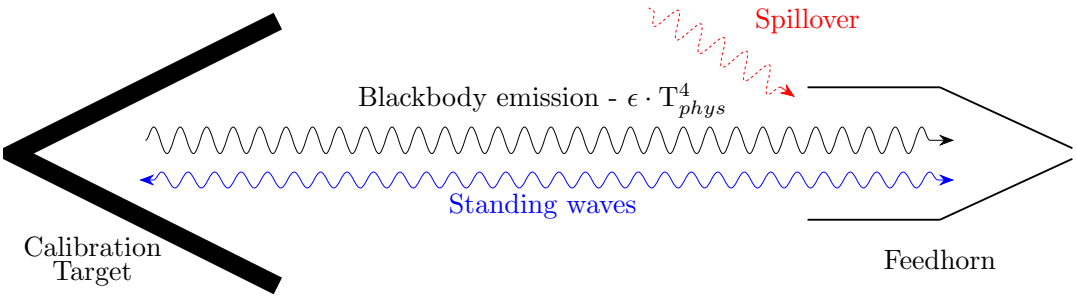

FIGURE 1.11: Sketch of a calibration target measurement.

Furthermore, the coupling between the antenna and calibration target is not 100% for a real antenna pattern and the environment also couples directly into the antenna (shown in red). This is the same as the spillover effects discussed in the previous section.

These effects will cause a discrepancy between the assumed brightness temperature for the hot or cold calibration target and the measured brightness temperature. The magnitude of the error depends on the brightness temperature difference between the calibration target and the antenna or the environment.

Thermal uncertainties arise from the accuracy of the physical temperature measurement of the calibration target. The sensors used to measure temperature accurately are metallic and cannot be potted inside the absorber itself as they would negatively impact the performance of the target. They are usually bonded to the substrate holding the absorber. Inevitably, there is a thermal gradient between the sensor position and the absorber which depends on the thermal conductivity of the materials involved.

Even if the thermal gradient between the sensors and absorber is negligible, the target temperature is often not homogenous. Common causes of induced temperature gradients are infrared (IR) radiative coupling or thermal gradients on the mounting interface. If the temperature of the target cannot be assumed to be homogenous, it requires comprehensive spatial temperature sampling across the target and precise knowledge of where the absorption occurs to calculate a more accurate brightness temperature. Lastly, the accuracy of the temperature sensor affects the radiometric measurement. The typical high accuracy temperature sensor used is an Resistance Temperature Detector (RTD) which are procured to certain standards often based on the Callendar Van-Dusen equation [26, 27]. This equation describes the relationship of the sensors resistance to its temperature using two polynomials for temperatures above and below 0 °C. Crucially, the uncertainty increases for very high or very low temperatures, assuming standard coefficients are used and no custom calibration was performed.

1.5 Common calibration target designs

There are a large variety of calibration target designs, which often depend on the precise application, frequency range and geometry of the instrument. This section is restricted to designs that are commonly used for meteorological radiometers in or near the AWS frequency range. Furthermore, a distinction should be made between ground-based and spaceborne calibration targets as the design requirements are quite different. For calibration targets used in space there are more external restrictions such as volume, mass and power budgets of the satellite. Some common ground-based absorber materials are not suitable or more often not qualified for spaceflight.

1.5.1 Cold calibration targets

Most designs for a ground-based cold calibration target are liquid nitrogen (LN_2) based [28, 29, 30], which has a boil-off temperature of about 77 K conveniently below the measured atmospheric brightness temperature range for a downward looking microwave radiometer. As long as the environmental pressure is kept constant, the LN_2 will stay at a constant predictable temperature. Another advantage is the availability of LN_2, since it is commonly used for cryogenic cooling in other applications. LN_2 provides little absorption and is only used to cool the absorber material of choice. The driving criteria here is the ability of the absorber material to survive frequent cryogenic temperature cycling.

Foam based absorber is not very affected by temperature shocks and can be directly immersed in an LN_2 bath. The foam is porous, ensuring a uniform temperature distribution since it soaked in LN_2. It is a simple low-cost approach. The disadvantage of this design is that the air/LN_2 interface above the absorber will produce an additional reflection, which will cause a standing wave if the surface is perpendicular to the incidence angle. This standing wave can produce a brightness temperature error of more than 1 K [31]. As the LN_2 boils off the characteristics of the standing wave will change. Furthermore, the uncontained boil-off of the LN_2 makes this concept unusable in vacuum chambers.

Another approach is to use epoxy based absorber bonded to a metal with high thermal conductivity. Here the absorber is not immersed in the LN_2 but cooled indirectly by bringing the metal in contact with LN_2 by e.g. pumping it through cooling channels in the metal. This avoids the LN_2 surface induced reflection. However, the absorber temperature will not be identical to the LN_2 temperature and RTDs bonded to the metal, therefore thermal simulations will be required to determine the true temperature of the absorber. This concept requires significant engineering effort for the piping, temperature monitoring and control, but is vacuum compatible .

For calibration in space, the most common cold calibration method is to observe the cosmic microwave background or "cold space". Its a well understood natural feature of a known brightness temperature. From a system level perspective, it is ideal since it only requires the instrument scanning mechanism to be able to point to cold space and no additional mass, volume and power is required.

1.5.2 Hot calibration targets

For ground-based hot targets the simplest solution is to use an "ambient" target that is floating at the temperature of the laboratory environment. Assuming room temperature, a hot calibration point at ≈300 K is warmer than the brightness temperatures found in the atmosphere. Foam based absorber is a good choice in ambient conditions as it is cheap and readily available. But its low thermal heat capacity makes it more susceptible to drafts, air-conditioning or cold targets positioned near the ambient target inducing temperature gradients. Therefore some insulation is still necessary.

For testing in vacuum, an epoxy based absorber on metal is preferred for the same reasons as mentioned above. In this case, heaters need to be included and spread evenly across the metal to ensure a homogenous heating of the absorber. Additionally, control software is required to balance any gradients. Sometimes, the functionality of cooling and heating is combined in a variable temperature target. Variable temperature targets are used to emulate the scene brightness temperatures which the instrument will measure and are the most complex and costly.

In space, natural hot calibration sources are not as straightforward as for cold targets. Outside of earth, no warm feature like stars or planets would fill the antenna beam sufficiently. On earth the amazonian rainforest [32] has been considered, but this would only possible for window channels where the atmosphere does not completely attenuate the signal. Another potential natural calibration scene without atmospheric attenuation is the moon [33], but it proves to be difficult to model its brightness temperature correctly.

Therefore, radiometers typically include a warm Onboard Calibration Target (OBCT) to provide a second calibration source in addition to cold space. The absorber typically consists of an epoxy mixture bonded to metal and is mounted inside the instrument [22, 24, 19]. Mounting the OBCT inside the instrument prevents significant thermal gradients from sources outside the instrument. Cold space, earth and the sun will radiatively couple into the OBCT absorber and impose a significant gradient, which can also vary depending on the orbit [34]. Therefore the OBCT should be insulated from direct views of the instrument exterior as much as possible. This often conflicts with the limited space available inside the instrument and is always subject to trade-off. There is always a drive to reduce the size and mass of the OBCT as much as possible.

One option is to not use an OBCT at all and instead add a noise source electrically coupled to the receiver [35, 36, 37]. The downside of this method is that any spillover in the optics of the instrument will not be calibrated out. Furthermore, ramp up time and long term drift of the noise diodes used for this purpose needs to be considered.

1.5.3 Absorber geometry

For a physical target, most of the design trade-offs concern the geometry of the absorber cavity. From a system level perspective, the ideal absorber would be a thin, lightweight plate filling whatever aperture space is required based on the optical analysis. From a radiometric perspective, the thickness of the absorber is driven by the skin depth of the material for the lowest frequency of the radiometer. The skin depth δ_s is the propagation distance of an electromagnetic wave until its power has been attenuated by $1/e^2 \approx 14\%$. Skin depth depends

on the complex permittivity of the absorber material and the frequency of the propagating wave. The skin depth is calculated as

$$\delta_s = 1/\alpha \tag{1.13}$$

and

$$\alpha = k_1 \sqrt{\frac{\varepsilon_r'}{2}\left(\sqrt{1+\frac{\varepsilon_r''^2}{\varepsilon_r'}}-1\right)} \tag{1.14}$$

One skin depth distance δ_s does not to provide sufficient absorption. For a sense of scale, the AWS minimum return loss requirement is 50 dB or 0.001% which is equivalent to 5.856 times the skin depth. Table 1.1 shows the theoretical required absorber thickness to achieve this return loss for the AWS frequencies, using material properties of the AWS OBCT epoxy absorber.

TABLE 1.1: Required skin depths for 50 dB return loss in AWS frequencies.

Frequency (GHz)	54	89	183	325
$5.856\delta_s$ (mm)	37.0	22.5	11.0	6.1

However, this only considers the component of the incident wave that has transmitted into the absorber. Since these materials are imperfect blackbodies, there is a reflection at the surface. This reflection coefficient Γ is based on the complex permittivity ε_r of the absorber. Using the complex permittivity of the AWS OBCT absorber we obtain

$$\Gamma = \frac{\sqrt{\frac{1}{\varepsilon_r}}-1}{\sqrt{\frac{1}{\varepsilon_r}}+1} \approx -0.364 \tag{1.15}$$

meaning the surface reflection drives the return loss of the absorber. This is another challenging issue for epoxy absorber mixtures. To minimise the required thickness of the absorber the imaginary part of the permittivity ε_r'' should be as high as possible, but typical mixing materials increase the real part of the permittivity ε_r' as well which increases the reflectivity.

The solution for high return loss absorber is to increase the amount of reflections on the absorber to minimise the reflected power. The simplest approach for this is a cone or wedge shaped cavity. A conical target is rotationally symmetric and will have equal performance for any polarisation. If only a single linear polarisation is required, a wedge cavity can also be used. The amount of reflections inside the wedge increases as the opening angle of the wedge decreases. However, a small opening angle for a given aperture results in a deep wedge and a large volume and more mass. A more volume efficient method of achieving multiple reflections is a repeating array of small cavities and is the preferred design of current spaceborne radiometers. Both linear polarisations are typically required, so the array consists of pyramidal elements for equal performance. The pyramids each have a metal core which is part of the baseplate acting as structural support and reflector. Although the pyramidal array is very space efficient, which is highly desirable on satellite platforms, it has a number of disadvantages.

The pyramid tips should be infinitely sharp to avoid any direct backscatter, but in reality have a real thickness and are very susceptible to breaking, increasing the reflecting area even more. If there are broken tips near the beamcenter where there is a lot of incident power, this can be noticeable in $|S_{11}|$ measurements. They are also prone to thermal gradients as

the thermal conductivity of the absorber is low compared to its metal backing [34]. These gradients are hard to detect since the RTDs do not fit into the pyramid cores and need to be inferred by thermal simulation. Lastly, the manufacturing of both the metal baseplate with its own pyramidal shape and the casting of the absorber onto the core is complex and expensive. A wedge or cone shaped OBCT is easier and cheaper to manufacture and the RTDs are potted closer to the absorber, which helps to identify and characterise any possible thermal gradients. However, it comes at the cost of more volume and mass if the size of the aperture cannot be suitably minimised.

Arctic Weather Satellite

2.1 EPS-Sterna

Arctic Weather Satellite (AWS) is a prototype meteorological mission funded by the European Space Agency (ESA). It is a precursor for a future constellation planned by the European Organisation for the Exploitation of Meteorological Satellites (EUMETSAT). The constellation is called EUMETSAT Polar System Sterna (EPS-Sterna) and its primary objectives are to improve global NWP, enhance nowcasting capabilities at high latitudes, complement existing meteorological programmes and contribute to global climate monitoring [38]. EPS-Sterna is awaiting approval by the EUMETSAT council and depends on the success of the AWS mission. No major changes are planned in the satellite design between the two missions and thus EPS-Sterna has been a major design driver for the AWS mission.

Typically, operational meteorological programmes such as EUMETSAT's METOP-SG [39], Joint Polar Satellite System (JPSS) [40] by the NOAA and FY-3 [41] by the China Meteorological Administration (CMA) consist of two or more large satellite platforms several cubic meters in volume, weighing over a tonne, carrying a variety of instruments in the same sun-synchronous polar orbit with a phase offset. Research has shown that Microwave Radiometers (MWRs) are among the most impactful for NWP [42] and that adding more MWRs will yield further improvements [43, 44, 45].

EPS-Sterna takes the novel approach of launching a larger number of identical MWRs, each on their own dedicated platform. The current baseline intends three orbital planes hosting two satellites each, for a total of six AWS satellites in orbit throughout the 13 year lifetime of the constellation [46]. The sun-synchronous polar orbits are chosen to complement the existing operational meteorological programmes (see Figure 2.1). A total of 20 satellites will be required over the constellation lifetime, which is an unprecedented quantity for a meteorological mission.

In combination with the existing MWRs, EUMETSAT anticipates achieving 90% global coverage in 2.4-3.8 hours or 3.1-4.7 hours for EPS-Sterna by itself [47]. For comparison, the METOP-SG satellites require almost 24 hours for equal coverage [48]. In the high latitudes, a mean time between measurements of 20 minutes is achievable. A study by EUMETSAT predicts a 6% and 9% reduction in NWP error for the European member states and the Arctic region, respectively [49]. It goes on to state that the net economic benefit over the constellation lifetime is predicted to be 32.7 billion Euros.

2.2 The Arctic Weather Satellite mission

The AWS mission consists of a single payload hosted on the InnoSat platform made by OHB Sweden. With stowed solar panels the entire satellite fills a volume of only $1.0 \times 0.7 \times 0.9$ m and weighs about 125 kg. The payload is a cross-track scanning MWR covering the 54, 89, 165-183 and 325 GHz bands divided into 19 channels built by AAC Omnisys, shown

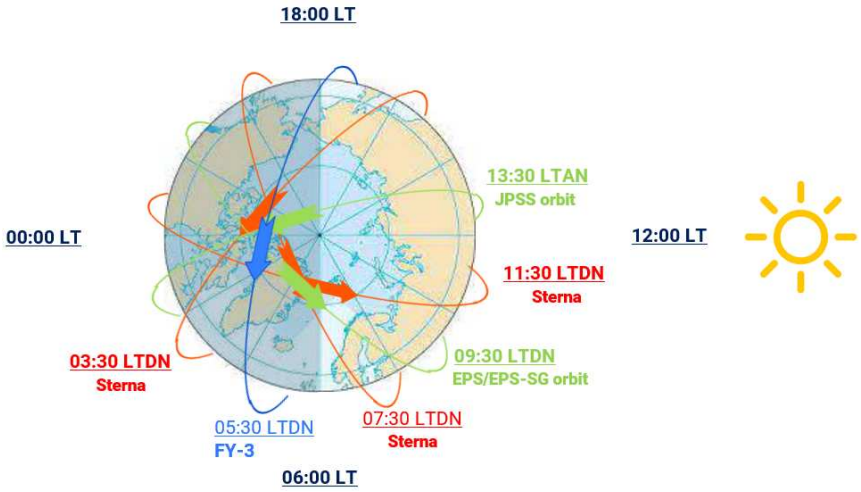

FIGURE 2.1: Planned EPS-Sterna orbits in context of other operational meteorological missions. Courtesy of EUMETSAT [47].

in Figure 2.2. The lower three bands are part of an established set of frequencies used for retrieving temperature and humidity of the atmosphere. Multi-channel measurements in 50-58 GHz and 165-183 GHz enable retrievals of vertical atmospheric profiles, whereas 89 GHz is a window channel which can be used for land, sea or cloud detection. The 325 GHz band is a novel addition designed to detect ice clouds, which are important contributors for the energy budget of earth [50]. AWS is the first mission to provide measurements in this frequency band [16], with the ICI from METOP-SG to follow in the near future. Apart from ICI, there are more meteorological missions covering the AWS bands, all contributing to NWP together. Table 2.1 gives an overview of all AWS channels and their overlap with existing/future missions. The other missions cover additional frequency bands, but they are not shown here.

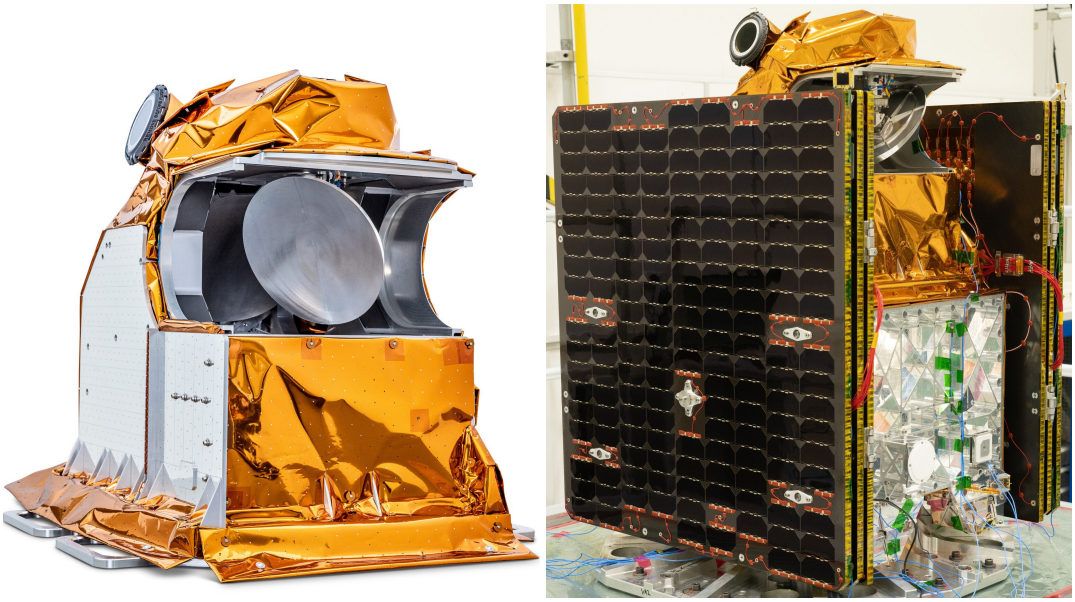

FIGURE 2.2: Picture of AWS radiometer (left). Picture of complete satellite (right). Courtesy of OHB Sweden and ESA.

The 54 GHz and 165-183 bands both use an LNA combined with an SSB architecture and filter banks to split the IF into the individual channels. The 89 GHz band is single channel

with two LNAs and a direct detection receiver. The 325 GHz receiver is a DSB architecture with subsequent filterbanks.

TABLE 2.1: Frequency Channels of EPS-Sterna/AWS and overlap with other instruments

Channel	Frequency (GHz)	Instrument overlap	Utilisation
11	50.3	ATMS, MWS, MWTS 3	Temperature
12	52.8	ATMS, MWS, MWTS 3	Temperature
13	53.246	MWS, MWTS 3	Temperature
14	53.596	ATMS, MWS, MWTS 3	Temperature
15	54.4	ATMS, MWS, MWTS 3	Temperature
16	54.94	ATMS, MWS, MWTS 3	Temperature
17	55.5	ATMS, MWS, MWTS 3	Temperature
18	57.290344	ATMS, MWS, MWTS 3	Temperature
21	89	ATMS, MWS, MWHS-2	Window Cloud detection
31	165.5	ATMS, MWS	Window/Humidity
32	176.311	ATMS, MWS, MWHS-2, ICI	Humidity sounding
33	178.811	ATMS, MWS, MWHS-2, ICI	Humidity sounding
34	180.311	ATMS, MWS, MWHS-2, ICI	Humidity sounding
35	181.511	ATMS, MWS, MWHS-2, ICI	Humidity sounding
36	182.311	ATMS, MWS, MWHS-2, ICI	Humidity sounding
41	325.15±1.2	ICI	Humidity Cloud detection
42	325.15±2.4	ICI	Humidity Cloud detection
43	325.15±4.1	ICI	Humidity Cloud detection
44	325.15±6.6	ICI	Humidity Cloud detection

Arctic Weather Satellite as a "New Space" mission

AWS was developed in a very short timeframe, especially for a mission intended for operational use. It went from kick-off in March 2021 to launch in August 2024, using the "New Space" approach by building on a lot of existing hardware and development for the MWS on the METOP-SG programme. For comparison, the MWS contract was signed in July 2013 with the launch of the first of three satellites scheduled for 2025, after AWS. However, the METOP-SG satellite is much larger, hosting six instruments. In terms of cost, the overall value of the AWS mission is published as "over 32 million Euro"[48], which includes the satellite platform. For MWS three flight models, excluding the multi-payload satellite platform, were purchased for 155 million Euro [51]. Significantly reducing the cost is a key design driver for AWS, since the satellite will be manufactured 20 times for EPS-Sterna. However, this introduces a wide variety of constraints on the design, testing and manufacturing of every aspect of the instrument.

2.2.1 Current status of AWS

AWS launched on the 16th of August 2024 from Vandenberg Space Force Base aboard a Falcon 9 rocket. Following the launch, the instrument was deployed successfully and is currently undergoing commissioning. While fully calibrated data has not been made available, some initial data has been publicised by ESA. Figure 2.3 shows relative brightness temperatures for a 183 GHz channel, which measures humidity recorded on the 14th of September 2024. The blue feature captured in the middle of the frame is the storm "Boris" over Europe, which killed 21 people and caused significant flooding in Eastern Europe [52].

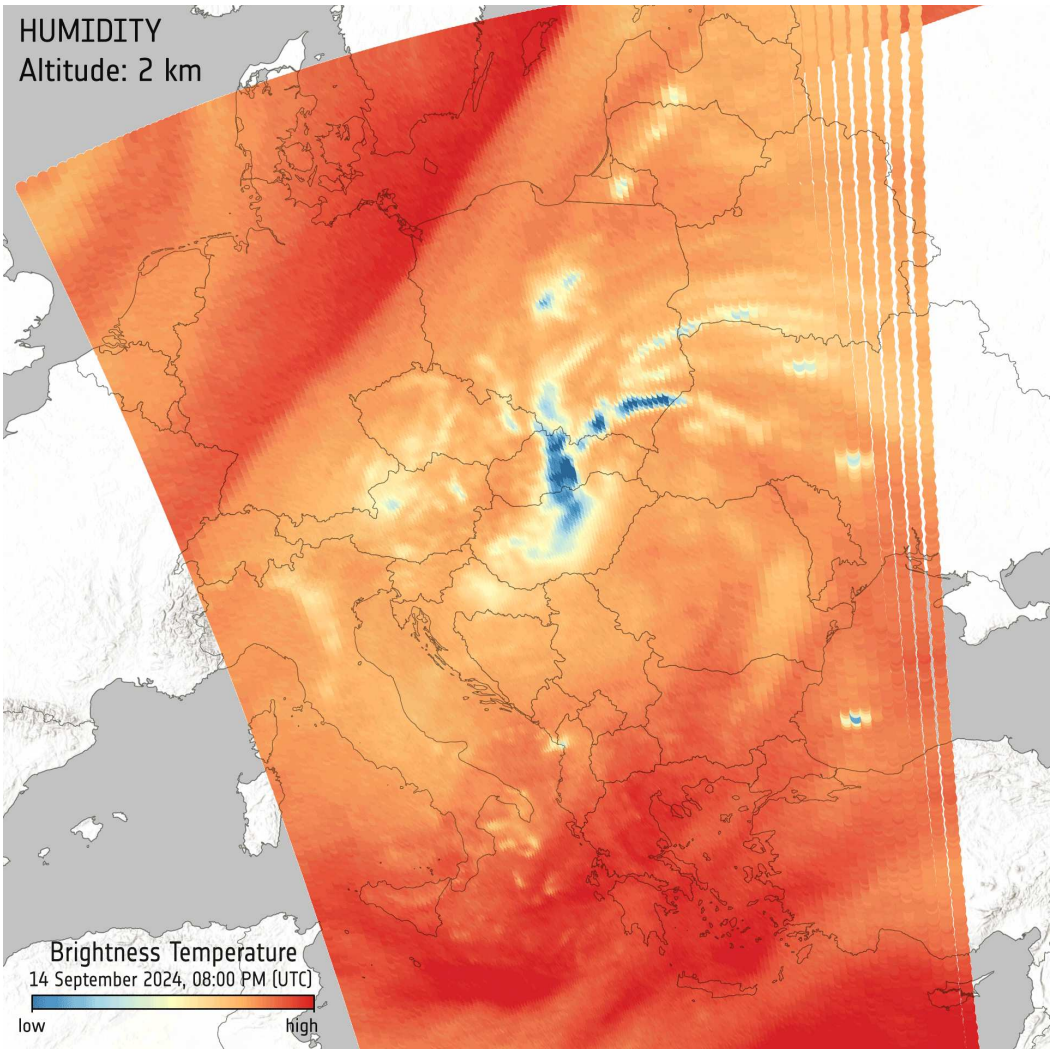

FIGURE 2.3: First humidity data from orbit recorded by the Arctic Weather Satellite radiometer. Taken from [53].

2.3 Thesis objectives

The AWS radiometer is the first cross-track scanning microwave radiometer using a feedcluster directly illuminating the scanning mirror. This design choice was the key to reducing the cost and achieving the compactness necessary to facilitate a future constellation using AWS. The overall objective was that the AWS radiometer delivers data of equal quality or better than current meteorological satellites with a fraction of the cost and time. The technical and scientific aims which were covered by the publications written during this thesis are the following:

Quasi-optical optimisation

Although the basic design of the feedcluster and scanning mirror was set, the details such as feedcluster positioning and reflector sizes were open. My aim was to finalise the design of the calibration optics and optimise the design of the feedcluster and scanning mirror in line with instrument mainbeam requirements. Another goal of the optimisation was spillover mitigation, which also investigated the use of absorber on the instrument structure.

Characterise quasi-optical performance

The novel design of AWS resulted in unusual behaviour for a cross-track scanning microwave radiometer. I investigated the effects of the design on the instrument radiometric performance, such as mainbeam characteristics, beam offset and rotation by electromagnetic simulations. These features affect the absolute accuracy of the AWS radiometer and the aim was to characterise them so that they can be compensated for in the calibration of the instrument.

Design and manufacturing of calibration targets

Another aspect of the project was the design and manufacturing of the AWS onboard and onground calibration targets. As part of my work I performed the quasi-optical design of the OBCT as well as the onground variable temperature target (VTT) using electromagnetic simulations. Both targets utilise a new epoxy based absorber mixture, which is more workable than previous mixtures, for which I developed a manufacturing process resulting in a homogenous mixture with high return loss in the AWS bands.

AWS quasi-optical design

This chapter presents the AWS quasi-optical design, its optimisation and performance characteristics. Although the AWS optics are simpler than that of other operational microwave sounders, the effects of these simplifications required extensive simulation to be fully understood. The AWS optics were simulated and optimised using the General Reflector Antenna Software Package (GRASP) and Electromagnetic Simulation Tool for Electrically large Antenna models (ESTEAM) software packages by TICRA and will be referred to as TICRA Tools [54] within this chapter. GRASP was used for the Physical Optics (PO) based simulations and ESTEAM was used for the Method of Moments (MoM) simulations. Not all 19 channels were individually simulated, since this would be too computationally expensive and would have significantly slowed down design iterations. Instead, three frequencies were chosen for each feedhorn, covering the low, middle and high end of the band, which are listed in Table 3.1. This work resulted in two publications [55, 56]. Not every plot for every band is shown in this chapter. All plots not shown here can be found in the Appendix.

3.1 Quasi-optical design overview

The AWS quasi-optics at its core consists of four feedhorn antennas directly illuminating the scanning mirror. All feedhorns are smooth-walled spline horns. The feedhorns are not manufactured individually, but cut into a splitblock. In this case the splitblock consists of three slabs forming two splitplanes. Each splitplane contains a pair of horns to form a more compact cluster than four horns on one splitplane. Figure 3.1 shows the positioning of the feedarray relative to the other optical elements, as modelled in TICRA Tools for PO simulation. Above the feedcluster sits the parabolic scanning mirror (blue) with a circular rim. It continuously rotates scanning across earth, cold space and finally the fixed parabolic mirror (green) positioned in zenith. This mirror is used to focus the beams down into the aperture of the wedge-shaped OBCT (black). The calibration mirror is also parabolic with a super-elliptical rim. A small amount of the roof structure (orange) above the scanning mirror was included in the PO simulation. The rectangular part of the roof structure, scan plane, feedhorn apertures and instrument baseplate (grey) are all parallel to each other. The circular part of the roof structure is slightly off-parallel, pointing towards the baseplate.

TABLE 3.1: Simulated frequencies of Arctic Weather Satellite quasi-optics and their corresponding channels

Feedhorn	Low band (GHz)	Mid band (GHz)	High band (GHz)	Channels
54 GHz	50.3	53.6	57.3	11, 14, 18
89 GHz	87.0	89.0	91.0	21
183 GHz	165.5	178.8	182.3	31, 33, 36
325 GHz	321.8	325.1	328.5	43

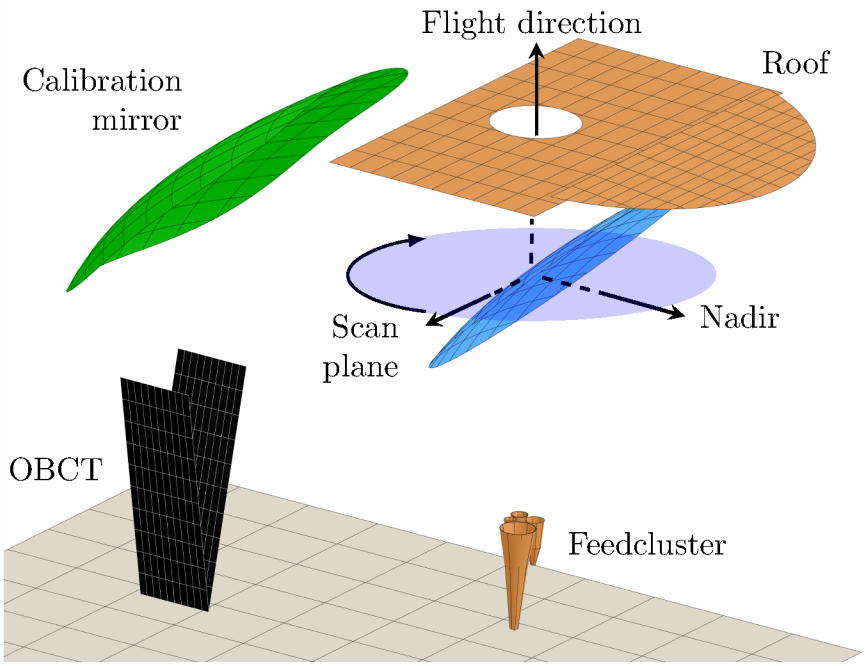

FIGURE 3.1: Physical optics model of AWS in TICRA Tools.

The most notable feature of the quasi-optical architecture is that unlike all other cross-track scanning radiometers, no additional quasi-optical elements are used to co-align the individual beams and position them in the focal point of the scanning mirror. Although feedclusters in direct view of the scanning mirrors are used in conical scanners, in this case there is relative movement between the two elements. Rotating the entire assembly adds mass and complexity and on the large meteorological missions the constant torque induced by the rotating instrument is typically balanced out by an additional counter-rotating instrument mounted on the same platform. This is not possible for a single instrument payload. As a result, the AWS quasi-optics have the following unusual characteristics for a cross-track scanning radiometer:

- The four outgoing beams are offset from the pointing axis of the mirror.
- As the scan mirror rotates, the beams rotate around the mirror pointing axis.
- The beams are slightly elliptical and the shape rotates with scan angle.
- There are small spillover variations with scan angle.

3.2 Feedhorns

The feedhorns were designed by AAC Omnisys based on their experience with smooth-walled spline horns. There was a strong preference for these kind of horns as they are simpler to manufacture than corrugated horns, especially when considering that electroforming is not feasible for splitblock horn cavities. However, corrugated horns can achieve very high gaussicity [57]. High gaussicity is desirable for a radiometer feedhorn since it means very low sidelobes and consequently low spillover. An advantage of smooth-walled horns over corrugated horns is their higher aperture efficiency and less open parameters for optimisation. The feedhorn aperture sizes drive the overall size of the feedarray and how tightly they

can be packed. The feedhorn designs provided by AAC Omnisys were modelled and simulated in the respective low, mid and high band frequencies using TICRA's Corrugated Horn Analysis by Modal Processing (CHAMP) package. Figure 3.2 shows orthogonal cuts for each horn. The dashed line denotes the scanning mirror rim relative to the pattern. However, this assumes that the horn is positioned at the focal point of the mirror, which is not possible for all horns in a feedarray. In reality the dashed line will be shifted, due to the offset of the feedhorn from the scanning mirror focus.

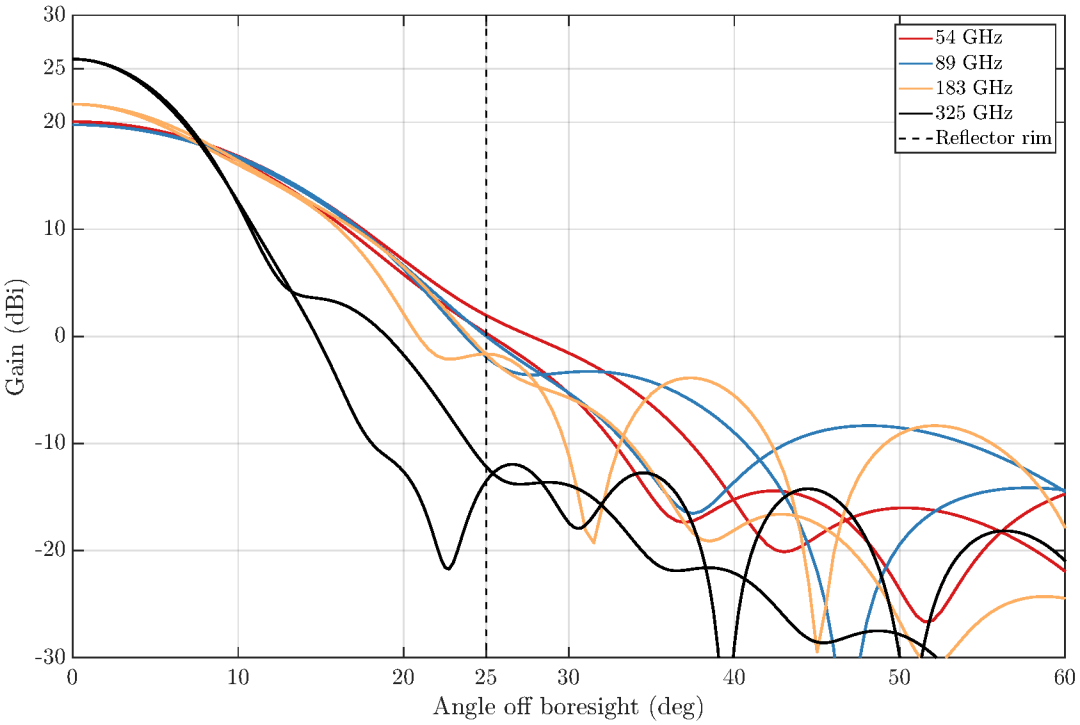

FIGURE 3.2: AWS feedhorn cuts in E and H plane for mid band. Published in [55].

3.3 Feedarray optimisation

The arrangement of the feedhorns in the splitblock relative to each other and the scanning mirror is a crucial aspect for the performance of the radiometer. Parabolic reflectors such as the scanning mirror have a single focal point where the phase center of the feedhorn should be located to achieve an outgoing collimated beam with low aberrations. In a feedarray only one of the horns can be located at the focal point. While this might lead to good performance for that particular horn, the cost in performance in the other horns is significant. Consequently, a lot of effort went into the arrangement and positioning of the feedarray to maximise the overall performance. Figure 3.3 shows an early model of the feedarray in the splitblock.

There were a number of constraints on the splitblock which restricted what parameters could be changed. The allocation of the feedhorns to their splitplanes in the splitblock were driven by the receiver positioning and not part of the optimisation. There was a restriction on minimum wall thickness for mechanical strength, dictating the separation betweeen feedhorns.

Optimisation of the open parameters was performed by sweeping individual parameters, assessing individual and averaged performance in a number of criteria which are as follows:

- Peak gain as a measure of how collimated the beam is

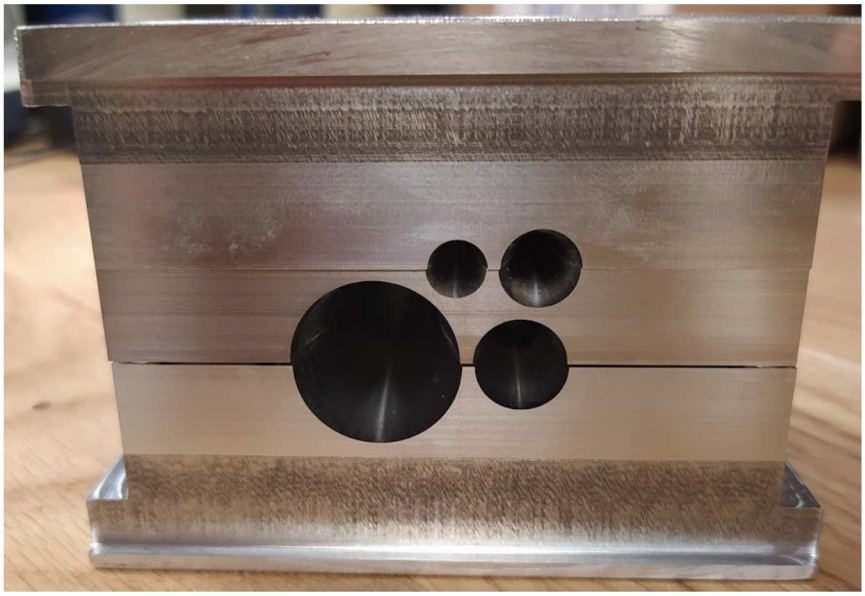

FIGURE 3.3: Picture of unaligned splitblock with visible splitplanes.

- Circularity of the full width half maximum (FWHM) contour as a symmetricity indicator
- Spillover at the scanning mirror

Circularity does not have a straightforward mathematical definition, since there are a number of edge cases for each definition that would result in a high circularity score, while not being circular. Initially a ratio between the largest and smallest radius of the contour was considered, but later changed to a more traceable method considering a ratio between the area and perimeter of the contour [58]. This can occur due to the reflector being undersized for the mainbeam or due to sidelobes in the beam.

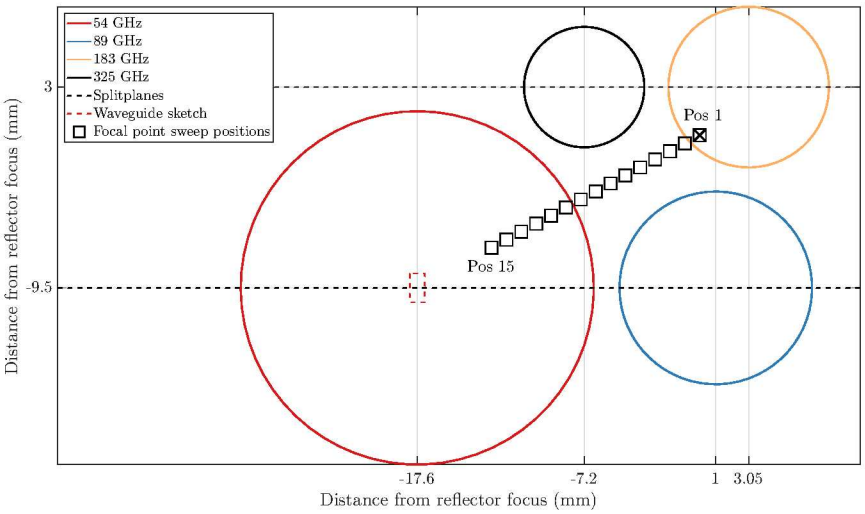

FIGURE 3.4: Sketch of feedhorn arrangement in the splitblock. Published in [55].

Figure 3.4 presents a sketch of the horn apertures in the splitblock. The squares denote possible positions for the scanning mirror focal point that were considered. A full 2D sweep across the face of the splitblock was not performed. The best overall performance was anticipated to be for a focal point position in between the four feedhorns. Hence the diagonal

sweep between the 183 and 54 GHz horn. A sweep between the 89 and 325 GHz was not performed, because good performance for the 183 GHz horn was considered priority. Only nadir scan angle was considered for this sweep.

Figure 3.5 gives an overview of the performance criteria across the sweep. A couple of general themes become apparent in the data. The 54 GHz band improves steadily in all criteria as the focus is moved closer to it. However, 183 GHz decreases in performance. The maximum performance for the two horns orthogonal to the sweep (89 and 325 GHz) is near the middle of the sweep when the focal point is closest to them. Circularity seems to exhibit an cyclical behaviour which scales with wavelength. Further plots for the mid band have been published in [55] and plots for the high band were also evaluated and can be found in the Appendix. The average of all horns for the different performance criteria and bands does not have a maximum at the same focal position for every plot, so an optimal focus position isn't immediately apparent. As a general trend, the performance loss in 183 GHz was more significant than the gains in 54 GHz performance when moving closer to the 54 GHz horn. This can be explained, by expressing the distance in terms of wavelengths instead of absolute distance. For example, moving 1mm away from the horn is a change of $\approx 0.63\lambda$ at 183 GHz but only $\approx 0.18\lambda$ at 54 GHz. The change in performance for the other two horns peaked towards the middle (around Position 5) and then dropped off. Considering this, in combination with the soft factor of 183 GHz being a priority, it was decided to keep the focal point at Position 1. Moving further towards the 183 GHz center would clearly have a negative effect on all the other horns and was therefore not considered.

Having fixed the lateral position of the feedarray, the distance of the feedarray to the reflector was varied in 1 mm steps to find an optimum. Ideally, the phase center of each horn would be placed at the focal distance of the reflector, according to gaussian beam optics [2]. But this does not consider the lateral offset of the feedhors in this array. Furthermore, the phase centers of the AWS feedhorns were not identical, as this proved very restrictive during feedhorn optimisation. It should be noted that the focal distance of the reflector itself was left unchanged, based on an early design from AAC Omnisys. Spillover was also evaluated for the distance sweep but is not shown here, as moving further away from the reflector will always increase spillover.

Figure 3.6 shows the circularity for low band versus splitblock distance from the reflector. The circularity variation once again seemingly scales with wavelength, increasing with frequency across the bands. The large variation for 325 GHz drives the average circularity, with a clear optimal distance at 160 mm. For mid and high band (see Appendix) the highest average circularity was 159 mm which was selected as the focal distance.

3.4 Scanning mirror optimisation

Due to asymmetrical illumination of the scanning mirror by the feed array, there was concern that the spillover would vary across the different scan angles. This would be a major issue for correct calibration of the instrument.

For the 54 GHz band the issue would be most pronounced, since the scanning mirror size is driven by the lowest frequency of the instrument, but not considering the offset. Changing the gain of the feedhorns to reduce their illumination on the mirror was not an option due to the FWHM requirements for the onground footprint. Likewise, the scanning mirror size could not be increased significantly due to volume and mass restrictions in the instrument. However, the rim of the mirror could be moved to equalise the spillover for each scan angle.

The rim refers to the outline of the reflector, either defined from the incoming or outgoing perspective. In Figure 3.7 the circular rim of the scanning mirror is shown in blue in front of the rim of the calibration reflector in green. This shape is then projected onto the parabola

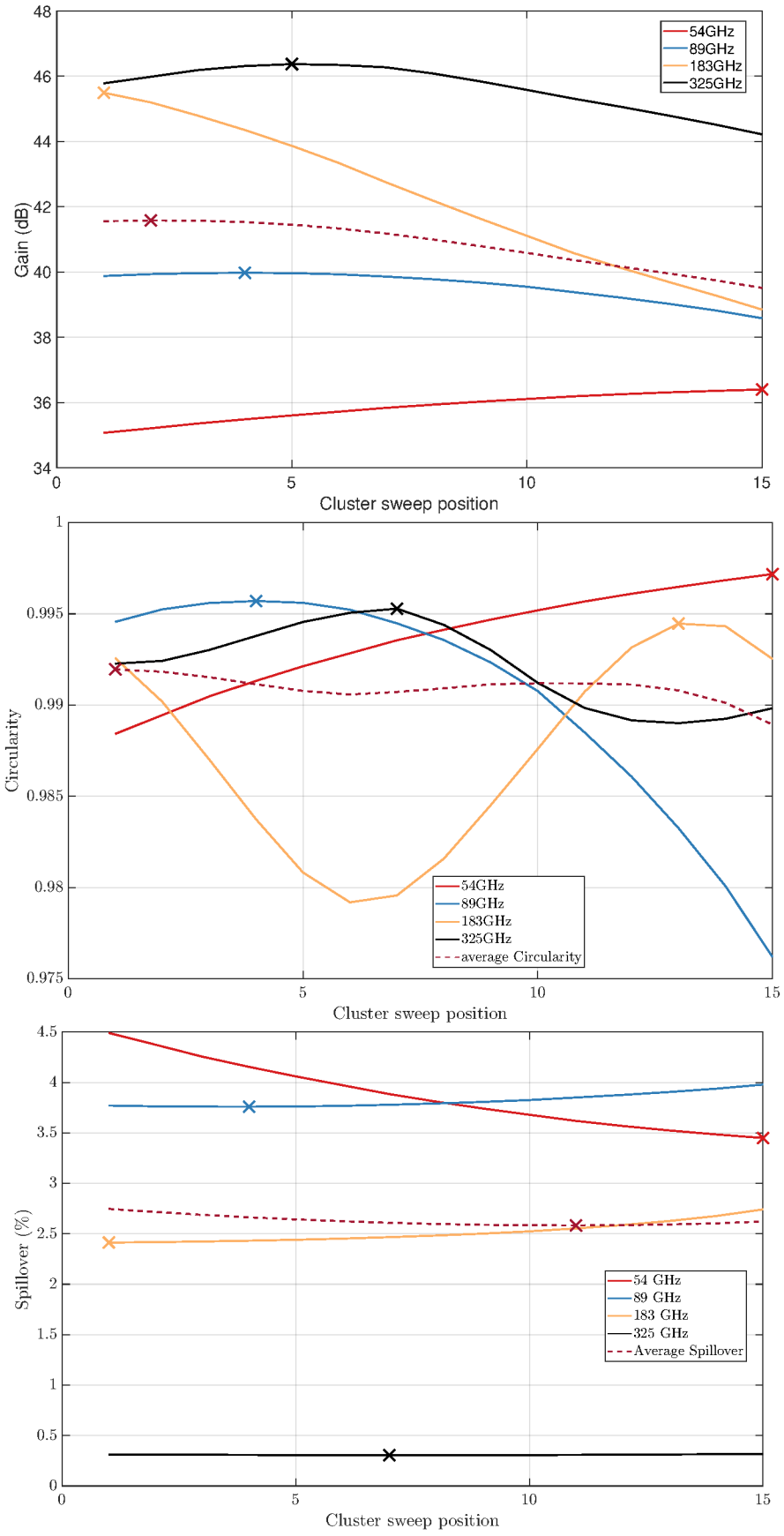

FIGURE 3.5: Peak gain, circularity and spillover for cluster sweep in low band.

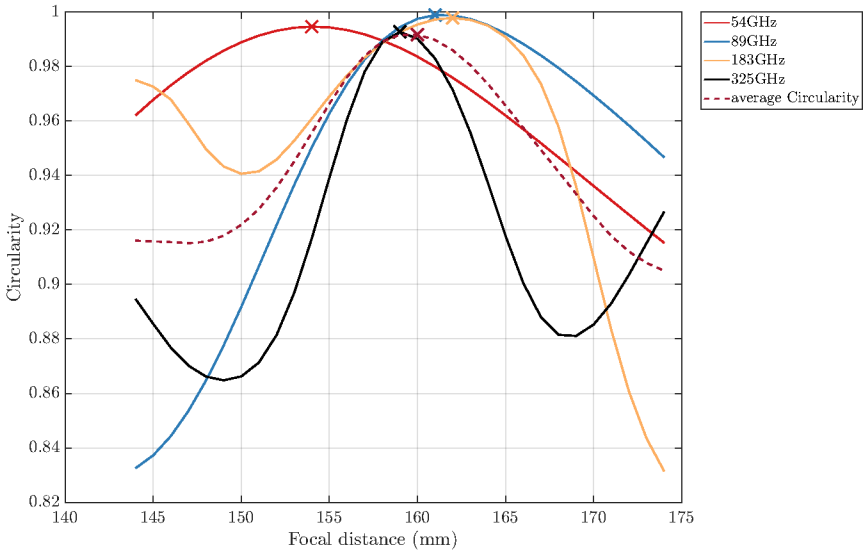

FIGURE 3.6: Circularity against distance to scanning reflector for low band.

describing the curvature of the mirror to form the completed mirror surface. If the rim is moved upwards it would look like a vertical shift in Figure 3.7, but from the side it would look more like a diagonal shift to the right. Figure 3.8 shows the apparent vertical movement using the red arrow and the equivalent movement along the parabola (dashed line) with the dashed arrow. It becomes obvious that a small movement in the red axis will result in a large displacement of the rim from the perspective of the horn.

The rays shown in Figure 3.8 span the same angular range for both the zenith and nadir orientation. The rim offset primarily serves to capture more illumination at the far edge of the reflector for any scan angle as shown by the two opposing orientations.

Using a MATLAB script, the rim offset was swept from -10 to +10 mm in the red axis of Figure 3.8 in 15°steps from -90 to 180°. The standard deviation across the scan angles was used as the performance criteria for the ideal rim position. The average spillover across the scan angles could be misleading as it may include larger variations. Figure 3.9 shows the sweep results for the low band of all horns, with the smallest standard deviation in spillover highlighed in red. Further plots can be found in the Appendix. It should be noted that the y-axes for each plot are different. Once again the final selection was a trade-off between the ideal offset for each horn/band. Overall, the 54 GHz had the highest spillover, as well as the highest variation. The final rim offset of +9 mm was selected to mitigate the 54 GHz as much as possible and being close to the ideal solution for the other horns. This process was restricted to reducing the overall spillover, but does not consider where the spillover occurs around the rim of the reflector for each scan angle. This is addressed in section 3.9.

3.5 Calibration optics optimisation

The calibration optics consists of the secondary mirror and the aperture of the OBCT. It was predetermined that the OBCT would be wedge shaped with an opening angle of 24°which was determined to be the optimal angle from previous research [59]. The apex of the wedge needs to lie in the zenith axis for optimum performance (Figure 3.1), meaning the width of the OBCT aperture drives the height of the wedge. Given the small size of the satellite platform and thus the instrument there was limited volume available for the OBCT. Positioning the OBCT directly in zenith of the scanning mirror was not possible as the wedge cavity would

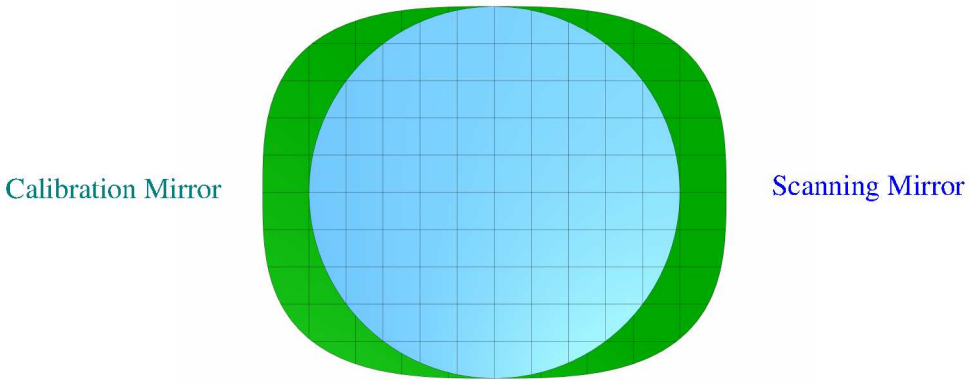

FIGURE 3.7: AWS reflector rims as seen from nadir looking into the instrument.

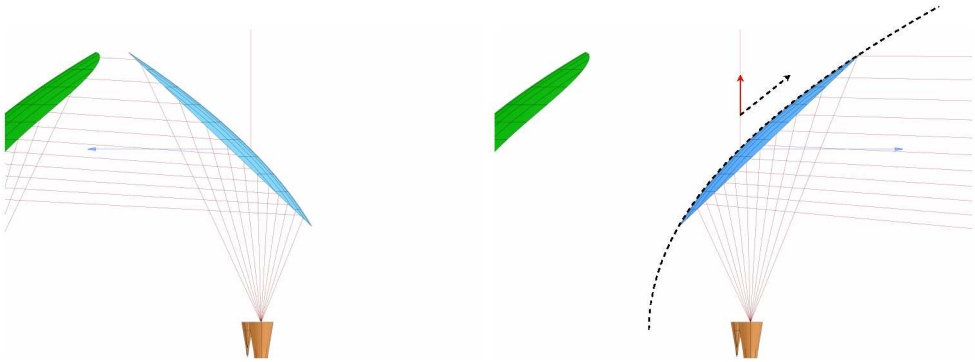

FIGURE 3.8: AWS scanning mirror for zenith (left) and nadir (right) orientation as seen from the side of the instrument.

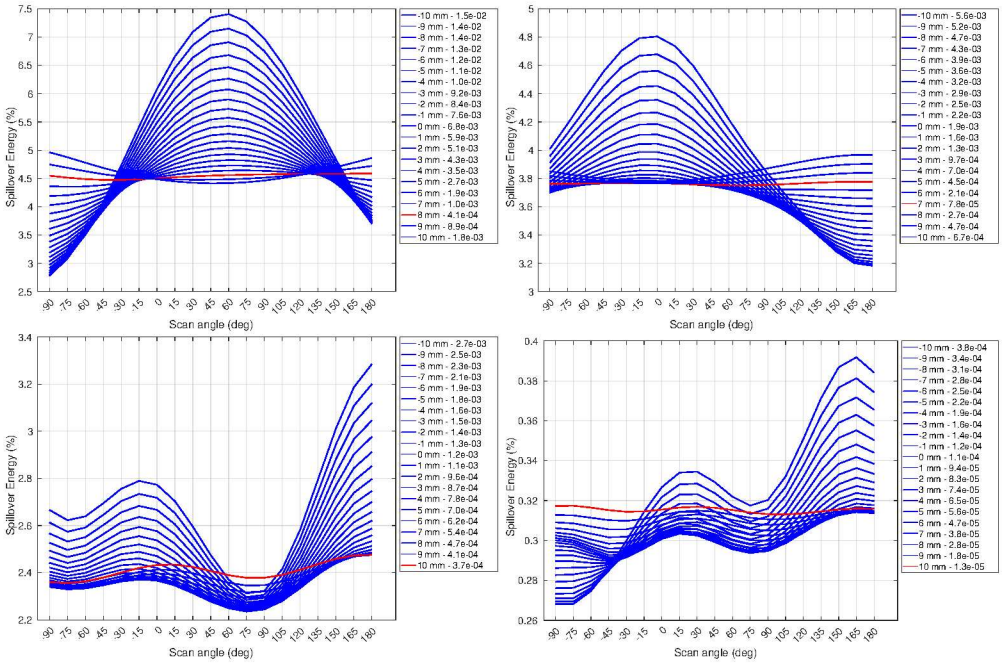

FIGURE 3.9: Spillover against mirror scan angle for different rim offsets.

be too large. Furthermore, the OBCT would be in direct view of earth through the scan opening, which would induce thermal gradients and degrade calibration.

Therefore, it was decided to add a secondary mirror to deflect the beams into the instrument and refocus them to reduce the required aperture size. To ensure a sufficient amount of measurements of the OBCT, the calibration mirror covers a 10°arc in the rotation of the scanning mirror. A super-elliptical rim shape (Figure 3.7) was selected to minimise spillover across the arc. The OBCT height was restricted by the distance of the instrument baseplate to the scanning mirror. Since the calibration mirror was bound to the scanning mirror position and rim size, it left limited room for the OBCT beneath it. However, choosing a very short focal distance would result in a very curved mirror more prone to aberrations and increasing the mass and size of the mirror. The instrument structure limited the available space for the mirror.

The final focal length was the maximum focal length possible to position the apex of the wedge with a clearance of 1.1 cm above the baseplate, allowing for the OBCT mechanical structure. Then the aperture of the OBCT had to be shifted relative to the mirror focal point to account for the beam divergence inherit to the AWS design. The calibration mirror focus is marked by the black cross in Figure 3.10, showing the superposition of beam contours across the OBCT aperture for different scan angles. Instead of a clear overlap in the focus of the reflector, as would be expected from a feedhorn in focus, the contours sweep across the aperture plane in an arc and deform towards the edges. The minimal aperture size was found by drawing these contours for zenith and ±5°about zenith in a common plot and enclosing them. This was then checked in TICRA Tools by placing a flat reflector of identical size in the model and calculating total spillover from the feedarray to this reflector.

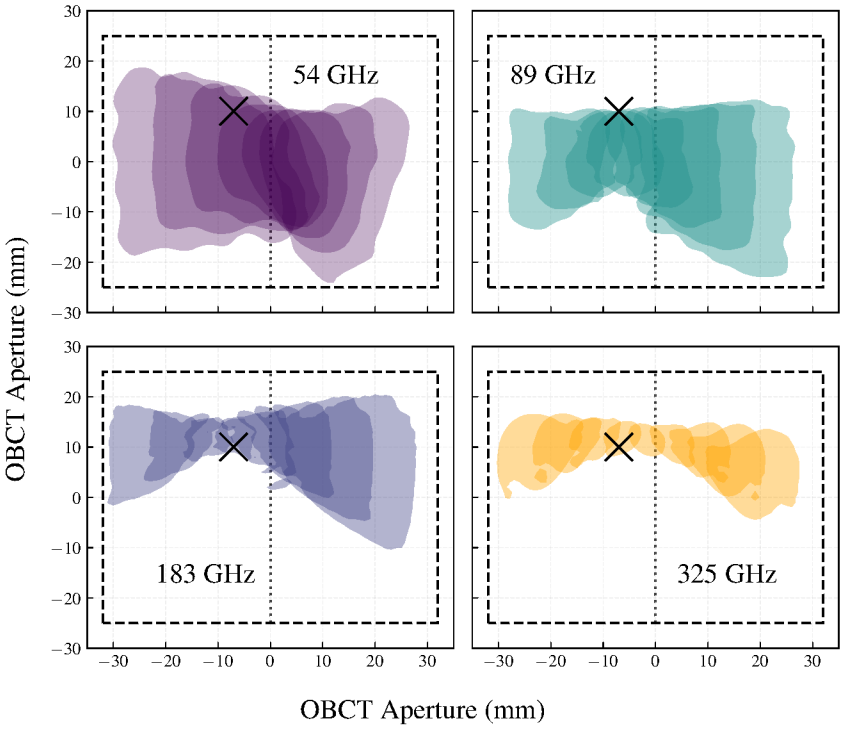

FIGURE 3.10: 30 dB contours for multiple scan angles and each horn projected on OBCT aperture. Adapted from [60].

Table 3.2 lists the spillover contributions per optical element for one band per horn. For 325 GHz the spillover is minimal as the reflectors are under-illuminated. Going down in frequency, the spillover increases significantly. However, the contribution from the calibration

TABLE 3.2: Spillover breakdown for one frequency per band in the zenith view.

Frequency (GHz)	50.3	89.0	165.5	321.8
M1 Spillover (%)	4.72	3.26	2.48	0.31
M2 Spillover (%)	0.43	0.10	0.22	0.02
OBCT Spillover (%)	0.32	0.05	0.05	0.00
Total Spillover (%)	5.48	3.41	2.75	0.34

optics remains small. In a common theme for AWS the 54 GHz spillover is highest, also for the calibration mirror and OBCT aperture.

3.6 Roof structure optimisation

The circular cap of the AWS roof structure was added after first analysis of the PO farfield plots showed a major sidelobe with direct earth view. Figure 3.11 is an azimuth over elevation plot of the projected farfield pattern from the scanning mirror. The coordinate system for this plot is centered on the scanning mirror and the origin is looking in flight direction of the instrument, through the roof. The outline of the instrument opening is sketched out in black. The deformed shape is due to projection effects from 3D cartesian space to azimuth/elevation. The red outline is the original roof structure of the instrument, where absorber could be placed. Although the satellite structure is in the nearfield of the scanning mirror, this method allowed for quick analysis what is in view of the spillover. Anything inside the black outline is projected outside the instrument. Anything outside the black outline is seeing some part of the instrument interior. However, since the instrument interior is largely reflective metal it is impossible to predict whether the reflections will eventually land on earth or cold space without including more of the structure and using MoM simulations.

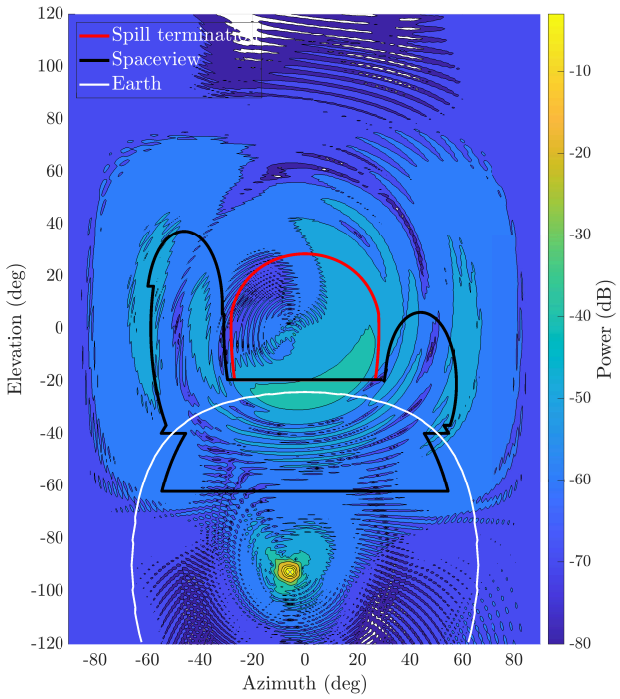

FIGURE 3.11: Early farfield plot with satellite opening and roof outline. Farfield for 54 GHz high band.

In Figure 3.11 a large sidelobe can be seen intersecting with earth (white outline). This sidelobe also existed for other bands and frequencies and complicates brightness temperature corrections. Spillover to cold space is straightforward to correct, as it has as a constant and well defined brightness temperature, provided there are no other stellar objects in the view. Spillover on earth varies depending on multiple factors such as satellite position, atmospheric conditions and the changing emissivity of the land and sea surface. While it is feasible to constrain the brightness temperatures based on some assumptions, there would still be significant uncertainty. The circular roof was added to capture this spillover and initial plans were to add absorber to the roof, terminating the spillover. However, due to mass and mechanical load restrictions the size of the cap had to be limited. Secondly, the absorber would be located on a very exposed structure (see Figure 2.2) subject to temperature swings caused by thermal

radiation from Earth, Sun and cold space. This would make the absorber brightness temperature unpredictable or require dense temperature sensor coverage. Since there was not a lot of space available, the absorber could not consist of a pyramidal array, which is commonly used for high return loss absorber. A flat, but low return loss (≈5 dB) absorber would not suffice to terminate the spillover and the remaining energy would still reflect towards earth. Lastly, the absorber would have to already be space qualified to be included in the project. Instead, the cap was tilted to deflect the sidelobe towards cold space. A comparison between no cap and the tilted cap can be seen in Figure 3.12 in a uv-hemisphere. In the right plot most of the sidelobe has been deflected from flight direction towards the anti-flight direction and crucially outside the earth outline.

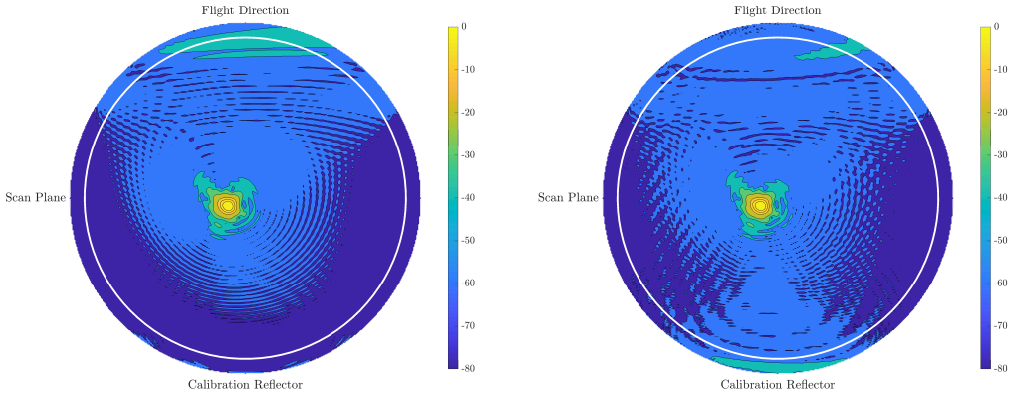

FIGURE 3.12: Comparison of no roof cap (left) and angled roof cap (right) for 54 GHz low band. Nadir facing Hemisphere grid shown in uv-coordinates. White circle marks earth outline.

3.7 Including the AWS Structure

Once optimisation using PO simulation was completed, it became clear that the significant spillover energy needed to be investigated further. MoM simulations, while being computationally more expensive, can readily handle the reflections inside the AWS structure. The structural model included in the ESTEAM package was based on the computer aided design (CAD) model of the instrument. To minimise simulation time, irrelevant details such as outward facing weight saving pockets, screw holes and electrically reflective housings were removed. Since simulation time increases with frequency and the 325 GHz band has negligible spillover, no MoM simulations were performed in this band. For 183 GHz it was also not possible to perform as many simulations as for the lower two bands. Total simulation time for low, mid and high band for a single scan angle at 183 GHz was 32 days using a high performance machine. For details regarding the simulation setup the reader is referred to [56]. Figure 3.13 shows the CAD model and its mesh in ESTEAM.

The red surfaces in the CAD correspond to absorbers that have been added on the structure in an effort to terminate some of the spillover. The selected absorber consisted of a flexible sheet with adhesive backing that could readily be cut into shape and attached to the existing structure without any additional fixtures. Some sheets are visible in Figure 2.2 on the struts next to the scanning mirror. The effective return loss in the simulations for the absorber was 5 dB based on material datasheets. Current distribution plots such as Figure 3.14 combined with simple raytracing were used to decide on the absorber placement. The red rectangle highlights a direct illumination of the structural strut. This section of the strut is

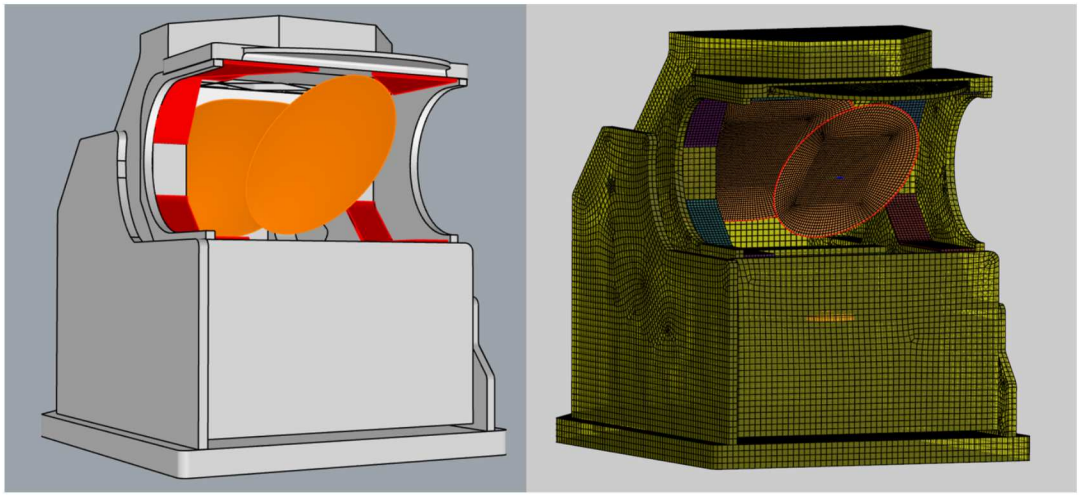

FIGURE 3.13: CAD model of AWS structure in ESTEAM and mesh rendering.

tilted 45°to the vertical (same orientation as the scanning mirror) and thus reflects the incident spillover directly towards earth. In terms of spillover termination this is the worst case scenario since 5 dB is insufficient for significant absorption and the earth coupling to earth is still strong. Reflections on the horizontal roof structure (black rectangle) can have more reflections as they bounce between the the roof and the horizontal structural elements left and right of the feedcluster (obscured by instrument front plate in Figure 2.2). Both these surfaces are covered in absorber and can iteratively attenuate the spillover. The current distribution also shows the illumination of the redirecting roof cap, confirming the PO simulation. Unexpected scattering features also appear, for example on the edge between the left and front radiating plates highlighted by the white rectangle.

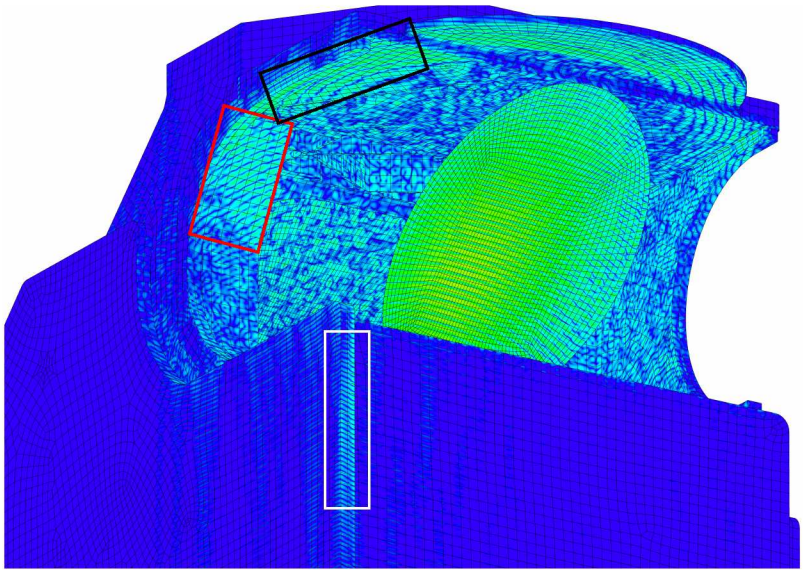

FIGURE 3.14: Surface current distribution for 50.3 GHz on AWS structure

The scattering introduced by the structure is visible in the farfield (shown in section 3.9), but it is also important if it affects the mainbeam. Since PO is the only realistic method to simulate several scan angles in a timely manner, it is important to evaluate its accuracy relative to the more complete MoM model. Figure 3.15 shows a comparison of the 89 GHz

mainbeam down to -30 dB for the two simulation methods. There are minor deviations down at the -30 dB contour, but very good agreement until then. The relevant performance criteria are based on the -3 dB contour where the two methods are interchangeable. More comparisons can be found in the Appendix.

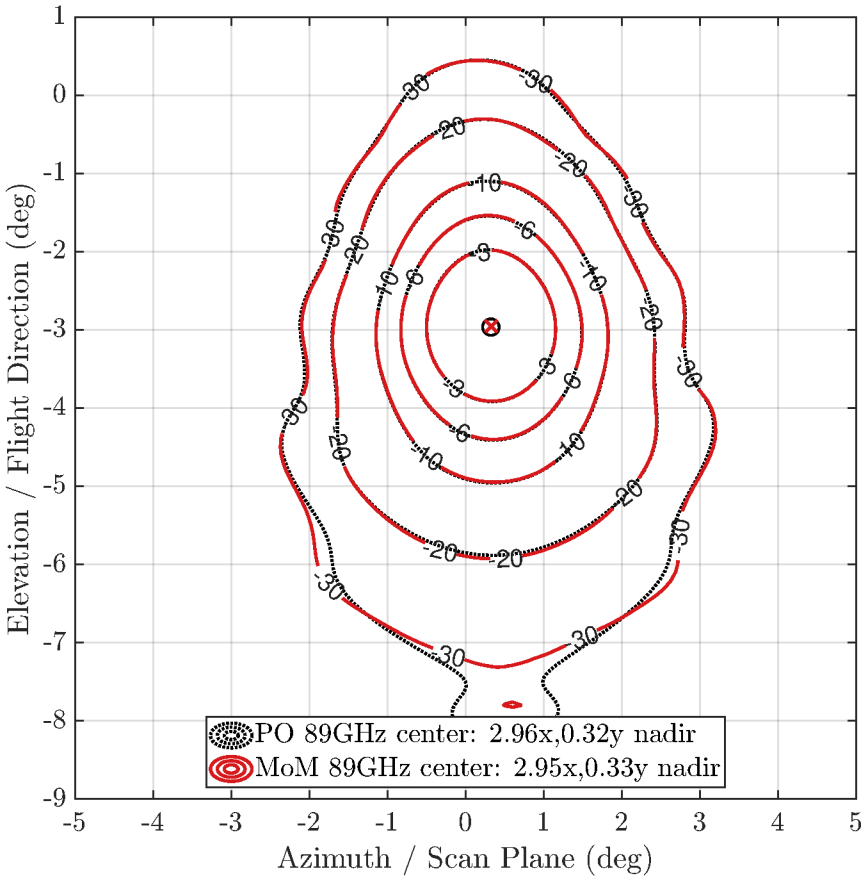

FIGURE 3.15: Comparison of PO and MoM mainbeam for 89 GHz at nadir scan angle

3.8 Mainbeam performance

3.8.1 Footprints

An important requirement for any spaceborne radiometer is the beam footprint since it drives the pixel size and coverage contiguity. The footprint is based on the -3 dB contour of the beam, also called the FWHM. The -3 dB contour (given in a spherical coordinate system) needs to be projected from orbit to ground to determine what the real footprint is in kilometres on ground. The orbital height therefore also affects the compliance to this requirement. For the AWS design the assumed orbital height is 600 km. For crosstrack scanning radiometers the pixel size varies along the track due to earth curvature as described in chapter 1. Therefore, all requirements apply to the nadir scan angle where there are no projection effects. Earth curvature is negligible for the mainbeam footprint and ignored in the projection. Figure 3.16 compares the real footprint to the instrument requirements. A key difference of this radiometer compared to other crosstrack scanning radiometers is that the footprints are not co-aligned. Furthermore, the footprints are less circular than other radiometers used operationally. Both of these effects occur due to none of the horns being in the focal point of the scanning mirror. The 54 GHz footprint is noticeably smaller than required, but this is an improvement over the requirement in this case since it is not driving the contiguous coverage. The smaller footprint provides higher resolution in this band. Most critical is the 165.5 GHz footprint, which is 300m undersize. However, for the baseline scan speed and orbital height coverage is still contiguous, which can be seen by the two additional contours showing the next pixel along track and the next same pixel in the next scan.

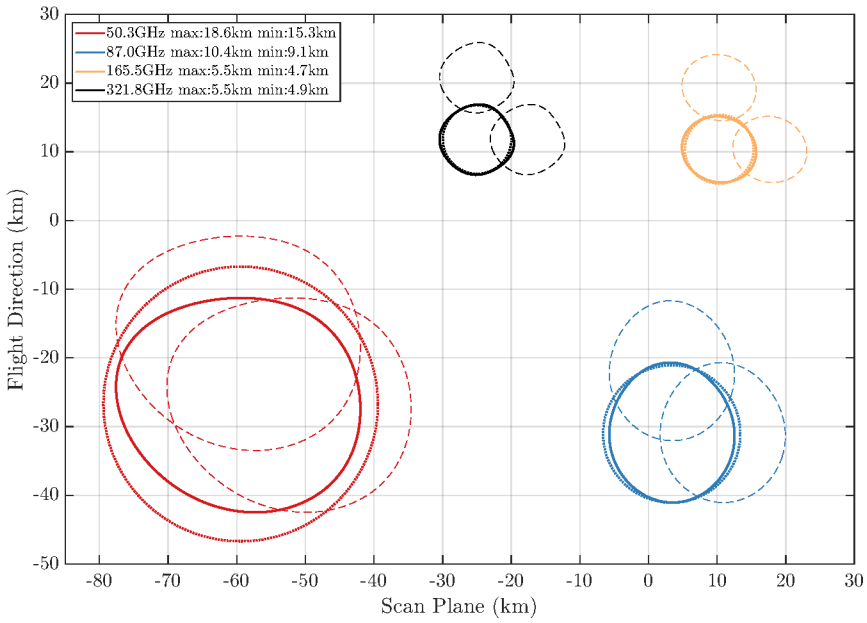

FIGURE 3.16: Lower band beam footprints for 600km orbital height against requirements. Dashed lines show next beam along track and next scan rotation. Dotted line shows baseline beam size.

Contiguous coverage

Achieving contiguous coverage is an important aspect for a spaceborne radiometer, which enables the fast global coverage times of the constellation. Contiguous coverage means during

the cross-track track each measurement overlaps with the previous one and the next measurement after a full rotation overlaps with the previous one along the track, as shown in Figure 3.16. Other than the orbital height and beamwidth, the rotation speed of the scanning mirror can be adjusted to make sure the footprints along track overlap. This is still related to the orbital height, since it determines the speed of the satellite along track and therefore the amount of time it takes to travel one footprint diameter. Although the requirements are based on instantaneous footprints, the radiometer integrates over a finite period of time, meaning technically the footprints shown in the plot are "smeared" along the x-axis during a measurement. The integration time for AWS is 2.5 ms.

Beam symmetry

The ellipticity of the beams is restricted by a symmetry requirement, which specifies that the smallest and largest diameters of the -3 dB contour should be within 15% of the mean. In Figure 3.17 it can be seen that 54 GHz lower band is slightly out of spec for the largest diameter, since it is the most elliptical. This is true for the other parts of the band as well (figures in Appendix). All other bands are compliant.

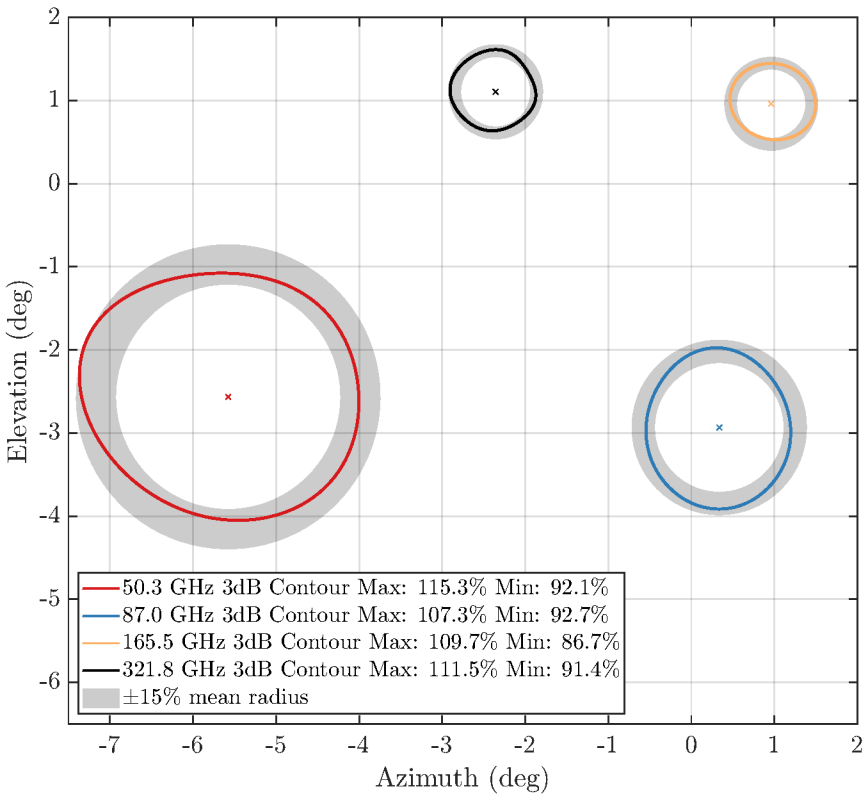

FIGURE 3.17: Lower band beam symmetricity against requirements

3.8.2 Mainbeam efficiency

The definition of the mainbeam efficiency (MBE) can have a significant impact on the perceived performance of the instrument. ESA uses a simple definition for the nadir pattern:

$$\text{MBE} = \frac{P_{mb}}{P_{sphere}} \tag{3.1}$$

where P_{sphere} is the total power in a full sphere radiation pattern. Because simulated antenna patterns are expressed as normalised values the total power in the sphere is equal to the area of a unit sphere which is 4π. P_{mb} is the power in the mainbeam defined as the integral of the power inside a specified contour, which in ESA projects is 2.5 times the -3dB contour.

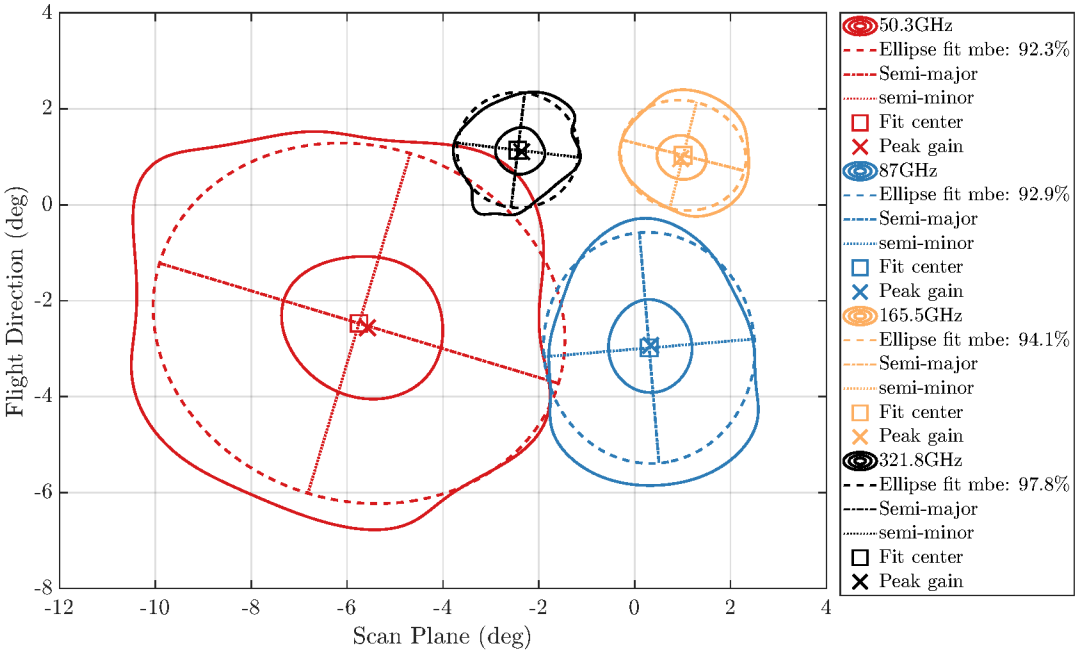

FIGURE 3.18: Mainbeam efficiencies for nadir lower band plotted with -3dB and -20dB contours.

In the case of AWS the -3dB contours are too asymmetric to be approximated by circles and therefore an elliptical fit needs to be used. The resulting fit is then scaled up by a factor of 2.5 and plotted against the -20 dB contour for comparison in Figure 3.18. The offset of the fit center against the peak gain of the pattern is a good metric for how close the fit is to the center of the beam. The comparison of the scaled up ellipse to the -20 dB contour also enables a qualitative assessment if the fit encompasses the majority of the antenna pattern. For the 54 and 89 GHz bands the -20dB contours are not centred around the peak gain, but biased towards one side of the semi-major axis. As a result the elliptical fit is capturing less power which affects the the MBE. For the two higher bands, the patterns are more centered and have a higher gain, so the elliptical fit is bigger compared to the -20dB contour and encompasses more power.

Defining the MBE as a fraction of the full sphere is a pessimistic assessment. It does not account for the spillover at the scanning mirror or energy that is terminated in the instrument using absorber.

3.8.3 Scan dependent beam rotation

An important feature of the AWS radiometer is that the beams are offset from the scanning mirror boresight. The absolute beam offset is static from the mirror boresight, but rotates around the boresight as a function of scan angle. This is due to the beam illuminating different parts of the reflector as it rotates. Simulating the antenna pattern for every single scene sample (145 total) and applying it in post processing is not feasible. Consequently, for accurate geolocation an expression of the beam pointing as a function of scan angle is required. The

fit can be assumed to be circular as the beams have to return to their original position for every full mirror rotation.

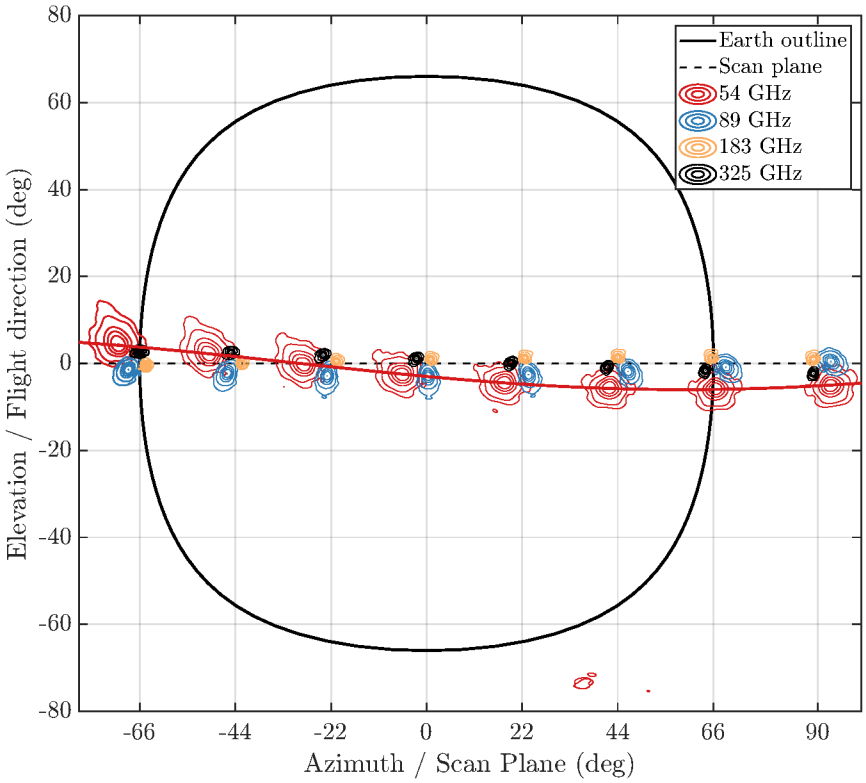

FIGURE 3.19: Patterns for several scan angles projected across earth.

Figure 3.19 demonstrates the rotation effect and includes a fit for the 54 GHz band peak gain. It shows antenna patterns for different scan angles on a static spherical grid centered on nadir. The fit is based on the offset of the peak gain in the pattern to the scan angle θ and expressed as:

$$Azimuth = \theta + x_0 + r \cdot cos(\theta + \beta) \tag{3.2}$$

$$Elevation = y_0 + r \cdot sin(\theta + \beta) \tag{3.3}$$

where r is the radius of the circle which is the absolute offset of the beam, x_0, y_0 are the center of the circle and β is a phase offset so the pattern is in the correct place for the nadir scan angle.

Table 3.3 summarises the coefficients for all the simulated frequencies. The rotation centres are close to 0, which is expected since the rotation should occur around the beam pointing axis. However, for the 54 GHz band the center is slightly shifted. This is caused by the peak gain in the pattern moving slightly. The circular fit could be forced to have a center at the origin, but checking the fitted center can highlight this peak gain movement which is an indicator of asymmetry in the pattern. The radius of rotation is largest for the 54 GHz, which is due to the horn being furthest away from the reflector focus.

In Figure 3.19 it is apparent that at the start of the scan (-54.5°) the offset for the 54 GHz beam has a large azimuthal component. Using Equation (3.2) for a scan angle of -54.5°, the resulting real beam pointing for 50.3 GHz (AWS channel 1) in azimuth is -60.0°. Taking into account the width of the pattern and that the atmospheric opacity is very low in this channel, it can be predicted that the first couple of measurements of each cross-track will see

TABLE 3.3: Circular fit coefficients for each beam and frequency

Freq (GHz)	x_0	y_0	r	β
50.3	-0.091	0.165	6.162	-154.28
53.6	-0.073	0.162	6.183	-154.385
57.3	-0.116	0.200	6.172	-153.89
87	0.018	-0.002	3.00	-83.216
89	0.018	-0.002	2.995	-83.216
91	0.020	0.001	3.00	-83.251
165.5	-0.005	0.002	1.371	44.782
178.8	-0.005	0.002	1.371	44.782
182.3	-0.005	0.002	1.371	44.782
321.8	-0.002	0.054	2.573	155.72
325.1	0.012	0.066	2.596	156.083
328.5	0.012	0.066	2.596	156.08

the atmospheric limb/cold sky. At the end of the cross-track the circular fit predicts an beam pointing azimuth of 53.4°and the beam should suffer from the same issue.

First light data after launch (Figure 3.20) confirms that the samples at the start of the cross-track show a cold bias. Specifically the measurements taken over Africa, which provides a very warm background demonstrate the effect. In the figure the satellite is travelling from the top of the image to the bottom over Africa and then travels upwards over the Pacific to complete one orbit. The first measurements of the cross-track (right side, descending) show a cold bias against the warm background of a land mass. At the end of the cross-track (left side, descending) the cold bias is not visible, indicating that this is not an effect due to the longer path through the atmosphere at the edges of the scan. As an additional control, the same orbit for 89 GHz, which is also a window channel is shown in Figure 3.21. The same effect is not apparent over e.g. Africa. This is due to the beam pointing at the beginning of the scan (again using Equation (3.2)) is only 56.7°. The first light data provides a first indication that the beam rotation and offsets exist as simulated.

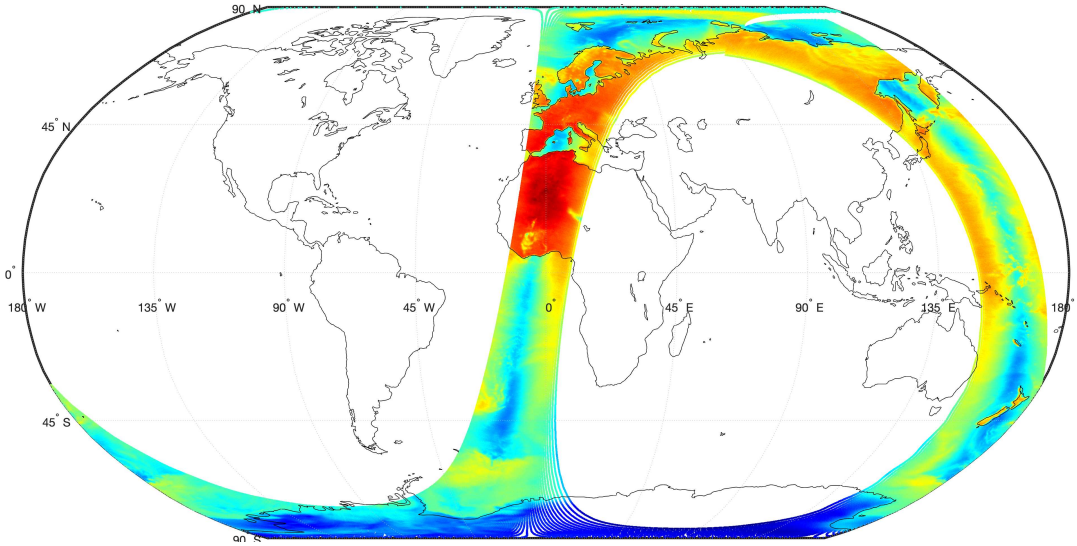

FIGURE 3.20: First light data taken by AWS over one orbit for channel 1 (50.3 GHz). Colours show relative brightness temperature from cold (blue) to hot (red). Image from J. Barbosa, RDA GmbH.

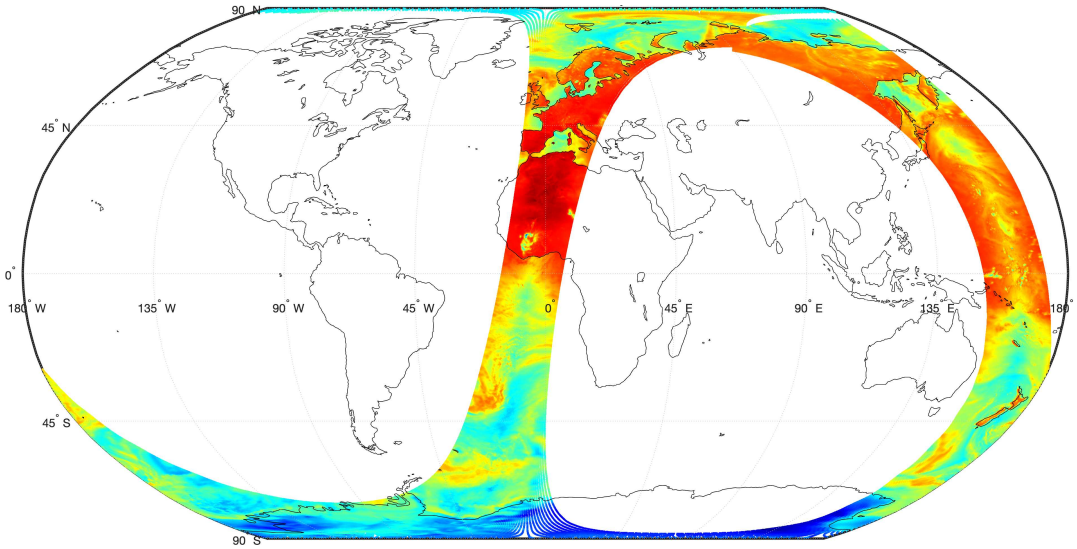

FIGURE 3.21: First light data taken by AWS over one orbit for channel 9 (89 GHz). Colours show relative brightness temperature from cold (blue) to hot (red). Image from J. Barbosa, RDA GmbH.

3.9 Full farfield sphere

For the 54 and 89 GHz bands it is feasible to compute several scan angle positions using MoM analysis of the full structure on the full sphere. This enables a detailed breakdown of the energy distribution and hence more comprehensive characterisation and compensation for spillover. Since the spillover at 183 GHz is also not negligible it would be desirable to do the same for this band. In the frame of this thesis it was only possible to perform a simulation for the nadir scan angle, which required significant effort from TICRA to even be able to run it. For the lower two frequencies the simulated scan angles were ±33°, nadir, +90°(cold sky) and +180°(obct view). Each scan angle has to be simulated twice per frequency; once with no absorber (perfect electric conductor (PEC)) and a second time including the absorbers shown in red in Figure 3.13.

Figure 3.22 is a plot of the full sphere where regions of interest are outlined in white. By integrating the power in these regions of interest and assigning them a brightness temperature, an effective brightness temperature measured by the radiometer can be estimated. The regions of interest are cold sky, earth, nearbeam and mainbeam. Cold sky is defined as everything outside the large solid outline which is the earth silhouette in the azimuth over elevation coordinate system. The area between the earth outline and the dashed circle is the earth spillover. Between the dashed circle and the smaller white solid ellipse is the nearbeam area. Inside the white ellipse is the mainbeam, which is calculated according to the same methodology detailed in section 3.8.2. The output data from TICRA Tools needs to be scaled correctly for the changing grid element size in the azimuth over elevation coordinate system prior to integration. Grid element size distortion increases away from the azimuth axis towards the poles of the coordinate system (±90°Elevation). This same effect creates the unintuitive earth outline. The power in each grid element normalised in radians is therefore calculated as:

$$P_i^{4\pi} = P_i \cdot \cos(El_i) \cdot \left(Az_i \frac{\pi}{180}\right)^2 \tag{3.4}$$

Lastly, the amount of power terminated by the absorber is found by the difference between the full sphere integral of the PEC simulation and the simulation including the absorber. Since the rescaling is done using external MATLAB scripts, the two full sphere integrals are also compared to the full sphere integrals natively provided by TICRA Tools. As a control value, the sum of all the mentioned factors is shown as a control value against 100%. Compared to earlier farfield plots without the structure (Figures 3.11 and 3.12), the effects of the structure become apparent in Figure 3.22 for the 54 GHz band. Firstly, hemisphere containing the beam has higher background noise due to the scattering of the structure. Secondly, some new spillover lobes can be seen e.g. below the mainbeam. The ripple structure is most likely due to the scattering on the radiator panels indicated in Figure 3.14 with the white rectangle. Above the mainbeam some scattering lobes are visible in a horizontal band. They are most likely caused by the remaining power of the primary sidelobe which is not captured by the roof cap.

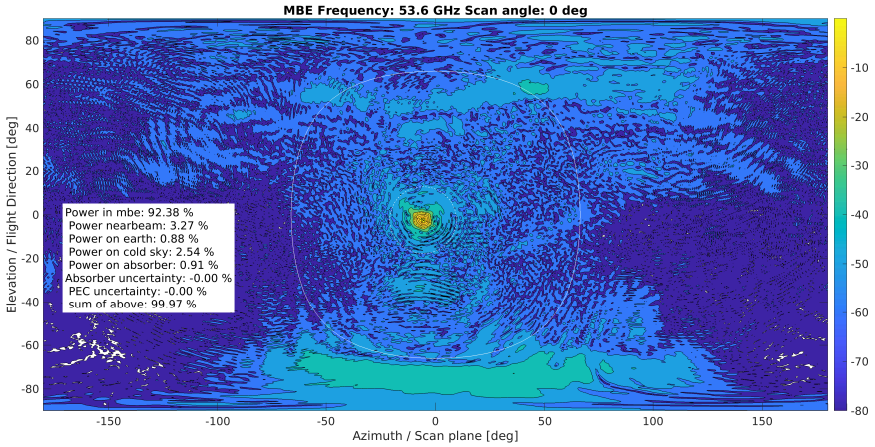

FIGURE 3.22: Full sphere farfield in Azimuth over Elevation coordinates for 53.6 GHz.

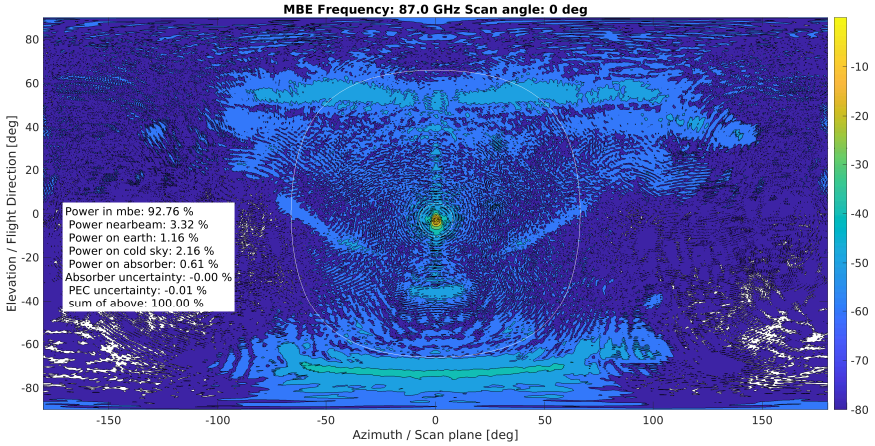

FIGURE 3.23: Full sphere farfield in Azimuth over Elevation coordinates for 87.0 GHz.

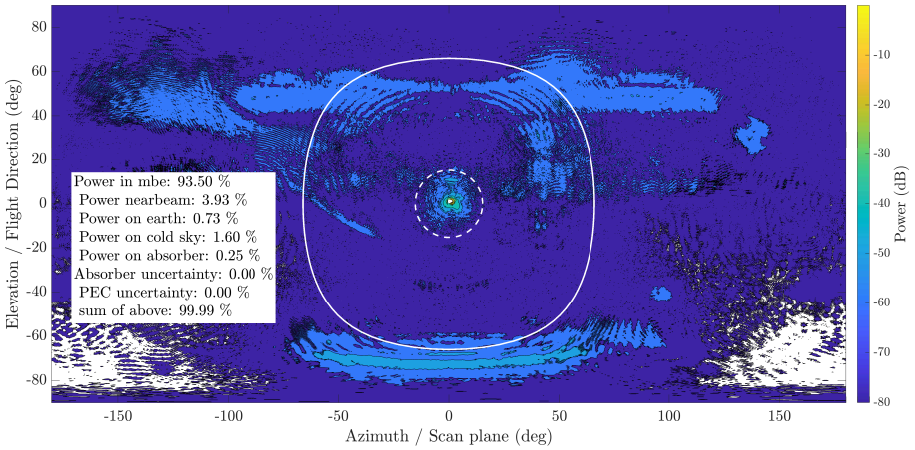

FIGURE 3.24: Full sphere farfield in Azimuth over Elevation coordinates for 165.5 GHz.

3.9.1 Spillover correction

In the third publication associated with this thesis [56] the spillover power fractions shown in Figures 3.22 to 3.24, as well as for other scan angles are presented. A first estimation of the brightness temperature bias induced by the spillover is also presented in the publication. However, the bias estimation assumes the radiometer is already calibrated and determines the bias for each scene due to spillover only. It is also apparent that the cold sky component is a large fraction of the overall spillover. While earth spillover is more complicated to compensate in the calibration, the cosmic microwave background is well characterised and can be compensated, assuming no lunar, solar or other intrusions in the cold space view. This section presents a compensation of the cold sky spillover during calibration and a comparison of the remaining bias against uncompensated calibration.

For this example, the receiver gain G_s is assumed to be linear, its noise temperature T_{rec} is constant and the mainbeam and nearbeam regions of interest are assumed to have the same brightness temperature. In an idealised example, the radiometer has a pencil beam that couples perfectly into the scene or calibration targets. In this case, the measured power by the radiometer for the scene, cold calibration point (cold space) and hot calibration point (OBCT) can be expressed as:

$$\begin{bmatrix} P_{scene} \\ P_{space} \\ P_{obct} \end{bmatrix} = G_s \cdot \begin{bmatrix} T_{scene} \\ T_{space} \\ T_{obct} \end{bmatrix} + G_s \cdot T_{rec} \tag{3.5}$$

and the system gain factor and receiver noise temperatures are as shown previously

$$G_s = \frac{P_{obct} - P_{space}}{T_{obct} - T_{space}} \tag{1.10}$$

$$T_{rec} = \frac{P_{space}T_{obct} - P_{obct}T_{space}}{P_{obct} - P_{space}} \tag{1.11}$$

If the real antenna pattern is considered as shown in Figures 3.22 to 3.24, the brightness temperatures for the different measurements are affected by each other and secondary intrusions from the earth atmosphere and the absorber on the AWS structure. When the real pattern is considered Equation (3.5) becomes

$$\begin{bmatrix} P_{scene} \\ P_{space} \\ P_{obct} \end{bmatrix} = G_s \cdot M_{spo} \begin{bmatrix} T_{scene} \\ T_{space} \\ T_{obct} \\ T_{earth} \\ T_{abs} \end{bmatrix} + G_s \cdot T_{rec} \tag{3.6}$$

where M_{spo} is a matrix of spillover power fractions

$$M_{spo} = \begin{bmatrix} 1-\alpha_1-\beta_1-\gamma_1 & \alpha_1 & 0 & \beta_1 & \gamma_1 \\ 0 & 1-\beta_2-\gamma_2 & 0 & \beta_2 & \gamma_2 \\ 0 & \alpha_3 & 1-\alpha_3-\beta_3-\gamma_3 & \beta_3 & \gamma_3 \end{bmatrix} \tag{3.7}$$

The spillover fractions are taken from the full farfield sphere analysis, each corresponding to the coupling fraction of one particular region. The remaining power is assumed to be coupling into the intended scene. The subscripts denote that each coupling fraction can be different for the respective scan position.

TABLE 3.4: Coupling fractions used for compensation.

50.3 GHz	scene	space α_i	obct	earth β_i	absorber γ_i
scene view	0.9519	0.0261	0	0.0104	0.0116
space view	0	0.9779	0	0.0083	0.0138
OBCT view	0	0.0230	0.9488	0.0114	0.0168

89 GHz	scene	space α_i	obct	earth β_i	absorber γ_i
scene view	0.9666	0.0184	0	0.0098	0.0052
space view	0	0.9849	0	0.0082	0.0070
OBCT view	0	0.0155	0.9677	0.0090	0.0079

TABLE 3.5: Assumed brightness temperatures for each region of interest.

Frequency	T_{scene}	T_{space}	T_{obct}	T_{earth}	T_{abs}
50.3 GHz	254.3 K	1.7 K	293.5 K	235.0 K	283.5 K
89.0 GHz	257.8 K	1.1 K	293.5 K	203.7 K	283.5 K

Using Tables 3.4 and 3.5 as inputs for Equation (3.6) and assuming an arbitrary system gain factor ($G_s = 10$) and receiver noise temperature ($T_{rec} = 300$), measured power values (P_{scene}, P_{space}, P_{obct}) for this simulated radiometer can be generated, which consider the spillover in the antenna pattern. The impact of the spillover bias can be assessed by using Equations (1.10), (1.11) and (3.5) to convert the power back into brightness temperatures, without considering the spillover biases.

Then, as a check if this methodology is sound, Equation (3.6) is used, but considering the full spillover matrix to calculate the brightness temperature of the space and OBCT measurements, including the spillover (T^{spo}_{obct}, T^{spo}_{space}). However, the effect of the spillover needs to be separated from the scene brightness temperature, since it is the final desired quantity. Using Equation (3.10), the expected output should be identical to the initial selected scene brightness temperature.

$$G_s = \frac{P_{obct} - P_{space}}{T^{spo}_{obct} - T^{spo}_{space}} \tag{3.8}$$

$$T_{rec} = \frac{P_{space}T^{spo}_{obct} - P_{obct}T^{spo}_{space}}{P_{obct} - P_{space}} \tag{3.9}$$

$$T_{scene} = \frac{\frac{P_{scene}}{G_s} - T_{rec} - \alpha_1 T_{space} - \beta_1 T_{earth} - \gamma_1 T_{abs}}{1 - \alpha_1 - \beta_1 - \gamma_1} \tag{3.10}$$

Finally, the same method is repeated, but any β and γ are set to 0, therefore only compensating for the cold space spillover in the scene and OBCT view. This will leave a residual bias, since the spillover intrusion of the earth and absorber are still present in the used power values, but not considered in the brightness temperatures.

The results of this methodology are presented in Figures 3.25 and 3.26 for 50.3 GHz and 89 GHz,respectively. Without compensation the bias on the measured scene brightness temperature stays below 1 K for the chosen scene temperature range. For both frequencies, only compensating the cold space spillover results in a significant bias reduction to $\leq$0.15 K. The complete compensation is equal to the input scene temperature, indicating that the compensation approach is working as expected. Although the total spillover is higher for the 54 GHz band, the bias for the 89 GHz band is larger overall.

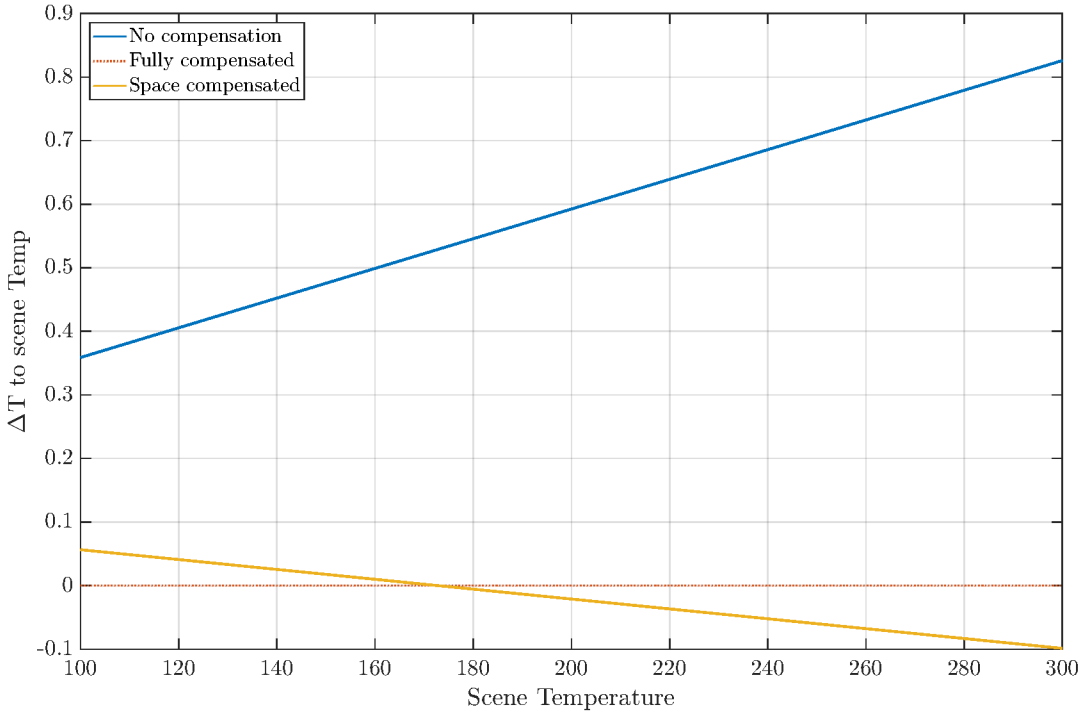

FIGURE 3.25: Brightness temperature bias as a function of input scene temperature after calibration for 50.3 GHz.

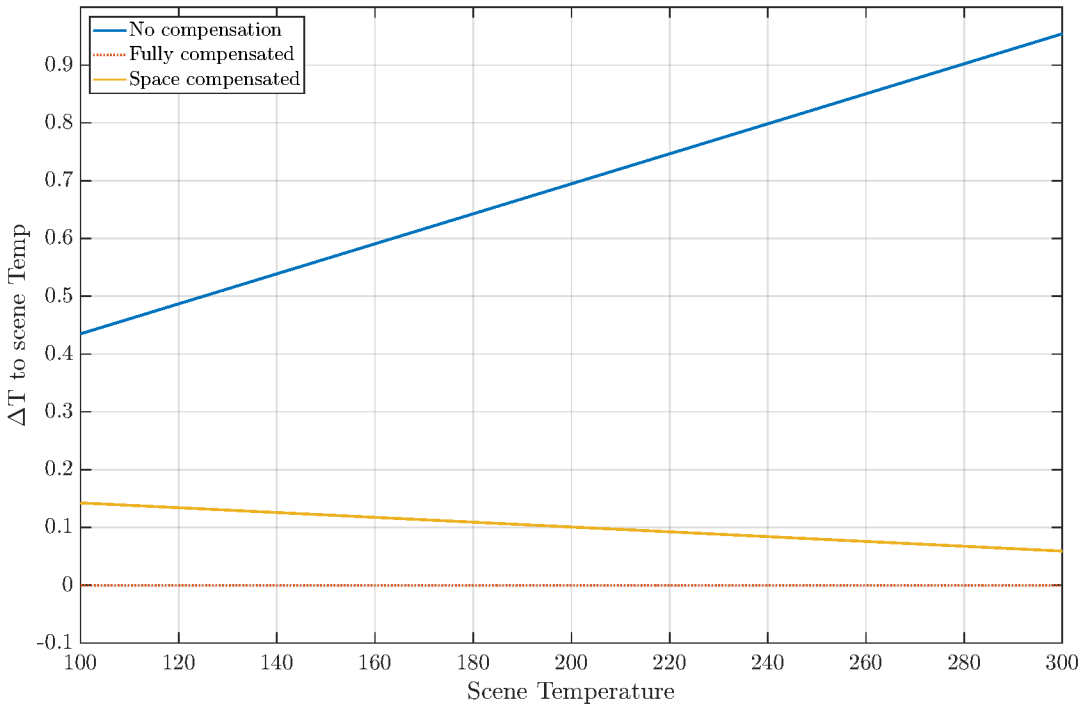

FIGURE 3.26: Brightness temperature bias as a function of input scene temperature after calibration for 89 GHz.

Calibration of the AWS Radiometer

This chapter describes the design and manufacturing of the AWS Onboard Calibration Target (OBCT) and three Onground Calibration Targets (OGCTs). The OBCT serves as the hot calibration point during on-orbit operation. The mechanical design was performed by members of the Space Physics Institute of Bern University. The work on its radiometric design, absorber properties and thermal considerations was published [60].

The Onground Calibration Targets (OGCTs) are used for pre-launch testing and consist of a cold, hot and variable target. As of writing there are no publications covering their design, but they are included here for a complete overview of the contributions of the Institute of Applied Physics (IAP) Microwave Group to the AWS mission. The VTT mechanical design is also from the Space Physics Institute.

4.1 Onboard calibration target

The OBCT for AWS is a passive device with no active thermal control. It consists of a single wedge shaped absorber cavity. The absorber is a three part epoxy based mixture detailed in Section 4.1.1. The absorber is cast on aluminium backing plates (grey in Figure 4.1). The backing plates form an angle of 24°, which has been shown to maximise return loss performance [59]. The wedge cavity is closed by two sheet metal plates covered in Acktar vacuum black IR [61] absorbing paint, but do not contribute to the RF absorption. Two large gold plated aluminium elements provide mechanical strength to the wedge and a mechanical interface to the instrument. The aperture of the OBCT and its optimisation is detailed in Section 3.5. The OBCT mass is just under 1 kg and fits inside a volume of $170 \cdot 110 \cdot 163$ mm. The structure includes weight saving pockets wherever possible to minimise the mass, while maintaining structural strength for the launch envelope.

Figure 4.2 shows the positioning of the four RTDs on each backing plate used to measure the temperature of the absorber. The RTDs are potted in the weight saving pockets, using the epoxy Stycast 2850 which was available and qualified for spaceflight. The tolerance from the manufacturer is class F0.15 according to IEC 60751, which states an accuracy of $\pm(0.15 + 0.002|T|)$ for a temperature T between -30°C and +300°C [62]. However, the operational temperature range for the instrument is much smaller at +10°C to +35°C.

For each backing plate, a D-sub connectors is mounted to the mechanical plate to which the four RTDs are wired. The RTDs are using the four wire measurement technique, which should remove the resistance of the wires from the measurement. Nevertheless, the wires are potted in with the RTDs which thermally grounds them to the same temperature. Once the wires leave the pocket they are wrapped in multilayer insulation (MLI) to prevent radiative coupling to the instrument. The RTDs are split into two redundant sets which each have one sensor on the opposite wedge side. It is anticipated that vertical thermal gradients will dominate, since the wedge is only conductively linked to the baseplate and free floating in temperature at the top. Assuming an isotropic baseplate temperature, horizontal gradients

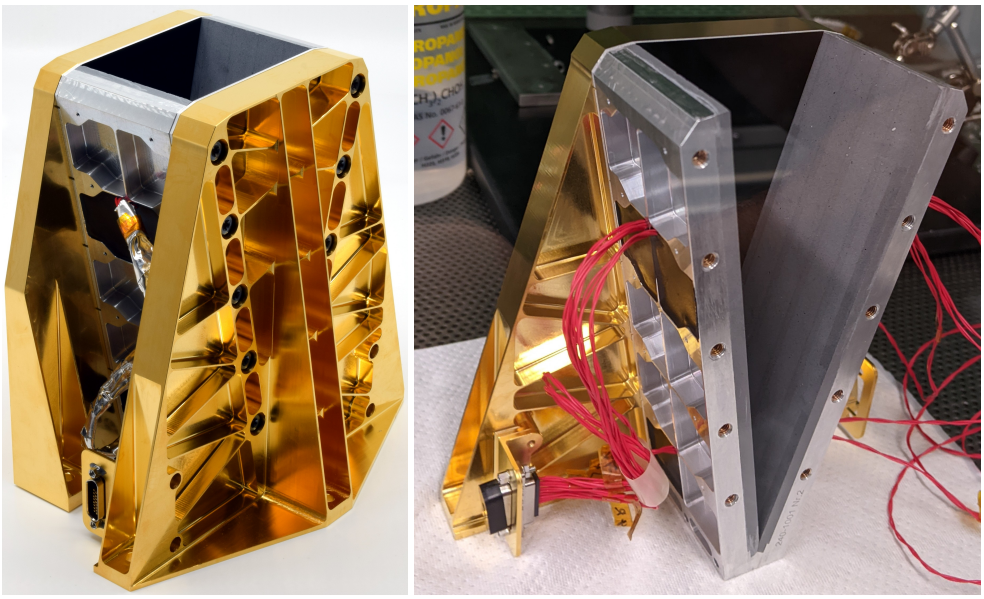

FIGURE 4.1: Picture of AWS onboard calibration target (left) and during assembly (right).

such as between the two wedge sides should be comparatively small, especially since the exterior of the target is gold plated for radiative isolation. The set distribution is shown in Figure 4.2.

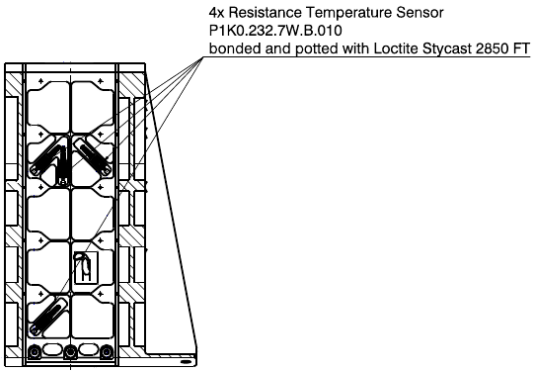

FIGURE 4.2: Schematic of RTD placement on absorber backing plates

4.1.1 Absorber mixture

The previous OBCT developed with the IAP used an epoxy mixture based on Stycast 2850 in combination with Carbonyl Iron Powder (CIP) [59]. The basic concept of using iron loaded epoxy mixtures as microwave absorbers is well established [63, 64, 65, 66]. The mixture was used with two mixing ratios, covering a frequency range from 22 to 664 GHz. The CIP exploits magnetic absorption at the lowest frequencies to reduce the required absorber thickness. However, the AWS band starts at 50 GHz, where magnetic absorption is negligible [67]. Furthermore, the existing mixture provided some manufacturing challenges and its thermal conductivity could be improved [68]. High thermal conductivity is helpful for reducing the temperature gradient between the temperature sensors (typically glued to the back of the absorber mounting) and the epoxy mixture, where the absorption occurs. Lastly, the refractive

index of the mixture was high, meaning more of the incoming beam is reflected at the absorber interface and more reflections are required to achieve high absorption. This project was an opportunity to find a new mixture optimised for the AWS bands, which may offer better performance and workability.

Stycast 1266 [69] was chosen as the new epoxy base for the absorber, since it has a lower refractive index (ε_r) than Stycast 2850 and the added benefit of having ≈30 times lower viscosity. Activated charcoal powder was used as a first additive to provide the required dielectric properties for very high return loss. Boron nitride (BN) was included to improve the thermal conductivity of the mixture. Different experimental mixtures were made using a variety of compounds which won't be detailed here. The initial performance of each mixture was estimated using the volumetric mixing ratio to determine the relative permittivity. They were then cast on a metal plate and the return loss was measured. From this measurement the actual relative permittivity can be calculated. Details of this procedure can be found in [60]. The electrical performance of this mixture is detailed in Section 4.1.2

Significant effort went into refining the manufacturing process to avoid faulty castings and repeatable performance. When casting epoxy, there are a number of common issues which need to be mitigated:

- The mixture is inhomogeneous.
- The mixture contains voids or air bubbles.
- The uncured mixture does not fill corners or small features of the mould.
- The mixture cracks during curing due to shrinkage.

Figure 4.3 shows some of the aforementioned issues for early samples and a picture of the final casting quality that was achieved. To achieve consistent homogeneity, as well as reducing void and air bubbles special equipment was purchased, which mixes the components in vacuum. After the mixture was poured, a small vibration table was used to release any trapped air from the pouring, which occurred in atmosphere. It also helped the mixture flow into the corners of the mould. Afterwards the mixture was cured in an oven at a low temperature, avoiding any thermal shocks. To ensure a repeatable and consistent surface finish, extra material was cast and then later machined down to final thickness. Compared to the previous mixture, the new absorber proved easier to machine.

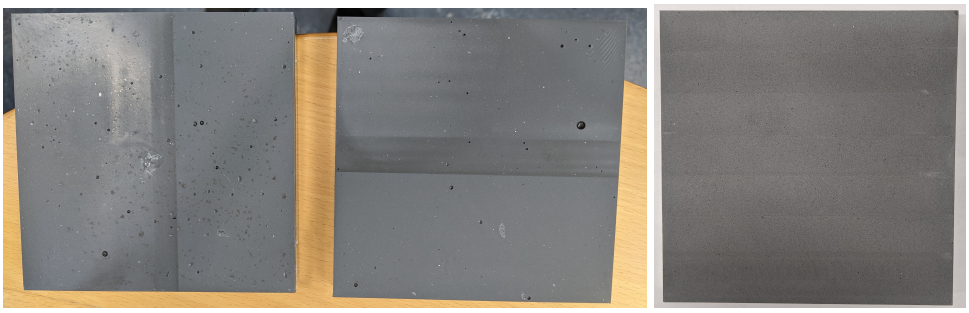

FIGURE 4.3: Picture of Unsuccessful casts with air bubbles and uneven mixing (left, middle) and a successful cast with a homogenous mixture free of air bubbles(right).

But manufacturing only presented a small aspect of the restrictive nature of material development for spaceflight. The absorber needed to have the mechanical strength and adhesion to survive the launch, maintain these properties across the forecast survival temperature range of the satellite, and comply with outgassing requirements. As part of this project, the

absorber underwent an extensive test campaign to prove the above, including vibration and shock testing, adhesion testing and thermal vacuum testing.

4.1.2 OBCT return loss

The performance requirement for the OBCT is a return loss ($|S_{11}|$) of 50 dB or higher. From a system level perspective, the mass of the OBCT has to be minimised. Therefore, it is important to minimise the thickness of absorber. Figure 4.4 is a plot of simulated return loss of the developed AWS mixture for different absorber thicknesses based on a plane wave simulation. The preferred orientation of the wedge cavity for transverse magnetic (TM) is apparent, where the electrical field polarisation is perpendicular to the apex of the wedge and therefore the magnetic field is parallel to the wedge apex. But even for TM the required $|S_{11}|$across the full frequency range is only achieved for a thickness of 6 mm. Below this thickness, there are ripples in the $|S_{11}|$, due to destructive superposition. The reflections of the metal backing overlap with the surface reflections of the absorber and if they are 180°out of phase will cancel each other. This effect depends on the wavelength and absorber thickness. At the larger thicknesses or frequencies where $|S_{11}|$is constant the absorption inside the material is total and the reflection from the metal backing is attenuated. The thick white lines highlight lower thicknesses where the $|S_{11}|$is compliant inside the AWS bands, but not in between them. A final thickness of 3.5 mm was chosen to minimise absorber thickness and therefore mass. This approached relied on the repeatability of the absorber manufacturing and the accuracy of the machining.

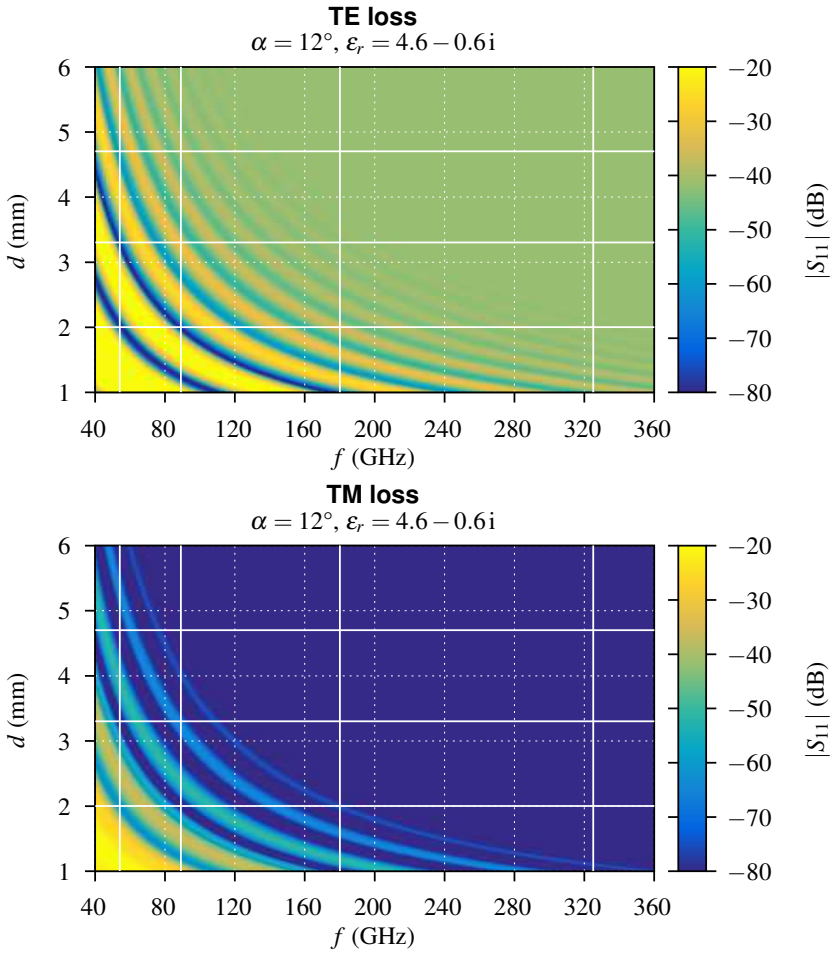

FIGURE 4.4: Simulated return loss of AWS absorber against thickness

The measured return loss of the AWS OBCT (Figure 4.5) demonstrates this effect. The OBCT $|S_{11}|$is compliant across the 54 GHz band but immediately outside the band $|S_{11}|$degrades significantly. No measurements could be conducted at 325 GHz could not be measured directly due to lack of equipment. Instead a measurement was taken at 400 GHz with the rationale that the return loss should be similar, based on the simulations.

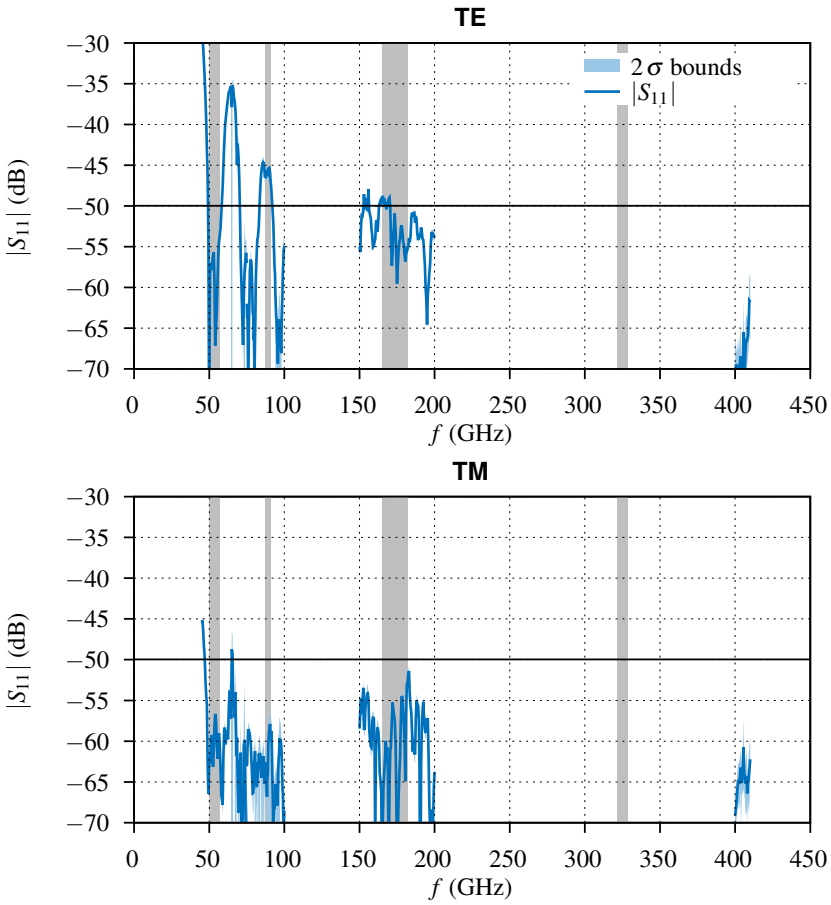

FIGURE 4.5: Measured return loss of the onboard calibration target. Courtesy of Tobias Plüss.

4.2 Onground calibration targets

The OGCTs are used to verify the performance of the radiometer before launch, independent of the operationally used calibration procedure. Therefore, three OGCTs are required to cover the hot and cold calibration point, as well as the "scene" which is the actual measurement taken by the instrument. By comparing the known physical temperature of the scene with the brightness temperature measured by the instrument, the accuracy of the instrument can be verified. For some tests (e.g. non-linearity tests) varying scene temperature are required. Hence the scene calibration target is called the VTT. The VTT is the most challenging target to build, since it needs to achieve accurate thermal stability over a wide range of temperatures, instead of a single point like the hot and cold target. For this instrument, the hot target is not actively temperature controlled, but instead floats at the temperature of the surrounding. Therefore, it is called the ambient target.

Figure 4.6 is a schematic of the onground test setup, using all three OGCTs. The grey circle describes the position of the AWS scanning mirror, which can cover the three targets

in one rotation. Only one viewing angle is shown in the schematic, but all targets have been sized to cover an arc of 10°to guarantee several measurements. Both the ambient and cold target use commercial foam absorber[70] (Section 4.2.3) in a low thermal conductivity expanded polypropylene (EPP) box with an RF transparent window for thermal insulation. In the cold target, the absorber foam is immersed in LN_2 to achieve a physical temperature of ≈77 K.

The VTT uses the same custom absorber mixture as the OBCT, also cast on a metallic wedge. The wedge target is suspended in a dewar chamber with an RF transparent window, above a LN_2 reservoir. The wedge target is thermally linked to the reservoir below it by several metal plates dipping into the LN_2. By varying the height of the reservoir and the number or configuration of plates, the thermal coupling and thus temperature of the absorber can be changed. For the cold and ambient target, no additional optical elements are necessary. But for the VTT, like for the OBCT (Section 4.1), an additional parabolic mirror was required to reduce the size of the beams and hence the wedge. Each target is more closely described in the following chapters.

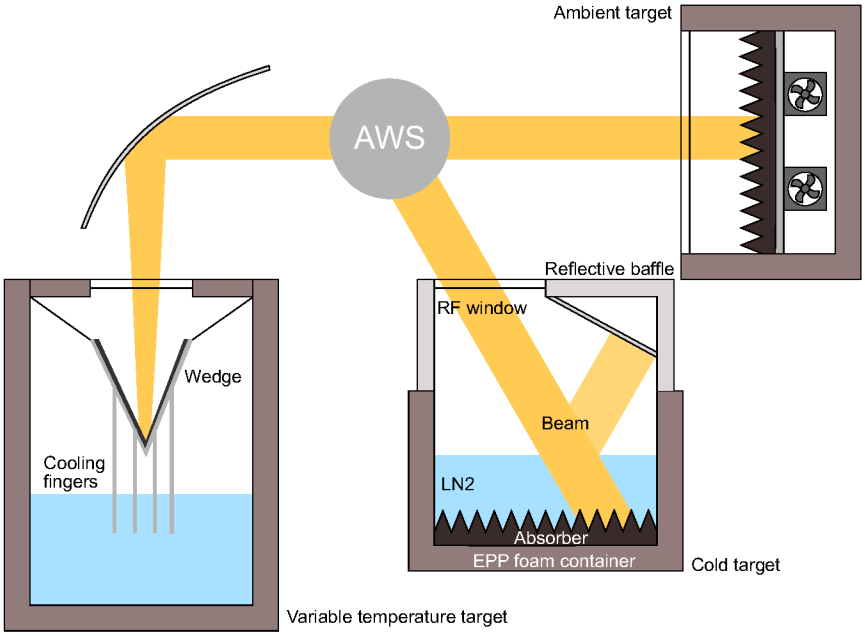

FIGURE 4.6: Schematic of onground testing utilising all three calibration targets. Courtesy of Mikko Kotiranta.

4.2.1 Ambient ground target

The ambient target is a passive device, floating at the temperature of its environment at an expected temperature of ≈300 K. It consists of pyramidal foam absorber (Section 4.2.3) which is glued to a thin metal plate inside an EPP box (number 2 in Figure 4.8). The volume of the box is 49 · 49 · 27 cm and the target weighs ≈5 kg. The box is sealed using a RF window material (number 1 in Figure 4.8) called Plastazote LD15[71]. Although the target is meant to be at ambient temperature, it is still important to seal the absorber box to avoid thermal gradients induced by e.g. air-conditioning or drafts. However, sealing the box means that the air inside could stratify, which in itself could introduce a vertical thermal gradient on the absorber. To avoid this, low power electric fans are fixed to the back of the metal plate, mixing the air inside the box (Figure 4.8 in black on the right). A gap between the backing plate and the box at two sides allows for the air to circulate on both sides of the plate

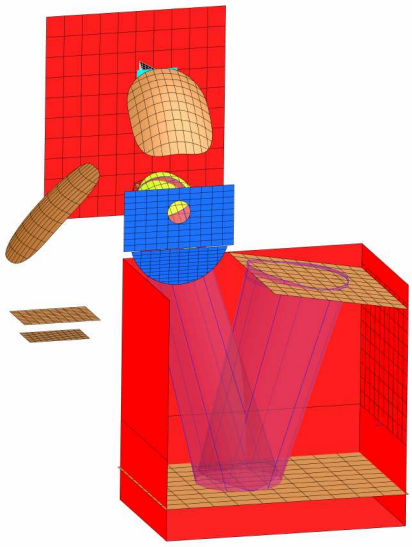

FIGURE 4.7: GRASP model of AWS and the cold target and VTT

(dashed line in Figure 4.8). The metal backing plate and absorber are fixed to the box by four polyoxymethylene (POM) feet, which insulate them from the EPP box.

To measure the temperature of the absorber and monitor any possible gradients, seven PRTs are glued to the metal plate in two diagonals from corner to corner. The PRTs are procured to IEC 60751 standard with an accuracy of F0.15. A sub-D connector provides an electrical interface for the PRTs and fans.

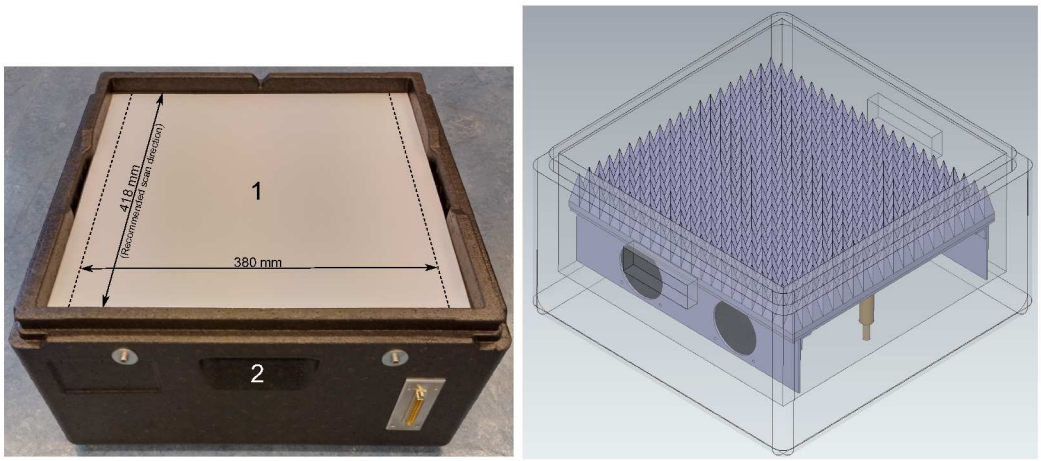

FIGURE 4.8: Picture of ambient OGCT (left) and CAD drawing of absorber mounting inside (right).

4.2.2 Cold ground target

The cold target uses LN_2 to create a low brightness temperature measurement point for the AWS at ≈77 K. Pyramidal foam is glued to the bottom of a large EPP box (625 · 425 · 200 mm) which itself sits in a metallic tub acting as a leak safety barrier. Additional insulating foam lines the metallic tub to further isolate the LN_2 from ambient temperatures, reducing boil-off rate. Since the LN_2 is not in a rigid closed container, it must be kept level and

therefore can only be positioned below the instrument. Due to the change in permittivity between the air (1) and LN_2 (1.2[30] - 1.4[72]), the LN_2 surface induces a reflection. By positioning the cold target slightly off-nadir, the incidence angle on the cold target changes to about 20°, avoiding standing waves. However, the surface reflection must not be terminated at ambient temperature, which would still induce a significant brightness temperature error. A reflective baffle made of metallic composite sitting on top of the EPP box, redirects the surface reflection back to the LN_2 and the cold absorber. The reflective baffle also holds the RF window, which insulates the inside of the cold target from the warm ambient environment.

Instead of using a Platinum Resistance Thermometer (PRT), the temperature of the LN_2 and therefore the absorber can be determined using the Clausius-Clapeyron equation, since it is boiling off continuously. The baffle is sitting loosely on the EPP box, venting the boil-off and keeping the pressure inside the cold target close to the ambient pressure, as proven by measurement. It is sufficient to measure the ambient pressure of the room to determine the LN_2 temperature. The uncertainty of the temperature depends on the accuracy of the pressure sensor. For this cold target the uncertainty is <0.35 K at sea level.

A temperature sensor is positioned just above the tips of the pyramids. It is used as level sensor to determine when the cold target needs to be refilled for long term measurements. The measured temperature increases sharply as soon as the LN_2 level decreases below the sensor. The boil-off rate of the LN_2 was determined by filling the cold target, recording its mass at the beginning and then periodically over several hours. The boil-off rate remained constant at a rate of 0.035 $\frac{\text{kg}}{\text{min}}$. Given the available volume, the maximum time between refills is 8 hours.

Figure 4.9 shows a picture of the assembled cold target. The RF window dimensions (number 2) are marked in the picture. The window size, its positioning relative to the AWS scanning mirror and the required minimum distance between LN_2 surface and scanning mirror were all determined using the GRASP model (Figure 4.7). This was mainly done using raytracing, as the main issue was geometric. The dimensions of the EPP box (behind number 3 in Figure 4.9) was fixed, since it was a commercial product with a fixed size. This fixed the width of the RF window (436 mm), but the length of the window was an open parameter. A longer window would increase the scan arc across the window, but would mean less area for the tilted mirror in the baffle to capture the LN_2 surface reflection.

In Figure 4.7 the 20 dB contour of a gaussian beam emitted from the 54 GHz horn is shown for a scanning mirror position of 10°off nadir. Since the 54 GHz beam is the largest, it was the design constraint. As the scan angle increases the reflection on the LN_2 surface moves to the right. Eventually, the reflection impacts the baffle wall before the reflector and this is why the baffle walls are also electrically reflective. At a scan angle >25°the beam starts to intersect with the RF window. However, the reflection point also depends on the LN_2 fill level and therefore the usable scan range changes slightly based on the fill level of the cold target.

4.2.3 Foam absorber material

Commercial pyramidal foam absorber was chosen for both the cold and ambient OGCTs. There are several advantages of using this kind of absorber instead of the epoxy based absorber mixture for this application. The absorber area for the ambient and cold target is much larger than that of the OBCT and VTT wedges. It would require a lot of time (and money) to mix, cast and machine this area using the epoxy based absorber, whereas the foam absorber is designed as a cost effective solution for large-scale absorbers. Foam absorber has the added benefit of being porous and thus more easily assumes the temperature of the air or LN_2 it is immersed in. It is also lightweight, so has low heat capacity and will follow the temperature

FIGURE 4.9: Picture of cold OGCT.

of its surroundings faster than the solid epoxy absorber plus metal backing. It also reduces the overall mass of the OGCTs significantly, which is important for handling.

The available products were narrowed down to the WAVASORB VHP absorber by Emerson & Cuming [70], which had performed best in laboratory measurements. The absorber was measured across the AWS frequency range and for several incidence angles. Figure 4.10 shows the measurements for perpendicular incidence (ambient target) and 20°(cold target) at horizontal polarisation. Smaller incidence angles and measurements at vertical polarisation were also performed, but for the sake of simplicity are not shown here. As expected with pyramidal absorber, the performance for the two polarisation was similar. VHP-2 and VHP-4 are the same material but with differently size pyramids. VHP-2 was chosen as the pyramids are smaller and would take less LN_2 to completely cover.

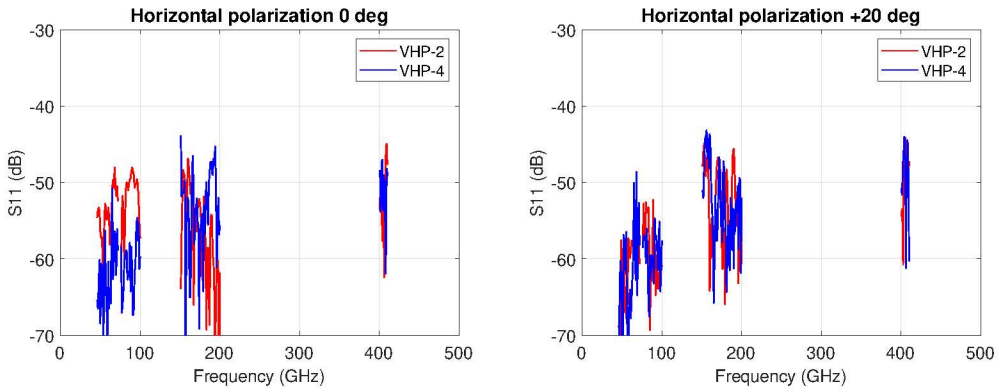

FIGURE 4.10: Measurements of VHP absorber at 0°and 20°incidence angle for horizontal polarisation.

4.3 Variable temperature target

The VTT is the most complex of the three OGCTs, since it needs to operate over a wide range of temperatures. A previous version of a variable target designed in collaboration with IAP required extensive development and precise electronics to have the ability of reaching and holding any temperature from 80 K to 335 K [73]. However, in the case of AWS and the "new space" approach, the VTT had to be designed and manufactured at a fraction of the cost and time.

The fundamental approach is to cool the wedge target using an LN_2 reservoir and allow it to slowly drift up in temperature as the LN_2 evaporates. The wedge target is linked to reservoir by metal plates called "cooling fingers" which are screwed to the backing plate of the absorber at one end and immersed in the reservoir at the other. The minimum temperature reached during test can be controlled by the fill level of the reservoir and the amount/thickness of the cooling fingers. By removing the active thermal control, the complexity of the target is greatly reduced. However, this approach means that the cooling phase of the VTT occurs rapidly with large temperature gradients across the wedge, rendering it unusable. Conversely, the drift up after reaching minimum temperature is very slow, due to the high heat capacity of the wedge assembly. The slow drift results in reduced temperature gradients across the wedge and can be used for radiometric measurements.

The wedge absorber consists of the same mixture used for the OBCT cast onto thick metal backing plates. The cavity is closed by thick metal sidewalls. Unlike the OBCT, a lot of mass is desirable for the VTT wedge to increase the thermal heat capacity, therefore slowing the upward temperature drift and avoiding cold spots on the absorber from the cooling fingers mounted to the backing plates. The wedge is suspended by a thin insulating metal mounting structure inside a commercial dewar. The metal interface is fixed to a metal lid, closing the dewar. The lid has an RF window like the other OGCTs, allowing the radiometer to couple into the wedge. The lid also contains two electrical plugs for the two sets of six PRTs for each wedge side. To detect possible vertical and horizontal gradients, the PRTs are distributed as pairs on three different heights along the height of the wedge. A long pipe is welded to the lid, which can be used to fill LN_2 into the dewar without spilling it onto/into the absorber wedge.

Like the cold target, the VTT reservoir is not closed and needs to be positioned on the ground facing upwards. However, the position below the radiometer is already taken up by the cold target. Therefore, an additional external parabolic mirror was necessary to couple the beams into the wedge aperture with the added benefit of being able to refocussing them, so the size of the wedge aperture could be reduced. The arrangement of the VTT and cold target during test is shown in Figure 4.11. As the scanning mirror rotates across the VTT mirror, the beams move from left to right in the picture across the RF window. The apex of the wedge lies in the same axis, so the polarisation of the beams is perpendicular and the better TM performance is exploited.

Since the VTT has to fit to the existing mechanical ground support equipment (MGSE) built by AAC Omnisys, both the mirror and the dewar assembly include adjustment mechanisms to fine tune the positioning relative to each other and the instrument. For lateral translation of the mirror, the metal struts can be slid along the mounting structure. The tilt can be adjust by loosening to screws on the interface just above the mirror visible in Figure 4.11. The dewar is mounted on a rotation plate which in turn sits on a sliding table to facilitate any configuration in the horizontal plane.

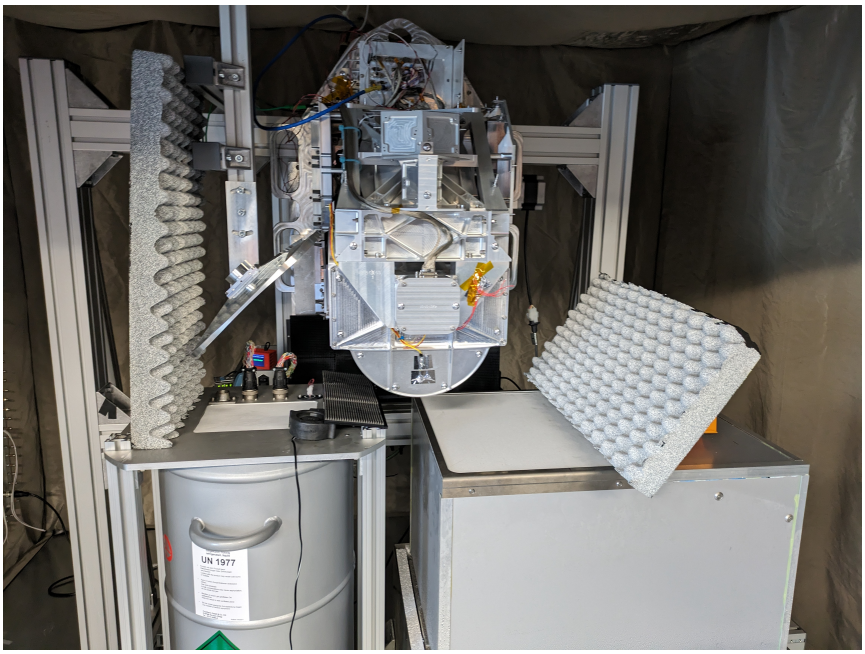

FIGURE 4.11: Preliminary test setup using the VTT in combination with the cold target.

4.3.1 VTT temperature drift and gradients

Figure 4.12 summarises the temperature drift of the VTT over a test duration of 48 hours. The top plot shows the average temperature of the wedge throughout the test, whereas the bottom plot shows the temperature offset of the individual sensors from the average. The sensors are split equally on the back of each absorber plate (A & B), in pairs at three different heights (1-2, 3-4, 5-6). Sensors at the same height along the wedge are drawn in identical colours. The test can be split into three phases:

- LN_2 in the dewar, but not in contact with the cooling fingers
- LN_2 level increased until cooling fingers are immersed
- LN_2 evaporates and cooling fingers no longer immersed

The ideal measurement window for each test phase is highlighted in green in the top plot, and is also recognisable by the lowest temperature drifts. For the first and second phase, where the wedge is cooling down rapidly, the gradients are most extreme and not usable for radiometric measurements. At the end of the first phase the LN_2 has evaporated completely, but due to the high thermal mass of the VTT its overall temperature drift is slow and the gradients in the wedge are $pm0.2$ K or less.

At the end of the second phase the temperature gradients are more pronounced than for the second phase. This is due to the wedge not having reached equilibrium before the LN_2 level decreased below cooling fingers. At that moment, clearly visible at the end of the second green area, there is no strong thermal link between the wedge and the LN_2. Consequently the upward temperature drift increases again. Towards the end of the third phase, a small kink in the average temperature is noticeable, which is the point where the LN_2 has completely evaporated once more.

In general, the spread for sensors at identical heights is smaller than the overall sensor spread, with the notable exception of sensor pair A5/6. When approaching equilibrium the overall constellation of the sensors is similar, indicating predictable behaviour of the wedge.

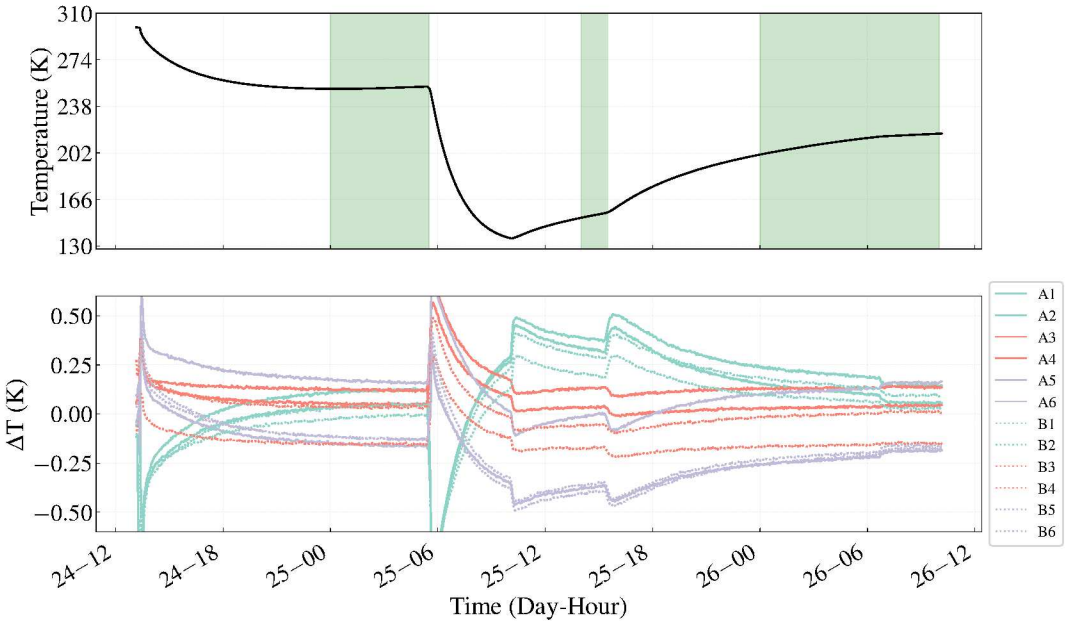

FIGURE 4.12: Average VTT temperature over test duration (top) and sensor temperature delta to average (bottom).

It should be noted that the sensors did not undergo custom calibration, which would increase their accuracy and could decrease the spread of the individual groups. The maximum overall temperature gradient during the usable measurement phases is 0.4 K. The speed of the temperature drifts in the wedge in the highlighted windows is slow enough for radiometric measurements at 0.8, 4 and 16 K over 5.5, 1.5 and 10 hours, respectively. However, the large gradient during phase 2 is limiting performance. A potential solution is to top up the LN_2 during this phase, extending the time the cooling fingers are immersed in the LN_2 reservoir.

Although the VTT can reach representative scene temperatures enabling e.g. non-linearity tests, it comes at the cost of test duration. Furthermore, it is not an automated test and requires monitoring and refilling. It should be noted that the VTT requires the use of at least the cold target at the same time, which requires LN_2 refills after approximately 8 hours. But the cold target is only required for the period where the gradients are in an acceptable window. Overall, there is a significant impact on test duration and the manual input required to conduct a test.

4.3.2 VTT return loss measurements

The $|S_{11}|$was measured using the same approach and equipment as for the OBCT. Please consult Section 4.1.2 for an explanation of the setup and methodology references. Figure 4.13 shows the measured return loss of the VTT wedge for the first three bands. The 325 GHz band was not measured due to time constraints, but as shown in the simulations and OBCT measurements, the return loss stays constant above 200 GHz. Since the VTT wedge is bigger than the OBCT wedge, it was measured at two spots in the aperture. Once in the center and at a position closer to the sidewall, moving along the apex of the wedge. Once again the destructive superposition at the 54 GHz band is apparent, with the $|S_{11}|$being below the target value of -50 dB just inside the band for both positions. For 89 GHz the wedge is also compliant. There is a single non-compliant point at 182 GHz for the wedge center measured at -49 dB.

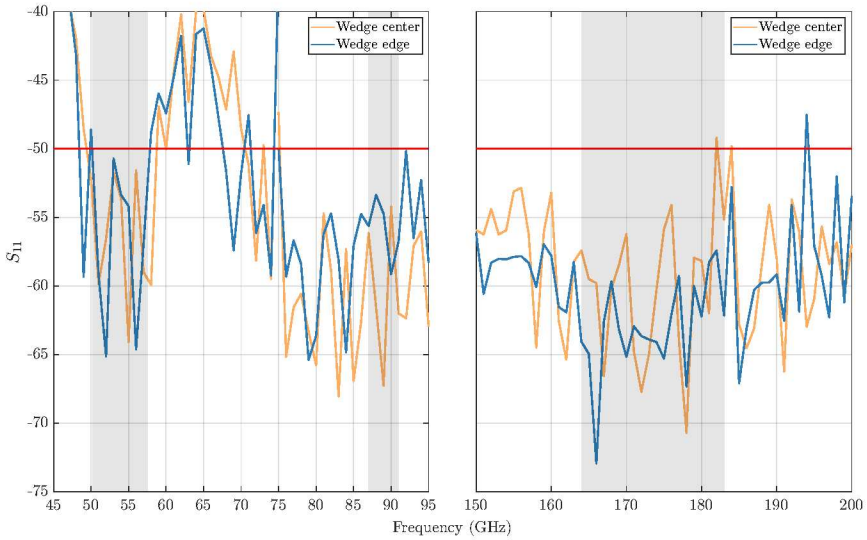

FIGURE 4.13: Measured return loss of VTT absorber wedge for 45 - 200 GHz range. AWS bands highlighted in grey.

4.3.3 VTT GRASP simulations

Since the VTT required a dedicated mirror, some simulations in GRASP were required. The main focus was to minimise the spillover at the mirror, the wedge aperture and ensuring that the RF window was large enough. The GRASP setup is shown in Figure 4.7. The parabolic mirror is in orange on the left in the figure. The RF window and wedge aperture are shown as two flat reflectors below the mirror. The wedge aperture is the lower and smaller reflector. By setting the two surfaces up as reflectors, GRASP will calculate the spillover of these surfaces. Beam positioning was determined by using flat output grids in the same plane as the reflectors.

In Figure 4.14 the tracking of 30 dB contours across the aperture of the wedge can be seen for selected scan angles which differ for each frequency. The selected samples are based on the highest coupling. The y-axis in the plot goes from left to right in Figure 4.11. Like in Section 3.5, the apex of the wedge is drawn by the dotted line. The dashed line shows the outline of the wedge aperture. Similarly to the OBCT, the wedge is shifted relative to the focal point of the VTT mirror indicated by the cross. While the three higher bands fit neatly into the wedge aperture, the 54 GHz contours cross the left edge of the aperture or are very close to it. For more optimal coupling in this band the VTT can be moved along the x-axis. Since the VTT is external ground equipment, this is possible.

Section 4.3.3 shows a summary plot of the total spillover (complete bar) and for each optical element (bar sections). The simulations were performed across a wide scan range to find the complete arc of useable samples. Each row represents the full simulated arc for a single frequency. The majority of the spillover originates from the scanning mirror (blue in plot), with little contribution from the ground-based elements of the VTT. The z-axis is cut off at 10% and some bars are cut off at the top. Like previously mentioned in Chapter 3, the 54 GHz band overall suffers from the most spillover and also the smallest usable scan range. Across all bands the spillover decreases from low to high band. For 325 GHz the spillover is negligible and it has the widest scan arc, with further possible samples past 100°.

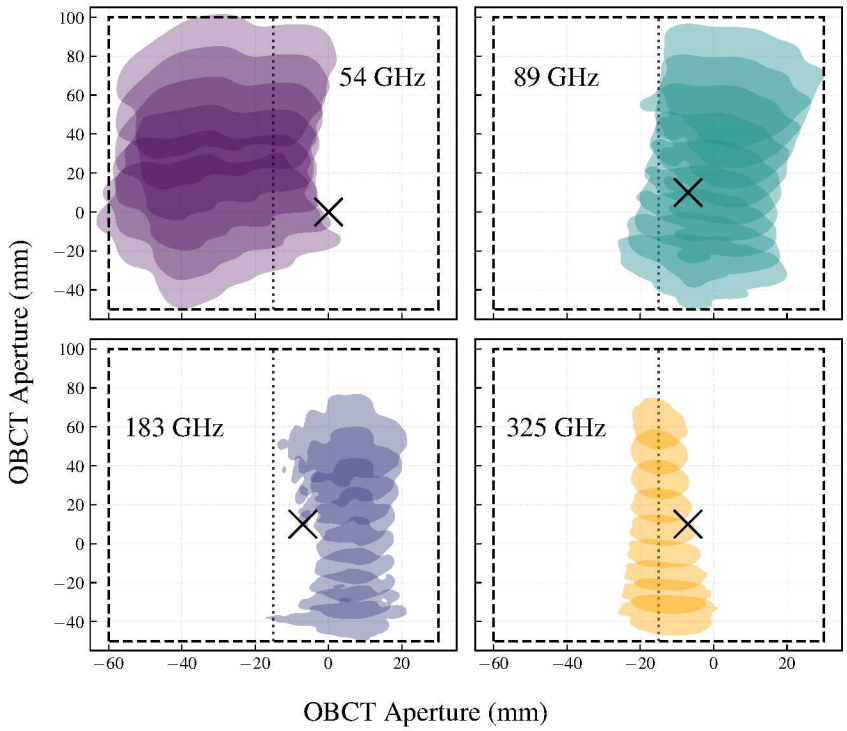

FIGURE 4.14: Beam contours (30dB) across VTT wedge aperture. Every second contour is plotted.

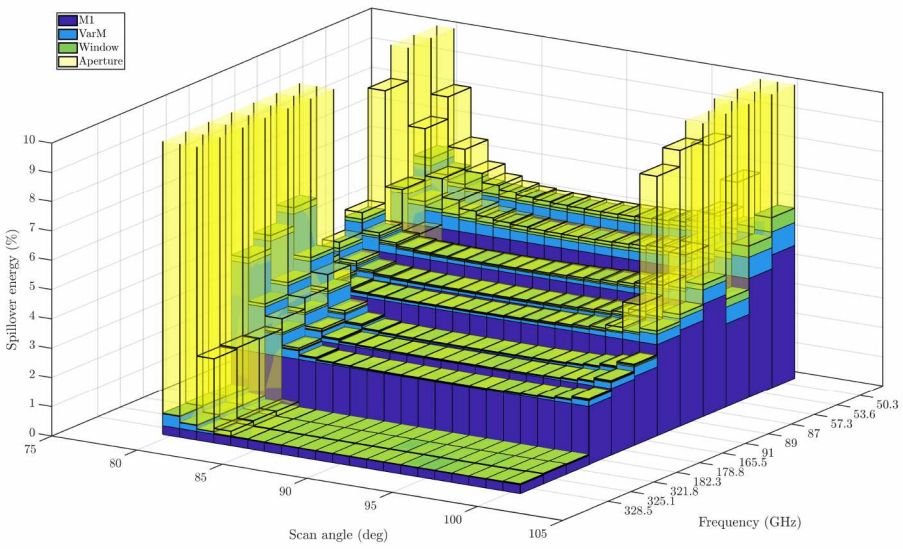

FIGURE 4.15: Spillover per element, scan angle and frequency. Each color corresponds to a different element.

Conclusion

The AWS radiometer and its novel quasi-optical design in the context of other cross-track scanning radiometers was presented. It consists of a feedcluster directly illuminating the scanning mirror, which results in a smaller, low cost instrument. It was shown that through optimisation of the feedcluster positioning, as well as the AWS reflectors it is possible to mitigate, but not eliminate the scan angle dependency of the instrument performance characteristics, such as spillover.

It was shown that due to the higher spillover, especially at the lower frequencies, the structure of the radiometer has a noticeable effect on the farfield pattern of the radiometer. A first analysis of the brightness temperature error due to spillover is presented using the full farfield sphere. Furthermore, the scan angle dependent rotation of the individual beam offsets around the scanning mirror boresight was characterised. Both effects need to be taken into account during operational use in order to produce accurate and correctly geolocated data.

Lastly, the calibration targets of AWS for both onboard and onground use were presented. The OBCT consists of a single large wedge cavity, which is a novel design for spaceborne operational radiometers. The absorption is provided by a custom made epoxy based absorber mixture, designed to improve return loss and thermal conductivity over previous absorbers. Measurements of the return loss for the OBCT were shown to be at -55 dB or better in the AWS frequency bands.

Three onground targets were presented, each providing a hot, cold or variable scene calibration point for the AWS. The hot and cold calibration targets use foam based commercial pyramidal array absorber and the VTT uses the same wedge shape and epoxy based mixture as the OBCT. Further return loss measurements for the VTT were presented, as well as quasi-optical simulations of its coupling to the AWS via an additional reflector. Temperature measurements of the VTT taken during testing showed thermal gradients of 0.8 K or less in relevant phases of the test.

5.1 Impact of this thesis

A large part of the simulations produced during this dissertation are used in the operational processing of the data to create the level 1b data products. The farfield antenna patterns and their rotation are used for accurate geolocation of the raw data. The spillover breakdowns contribute to the calibration of the received radiances in orbit. The addition of the reflective cap to the roof structure reduces the more varied earth spillover in favour of predictable cold sky spillover.

The OBCT designed and built as part of this thesis proved the validity of both the wedge concept and the new epoxy absorber mixture. The high return loss of the target contributes to an accurate calibration of the instrument. The ground targets described in this thesis were used to demonstrate compliance of the instrument to its requirements.

5.2 Suggestions for future work

It is evident that spillover is the major performance limitation of the AWS radiometer. Specifically, the lowest frequency feedhorn (50-58 GHz) suffers the most in the current configuration. A potential improvement of the current design is a dual-band feedhorn antenna covering both the 54 GHz and 89 GHz bands. From a quasi-optics perspective, this would be a straightforward way of improving the spillover and beam ellipticity over the current design. Another option would be to use a corrugated feedhorn for the 54 GHz or even higher frequency horns, which can achieve very high gaussicity compared to smooth walled spline horns.

AWS launched just prior to the publication of this thesis and some commissioning activities are still outstanding. The cap which was included later in the project is key to reducing incident spillover on earth which is very difficult to compensate due to the brightness temperature variations. A series of slew manoeuvres are planned to verify the spillover lobe exists and is positioned as predicted by the simulation.

For operational use it is not feasible to use a complete brightness temperature map of the earth for each position and scan angle of the radiometer. However, expected brightness temperature ranges could be extracted from atmospheric simulations for the AWS channels and used to define the measurement error induced by the earth spillover for different seasons, orbit positions and scan angles. Provided the cold sky and absorber spillover is already compensated, this is the final step for complete bias compensation of the AWS radiometer.

Publications

Peer-reviewed articles

Albers, R., A. Emrich and A. Murk. 'Antenna Design for the Arctic Weather Satellite Microwave Sounder'. In: *IEEE Open Journal of Antennas and Propagation* 4 (2023), pp. 686–694. ISSN: 2637-6431. DOI: 10.1109/OJAP.2023.3295390.

Albers, R., T. Plüss, L. Eggimann and A. Murk. 'Development of the Onboard Calibration Target for the Arctic Weather Satellite'. In: *IEEE Transactions on Geoscience and Remote Sensing* (2024), pp. 1–1. DOI: 10.1109/TGRS.2024.3436517.

Albers, R., M. M. Bilgic, K.-E. Kempe, A. Bell and A. Murk. 'Spillover analysis and main-beam characterisation of Arctic Weather Satellite radiometer using method of moments'. In: *IEEE Open Journal of Antennas and Propagation* (2024), pp. 1–1. DOI: 10.1109/OJAP.2024.3462601.

Co-authorship of peer reviewed-articles

Albers, R., H. Andrews, G. Boccacci, V. D. Pires, S. Laddha, V. Lundén, N. Maraqten, J. Matias et al. 'Magnetospheric Venus Space Explorers (MVSE) mission: A proposal for understanding the dynamics of induced magnetospheres'. In: *Acta Astronautica* 221 (2024), pp. 194–205. ISSN: 0094-5765. DOI: https://doi.org/10.1016/j.actaastro.2024.05.017. URL: https://www.sciencedirect.com/science/article/pii/S0094576524002674.

E. Sauvageat, **Albers, R.**, M. Kotiranta, K. Hocke, R. M. Gomez, G. E. Nedoluha and A. Murk. 'Comparison of Three High Resolution Real-Time Spectrometers for Microwave Ozone Profiling Instruments'. In: *IEEE Journal of Selected Topics in Applied Earth Observations and Remote Sensing* 14 (2021), pp. 10045–10056. DOI: 10.1109/JSTARS.2021.3114446.

Talks and poster

Albers, R., M. M. Bilgic, M. Whale and A. Murk. *Method of Moment Simulation of Full Arctic Weather Satellite Structure*. Talk at 18th European Conference on Antennas and Propagation. Mar. 2024. DOI: 10.23919/EuCAP60739.2024.10501048.

Albers, R., M. Kotiranta, A. Emrich and A. Murk. *Otical Design of the Arctic Weather Satellite Microwave Sounder*. Talk at 17th European Conference on Antennas and Propagation. Mar. 2023. DOI: 10.23919/EuCAP57121.2023.10132949.

Albers, R. *Optics for the TEMPERA-C polarimetric middle atmosphere temperature sounder*. Talk at International Symposium on Space Terahertz Technology. 2022.

Albers, R. *An overview of the Arctic Weather Satellite radiometer*. Seminar at Institute of Applied Physics, Bern. 2021.

Albers, R., M. Kotiranta, T. Pluess and A. Murk. *Antenna simulations and radiometric calibration of the Arctic Weather Satellite*. Seminar at Institute of Applied Physics, Bern. 2024.

Albers, R., M. Kotiranta, T. Plüss, K. Kempe, A. Emrich and A. Murk. *Onground Calibration of the Arctic Weather Satellite Microwave Radiometer*. Poster at 17th Specialist Meeting on Microwave Radiometry and Remote Sensing of the Environment. 2024.

IEEE Open Journal of
Antennas and Propagation

Received 3 March 2023; revised 7 July 2023; accepted 10 July 2023. Date of publication 14 July 2023; date of current version 2 August 2023.

Digital Object Identifier 10.1109/OJAP.2023.3295390

Antenna Design for the Arctic Weather Satellite Microwave Sounder

ROLAND ALBERS[1], ANDERS EMRICH[2], AND AXEL MURK[1]

[1]Institute of Applied Physics, Bern University, 3012 Bern, Switzerland

[2]AAC Omnisys, 421 32 Västra Frölunda, Sweden

CORRESPONDING AUTHOR: R. ALBERS (e-mail: roland.albers@unibe.ch)

ABSTRACT The Arctic Weather Satellite (AWS) is a prototype mission for an operational constellation of microwave sounders, complimenting existing meteorological sounders. The AWS is a microsatellite with a single cross-track scanning radiometer operating in the 54, 89, 183 and 325 GHz bands. Due to the small platform size, the core design focus of the radiometer's quasi-optics is less complexity and a more compact setup than comparable spaceborne microwave sounders. To achieve this, the instrument utilises a splitblock feedarray which directly illuminates the off-axis parabolic scanning reflector. A secondary parabolic reflector is used to couple into a wedge-shaped load which is used for calibration in combination with cold sky measurements. The main challenge for instrument performance is that only one of the four horns can be located in the focus of the scanning reflector. Consequently, scan angle dependent spillover variations and beam asymmetries can occur. This paper details the simulation and optimisation efforts of the quasi-optics to minimise the aforementioned effects.

INDEX TERMS Antennas, millimeter-wave (mm-wave), satellite, splitblock, quasi-optics.

I. MISSION BACKGROUND

MICROWAVE sounders are the most impactful contributors to numerical weather prediction (NWP) [1]. Typically, operational microwave sounders are launched as part of a collection of meteorological instruments on a large satellite platform which restricts both the number of sounders operating concurrently and the rate at which they are replaced due to the slow and costly nature of such major missions. However, there is a need for more frequent measurements in the microwave frequency range, specifically in the 50, 89 and 183 GHz bands [2]. While geostationary satellites offer continuous (but not global) measurements, they are limited in their resolution which is an important driver for NWP due to the height of the orbit and cannot view the high latitudes. Sun-synchronous orbits (SSO) are used by the major meteorological missions to benefit from increased resolution (from being in low earth orbit) and coverage for the high latitudes, as well as the rest of the globe. The European Organisation for the Exploitation of Meteorological Satellites (EUMETSAT) is in the early phase of a microsat constellation program called EPS-Sterna which would be used for operational forecasting in combination with existing meteorological programmes. The constellation would improve global NWP accuracy and provide nowcasting [3] capabilities in the arctic region with very short revisit times in the high latitudes, as well as support global efforts on climate change monitoring. The Arctic Weather Satellite (AWS) is the baseline satellite for this constellation.

A. EXISTING CROSS-TRACK MICROWAVE SOUNDERS

EUMETSAT operates the European meteorological satellites (MetOp) in SSO used for operational forecasting and NWP. The MetOp program is about to be upgraded with a new fleet of satellites under the MetOp-second generation (MetOP-SG) mission. The operational atmospheric sounder for the MetOp-SG mission is the Microwave Sounder (MWS) instrument which is a cross-track scanning radiometer covering 5 bands (24, 50, 89, 164-183 and 229 GHz) with a total of 24 channels [4]. The MWS design is driven by a very stringent beam co-alignment requirement, which allows for easy comparison of the different bands and/or combined data products. This is achieved by overlaying individual beams

IEEE Open Journal of Antennas and Propagation

onto a single flat scan mirror using a sequence of dichroic plates, polarising grids and mirrors [5]. Dichroic plates are needed as some bands are measured in both polarisations using a separate feedhorn for each polarisation. While the data products are more easily extracted with this setup, it results in a large and complex quasi-optical setup. For the MWS this is acceptable since it is mounted on a large satellite platform (MetOP-SG Sat-A) as part of an operational suite of 8 instruments. Only one Sat-A will be in use at a time, resulting in relatively long revisit times.

The main American operational microwave radiometer is the Advanced Technology Microwave Sounder (ATMS). Like MWS, it is a cross-track radiometer operating in similar frequency bands (30, 50, 89, 164-183 GHz). However, the ATMS design is more compact compared to the MWS, partially due to lacking the 229 GHz band, but there are some key differences in the quasi-optical design as well. Instead of overlaying all beams, ATMS splits its bands into two sets each with their own flat scanning mirror [6]. The two scanning mirrors are driven by the same motor, ensuring synchronicity. Each scanning mirror then couples into their respective stationary parabolic mirror. After the parabolic mirror the two bands of the set are separated using a polarising grid, which is less lossy than a dichroic plate but limits the bands to a single polarisation. The advantage of not combining all the beams is a reduced volume compared to MWS. ATMS is part of the payload of two satellites: NOAA-20 and Suomi NPP with a third (NOAA-21) recently launched. NOAA-20 and Suomi NPP share the same SSO but are 180 degrees phase shifted, which results in better revisit times than MetOP-SG.

The Time-Resolved Observations of Precipitation structure and storm Intensity with a Constellation of Smallsats mission (TROPICS) from NASA is using similar bands, but mounts the radiometer on six dedicated cubesats in three LEO planes. The baseline median revisit time is 60 minutes in the tropics, which is needed to observe the rapidly changing cyclones occurring in this region. The TROPICS radiometer covers 4 bands (90, 118, 183, 205 GHz) with a total of 12 channels [7]. TROPICS uses very compact optics that fit in a 1U cube. By using a wideband feedhorn for the 90 and 118 GHz bands with a second feedhorn for 183 and 205 GHz bands and co-aligning them using a polarising grid, the volume of the optics is further reduced than for ATMS. Additional space saving is achieved by using a single static parabolic reflector and rotating the entire cube housing the optics. However, this severe size restriction limits TROPICS in both frequency (lower frequency horns are too big) and in available bands (1U could not accommodate more feedhorns). Unlike the previous two missions, TROPICS is a science based mission and not being used operationally for meterological forecasts [7].

The key driver for the quasi-optical design of ATMS, MWS and TROPICS is the beam alignment. Combined data products and other comparisons require measurements of the same location. Consequently, one solution is to build large and intricate quasi-optics (MWS), or limit the amount of bands (TROPICS) or a compromise between the two (ATMS). The new Arctic Weather Satellite (AWS) mission is using a different approach to this design trade-off.

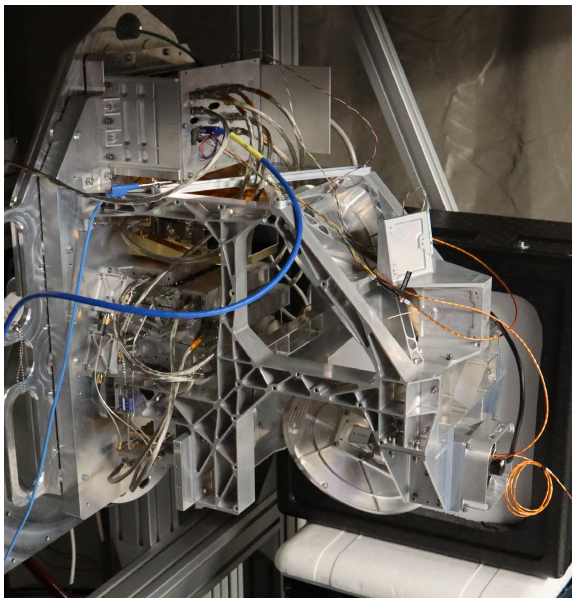

FIGURE 1. Picture of AWS radiometer prototype at AAC Omnisys.

B. THE ARCTIC WEATHER SATELLITE MISSION

The AWS is a prototype for a future constellation for EUMETSAT called EPS-Sterna. The constellation consists six satellites on two SSO planes with a revisit time in the high latitudes of 60 minutes or less. Each satellite carries the same instrument: A cross-track scanning microwave radiometer covering the 50, 90, 165-183 and 325 GHz bands [8]. These four bands are split into a total of 19 channels (8, 1, 6, 4 channels from lowest to highest frequency band) which are used to extract temperature and water vapour profiles, as well as cloud liquid water content and precipitation. Including the 325 GHz band is a distinguishing addition to the AWS radiometer over the other operational radiometers. The AWS mission is intended to be a fully operational constellation used for regular forecasting and nowcasting in the arctic region and will be the first of its kind. The AWS radiometer, built by AAC Omnisys, covers its four bands (54, 89, 183, 325 GHz) with a feedhorn for each band. Due to the large number of satellites required, the AWS radiometer cannot be of the same size and complexity as the MWS, as costs would be prohibitive. Nevertheless, the radiometer performance should be similar to MWS levels to be useful operationally. Instead of overlaying the beams using dichroics or polarising grids, the feedhorns are arranged adjacent to each other in a feedcluster, directly illuminating the primary reflector (Fig. 1, 2). This significantly shortens

the path length and compacts the quasi-optics. The primary reflector is an off-axis parabolic reflector and rotates continuously to facilitate the scanning as well as calibration measurements. A secondary static reflector is located 180° from the nadir view Fig. 3. The calibration reflector covers a scanning range of 10° with a super-elliptical rim to provide sufficient measurements of the on-board calibration target (OBCT) which is positioned underneath the calibration reflector, nested inside the instrument to protect it from a direct spaceview. The OBCT consists of a wedge shaped epoxy based absorber cast on aluminium backing plates and is used as the "hot" calibration point. Cold sky measurements are used for the cold calibration point. Since the feedhorns are not co-aligned on the focal axis of the reflector, they introduce asymmetries and other imperfections in several aspects of the quasi-optical design, which will limit its performance compared to other solutions (e.g., MWS). Furthermore, the beams diverge on the ground track and measurements taken at a given moment will not be of the same location for each band. Consequently, each measurement needs to be geolocated individually so data products can be produced. Measurements will be separated in time by up to a couple of seconds, but this is not a concern as the timescales of relevant meteorological processes are much larger. For accurate geolocation and consideration of the aforementioned effects, the quasi-optics are modelled in detail so they can be accounted for in software to improve the performance of the AWS. This paper summarises the efforts of simulating and optimising the AWS quasi-optical setup, using the CHAMP and GRASP software packages from TICRA. Only the lowest, highest and middle channel for each band were simulated. For the 89 GHz band (single channel) the upper and lower bandlimits were simulated.

II. FEEDCLUSTER DESIGN

While corrugated horns are widely used for microwave radiometers, their manufacturing is costly and complex. Circularly symmetrical horn designs in a splitblock design were chosen, which are simpler and faster to manufacturer [9]. The splitblock consists of three metal blocks, which are stacked on top of each other to form four feedhorn cavities. The plane where the faces of two blocks meet is called the splitplane and must contain the axis of symmetry for any horn it intersects, as the splitblock also contains the waveguide transition and a rectangular waveguide bend to interface with the receivers (Fig. 5). The splitplane must be located in the E-plane of the waveguide to minimise losses. However, this restricts the degrees of freedom for the horns in the splitblock, as the aperture face has to be perpendicular to the splitplane to guarantee the correct intersection.

A. FEEDHORNS

The primary design concern for the feedhorns is the trade-off between aperture size (and thus offset to the focal axis) and directivity needed for the required footprint size. Secondly, since all horns share an aperture plane, the respective phase centers should be as close to each other as possible to prevent degraded performance of individual feedhorns. Finally the horn designs are optimised to achieve a high Gaussian coupling efficiency (95.5% and higher). Smooth walled spline horn profiles provided by Omnisys AAC were imported into CHAMP and simulated. The resulting beam patterns, which were consequently used in the GRASP simulations, are shown in Fig. 4.

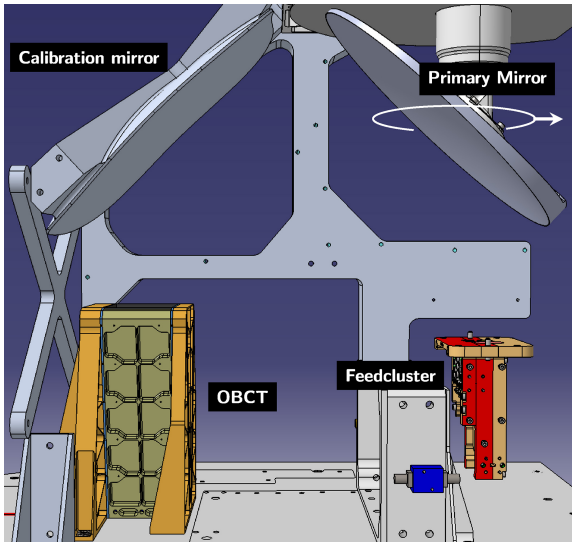

FIGURE 2. Overview of optical elements of the AWS radiometer. Scan plane and nadir direction indicated by white ellipse and arrow.

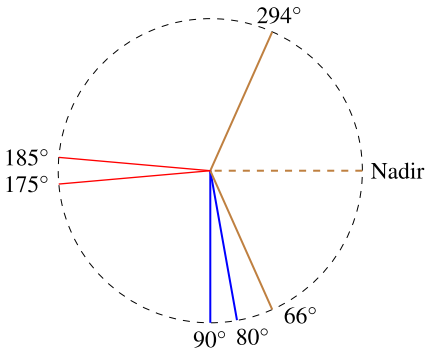

FIGURE 3. Scanning angle breakdown. Earth view in brown, cold sky in blue and calibration reflector in red.

B. FEEDCLUSTER OPTIMISATION IN FOCAL PLANE

The precise packing of the feedcluster is nevertheless challenging. The final beamshape symmetry leaving the primary reflector is dictated by the distance of the horn from the focal point of the mirror in the focal plane. It is important to keep in mind that instead of absolute distance, the separation should be measured in wavelength of the respective horn, as this dictates the extent of beam distortion.

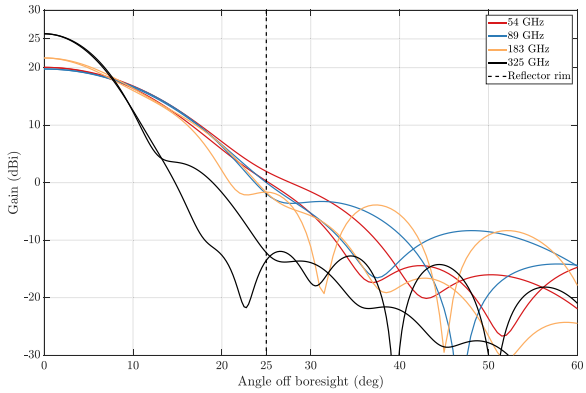

FIGURE 4. Antenna pattern of final feedhorns in E- and H-plane generated using CHAMP.

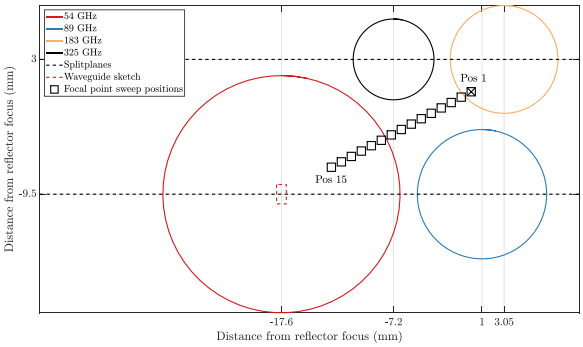

FIGURE 5. Plot of feedcluster and focal point sweep Positions. Waveguide sketch not to scale.

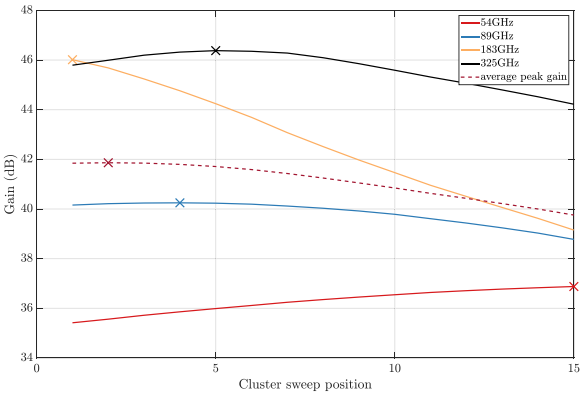

FIGURE 6. Peak gain in mid band in the farfield of the primary reflector as a function of focal point position.

Additionally, the effect of the beam distortion depends on the beamshape of the horn, so not all horns will be affected equally. Initially the use of iterative algorithms was considered to determine the optimal packing, but this was ultimately rejected as there was a lack of means to accurately quantify one horns relative importance over another. Furthermore, the packing problem is compounded by the fact that two feedhorns need to share a splitplane through their midpoint while they cannot extend through the splitplane of the other two feedhorns. Furthermore, the option to tilt the individual horns so they point towards the reflector was considered. This did not improve beamshape for any band, although it did reduce the spillover for the 54 GHz band by 1%. However, this spillover improvement was limited to 54 GHz and came at a cost of more divergent beam pointing. Given the added complication for the configuration of the splitplanes in the splitblock and the subsequent impact on receiver interfaces with the splitblock, tilting the feedhorns was disregarded.

Fig. 5 shows the final feedcluster packing which was used. Having decided on a packing configuration, the next step was to decide where the focal point of the reflector should be located in the aperture plane of the feedcluster. As the 183 GHz horn performance was deemed most critical the initial position of the focal point was close to its center. This position put the 54 GHz horn at the furthest wavelength number away from the focal point.

By sweeping the focal point along a straight line between the two horns centers the trade-off in performance between the 54 GHz and 183 GHz horns can be quantified. Only points on this line were considered, since it was the solution that affected the performance of the other two horns the least. Fig. 6, showing the peak gain for each horn in the farfield of the primary reflector, demonstrates the effect well. Peak gain for the 183 GHz beam decreases steadily as the focus is moved further away from it, whereas the 54 GHz beam increases as the focal point is moving closer to it, but the decline in 183 GHz is larger than the gain for the 54 GHz band. Both 89 and 325 GHz horns show a maximum gain value at the focal point which corresponds to minimum separation to the focal point. Since the gain is directly linked to the full-width half maximum (FWHM) of the beam, which in turn is specified in the radiometer's requirements, large variations are not acceptable.

Lastly, the circularity of each beam in the farfield of the primary reflector was investigated (Fig. 7). This parameter was also controlled by requirements from the end-user, placing a deviation limit from the nominal circular footprint size. Assuming a circular footprint, this deviation can be controlled using gain variations in the feedhorns. However, due to none of the horns being in focus and hence not symmetric around the focal axis, it is to be expected that beam deformation occurs.

The 89 and 325 GHz horns both show the by now familiar effect of peak values near their closest proximity position. The 183 GHz maximum circularity is also at the expected position, but its behaviours across the positions is unexpected. One would have expected a drop-off similar to 89 GHz and not a cyclical behaviour.

Averages of each parameter are also plotted in the figures to gain an appreciation of how the system changes

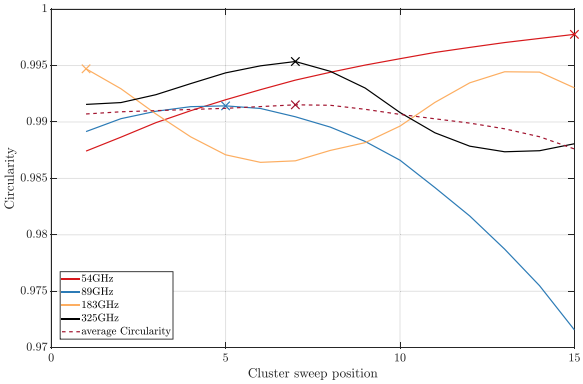

FIGURE 7. Circularity in mid band in the farfield of the primary reflector as a function of focal point position.

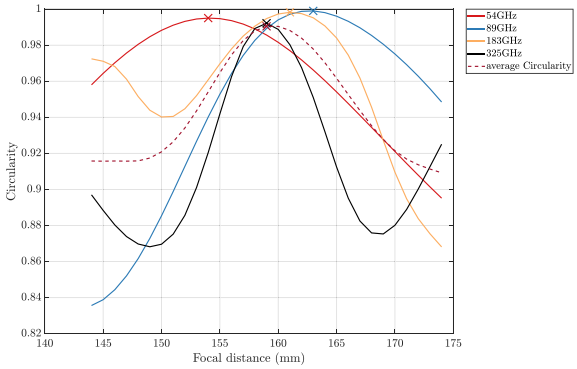

FIGURE 8. Farfield beam circularity as a function of distance between reflector and feedcluster.

as a whole as a function of cluster position. However, this cannot be used as a direct criteria for system performance, as certain frequency bands are more critical to the instrument and thus their performance weighs more heavily in consideration. On balance, the first sweep position was considered the most suitable since it delivers peak performance for the 183 GHz band, with minor degradation to no variation in 89 and 325 GHz. Its clear downside is the degraded performance in the 54 GHz band. Nevertheless, the 54 GHz performance was still acceptable and improving it is not worth the sacrifices in the other bands.

C. FEEDCLUSTER OPTIMISATION ALONG FOCAL AXIS

When optimising the feedhorns, it became clear that forcing a common phase center location in each horn, while maximising other performance criteria, was too restrictive. Hence each horn as a different phase center location, along its axis of symmetry inside the horn. In order to find the optimum for the overall feedcluster, the 3dB contours of each horn in the farfield of the reflector were calculated as a function of distance to the primary reflector. The key performance criteria is the circularity of these 3dB contours and can be seen in Fig. 8. The dashed line shows the average circularity of which the peak was chosen as the focal distance for the instrument. The plot also illustrates how each horn shows a wavelength dependent drop off. The width of the peak is thinnest for 325 GHz and proceeds to get wider, as wavelength increases to 54 GHz. The final focal distance chosen was 159 mm, as it yielded the highest average circularity of the beams. The circularity was calculated using [10]:

$$\text{Circularity} = \frac{4\pi \cdot \text{Area}}{\text{Perimeter}^2} \quad (0 < \text{Circ} < 1) \qquad (1)$$

where a perfect circle has a value of 1.

III. PRIMARY REFLECTOR

The main design challenge for the primary reflector is the large offset of the 54 GHz horn from the reflector focal point. While the gain of the 54 GHz feedhorn is matched to the reflector diameter of 160mm, the offset causes the feedhorn pattern to under-illuminate one side of the reflector and to spill past the reflector on the other side. An additional effect occurs due to the rotation of the primary reflector. As the feedhorn is offset from the axis of rotation of the reflector (its focal axis), it will lead to changes in the amount of spillover as a function of the scan angle. This occurs due to the rim of the mirror moving in the field of view of the feedhorn. If the spillover intensity varies between the calibration measurement and the earth measurement, it will produce a bias on the calibrated measurement.

The most straightforward solution would be to change the feedhorn gain to underilluminate the reflector as a whole, reducing the change in spillover due to any potential offsets. But this is not possible due to the beam footprint requirements. A second option would be to move the feedhorn closer to the primary reflector without changing its gain. While this is an option for the 54 GHz in isolation, when considering the other three feedhorns in the cluster this stops being feasible. Due to the tight packing of the horns, moving the 54 GHz horn would result in it interfering with the beams of the other horns. Consequently, the remaining option is to change the size and design of the primary reflector. While drastically increasing the size of the reflector would reduce the aforementioned issues, it is not a viable option due to mass restrictions on the spaceborne instrument. However, the rim offset of the reflector is an open parameter to change which does not adversely affect performance or other instrument requirements. Fig. 9 shows changes in spillover for one feedhorn over a 270° scan arc. Each blue plot corresponds to a specific rim offset and the red plot is the "ideal" rimshift based on the smallest standard deviation in spillover across the scan arc.

However, Fig. 9 is only useful for minimising the overall fraction of the beam power not hitting the reflector. It does not take into account where this spillover occurs around the reflector. Its the multiplication of the fraction of beam power (F) with the integrated intensity (I) of the area illuminated by the spillover that produces the error in the measurement

IEEE Open Journal of Antennas and Propagation

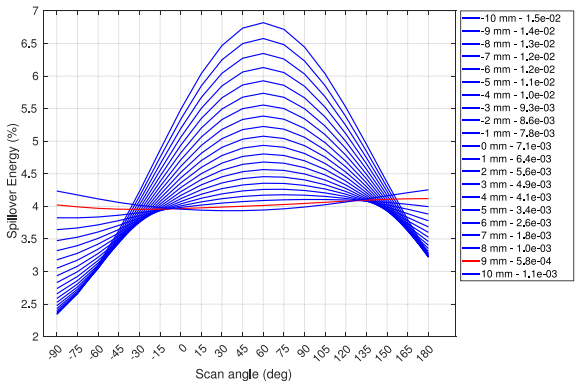

FIGURE 9. Spillover energy of 54 GHz horn hitting reflector across scan range as a function of rimsweep. Legend details spillover standard deviation for each rim position.

due to spillover. In equation 2, the subscript "mb" refers to the mainbeam and "i" to any arbitrary area in view of the spillover, e.g., structural elements of the satellite:

$$I_{total} = F_{mb} \cdot I_{mb} + \sum_{i=1} F_i \cdot I_i \tag{2}$$

Therefore it is possible for significant differences in spillover intensity to occur if the spillover views deep space ($\approx 3K$) for one scan angle and earth ($\approx 300K$) for another. Fig. 10 shows the total power farfield of the primary reflector for one frequency band and scan angle with specific regions of interest highlighted. As the GRASP output is saved in an Azimuth over Elevation grid where the z-axis is in line with (0,0) with poles at $\pm 90°$, each elements power value is normalised to the full sphere power $4pi$:

$$P_{normalised} = P_{element} \cdot cos(\phi) \cdot d\phi \cdot d\theta \tag{3}$$

where ϕ is the elevation angle which circles the pole and $d\phi, d\theta$ are the grid element sizes.

By integrating the energy fraction inside the regions of interest, the spillover can be further broken down by specific regions of interest. There is uncertainty in this approach, since the instrument's structure defining the outline of the spaceview are in the nearfield of the primary reflector. As a quality check to this approach, the sum of all the regions of interest was compared to the overall spillover of the primary reflector as reported by GRASP. The biggest difference across all tested bands and scan angles was: 0.2%. Detecting and mitigating significant spillover contributions from an earth view was the main objective, due to the earth's wide range of brightness temperatures in the atmosphere (54, 183 and 325 GHz) and also on ground (89 GHz) [11]. These variations could introduce a bias in the measurement which will depend on the instruments location above ground and the scan position of the primary reflector. This method was followed for the 54, 89 and 183 GHz band and for several scan angles (0, 66, 90, 180, 294). Since the overall spillover in the 325 GHz band is significantly lower (≈0.3%) than

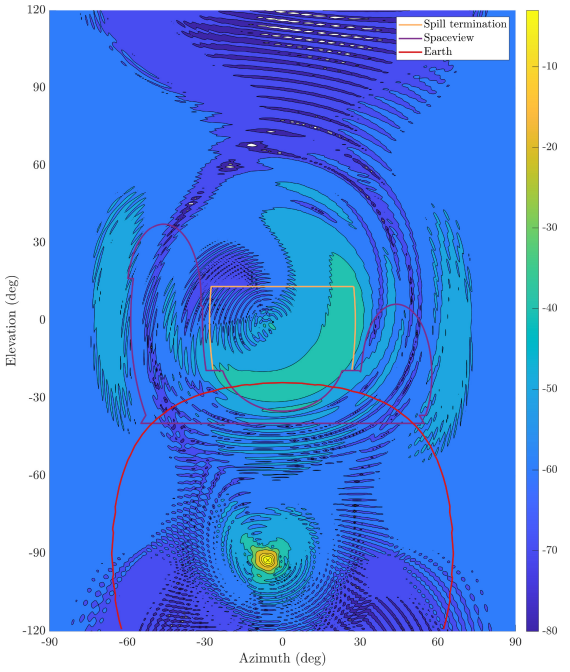

FIGURE 10. 54 GHz farfield from primary reflector highlighting different key features in the farfield. Origin corresponds to the flight direction of the satellite. Beam shown in nadir scan position.

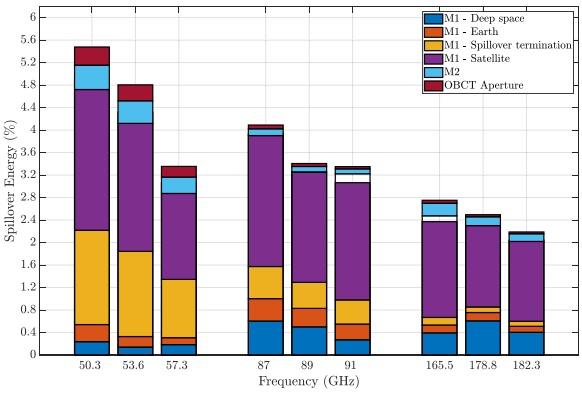

FIGURE 11. Spillover energy distribution for a scan angle of 180 degrees - OBCT facing. White gap between stacked bars due to mismatch of farfield integration and GRASP spillover.

for the other bands it was not considered to avoid tripling the simulation time per scan angle. The analysis showed a large spillover lobe which moved as a function of scan angle and was in view of earth. To mitigate this, the instrument design was modified to include an absorber plate behind the primary reflector which was shaped to capture this spillover lobe (marked in yellow in Fig. 10). When considering this addition, a plot summarising all spillover contributions for a given scan angle can be produced (Fig. 11).

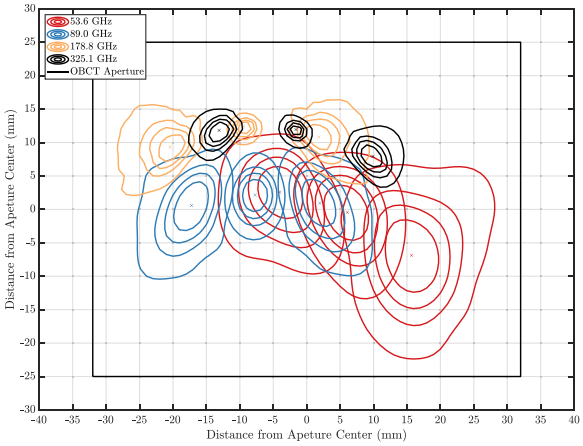

FIGURE 12. −3, −6, −10, −20 dB beam contours projected on OBCT aperture for 175, 180 and 185° scan angle (left to right).

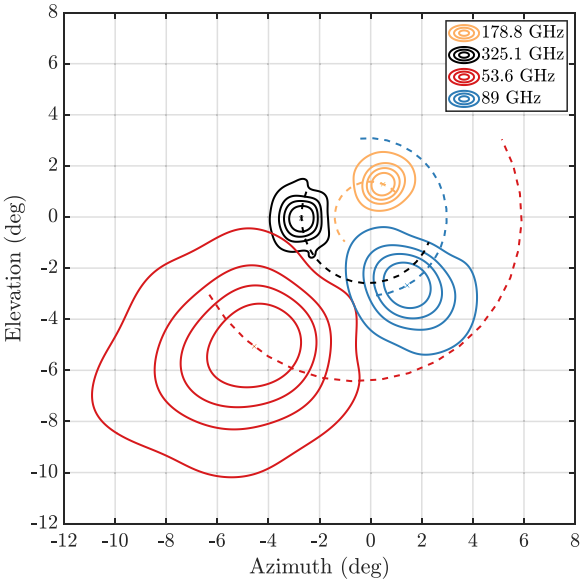

FIGURE 13. −3, −6, −10, −20 dB Contours of co-polar farfield AWS beams relative to the pointing vector of the primary reflector for a scan angle of 294°.

IV. CALIBRATION REFLECTOR

The calibration reflector is a static off-axis parabolic reflector used to focus the antenna beams on the aperture of the OBCT. As the calibration reflector had to be mounted between the two main structural elements of the instrument, it was restricted in size and position. Simultaneously, it needed to cover a 10° arc of the scan range of the primary reflector. By placing it close to the primary reflector and using a super elliptical rim shape, its overall size is reduced.

The second parameter governing its size is the focal distance which is driven by the distance of the OBCT aperture to the reflector. A smaller focal distance requires a greater curvature of the reflector, resulting in more mass. The distance of the OBCT aperture in turn is driven by the wedge opening angle which is fixed at 12° for performance [12]. A larger aperture requires a deeper wedge, which decreases the distance between the reflector and aperture. To find the smallest possible wedge aperture, beam contours are plotted on a planar grid located at the focal distance of the reflector (see Fig. 12). By iterating through this process, an aperture can then be chosen that captures each beam across a 10° scanning arc. The width of the arc, rather than its absolute position in the scan cycle (Fig. 3) is important. Although the 54 GHz band is close to the edge of the aperture at a scan angle of 185°, measurements can be taken prior to 175°, where it is better captured by the aperture. However, the 54 GHz band is still the size driver, as for all other optical components. To determine the aperture spillover for each scan position it was modelled as a surface in GRASP. Along with the calibration reflector spillover, it was added to the stacked bar chart of spillover sources to form a complete picture of spillover sources (Fig. 11). The figure shows a slightly higher spillover for the calibration reflector (M2) and the OBCT aperture for the 54 GHz compared to the other bands.

V. FARFIELD PERFORMANCE

Taking into account the optimisation detailed in the previous sections, Fig. 13 shows the co-polar farfield beams for each band, relative to the pointing vector of the primary reflector (plot origin). A beam sitting in the focal point of the primary reflector would have its beam center on the origin. However, due each beam's offset from the focal point, they are diverging in the farfield. The angular distance from the origin in the farfield is directly related to the offset of the horn in the feedcluster (Fig. 4). Thus, the 54GHz is the furthest away from the origin. However, this relative offset position is scan angle dependent. The dashed line plots the movement of the corresponding beam center as a function of scan angle from 270° to 90° encompassing the relevant scan angles for earth scanning and cold sky measurements. The beam movement is circular with a fixed radius around the pointing vector. This scan angle dependent movement needs to be accounted for when geo-locating the individual beams, but is fully characterised from the GRASP simulations. It is also evident in Fig. 12 over the 10° arc and accounted for in the OBCT aperture sizing.

The beam contours also exhibit a variation as a function of scan angle. This farfield variation increases with horn offset from the focal point of the reflector. When defining the mainbeam contour, one needs to consider both the fundamental ellipticity of the farfield beam and its variation. While determining the actual beam contour for each channel for each scan angle is possible, this is computationally too expensive for operational processing. Instead, an ellipse is fitted to the −3dB mid band contour of each horn and scaled up by a factor of 2.5. In post processing the length of the

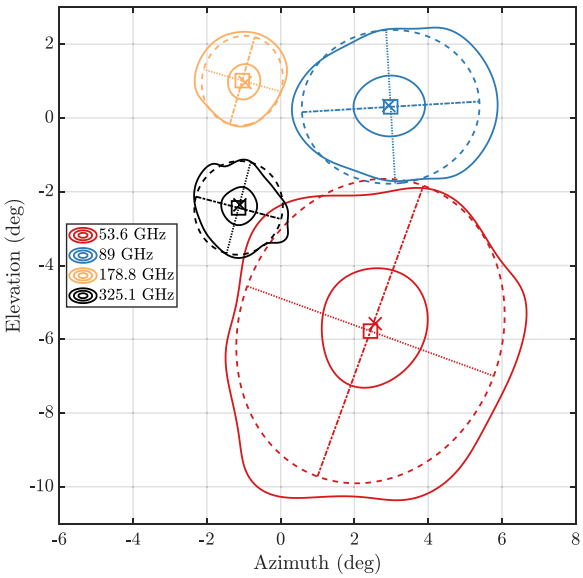

FIGURE 14. −3, −20 dB co-polar beam contours vs fitted mainbeam ellipse for a scan angle of 0° (nadir). Solid lines are simulated contours. Dashed lines are elliptical approximations. Dotted and dash-dotted lines are minor and major axes of the ellipses. Boxes mark the center of the ellipse and crosses the peak gain of the simulated contour.

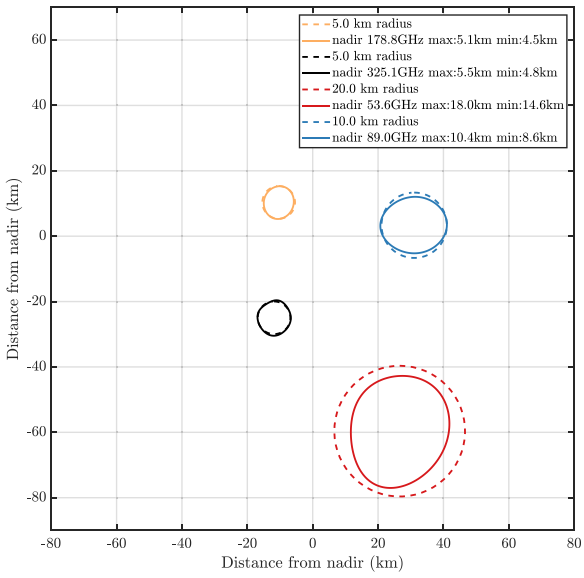

FIGURE 15. Full width half maximum footprints of actual AWS beams projected on ground vs maximum footprint requirements for nadir scan angle.

semi-major and semi-minor axes of the fitted ellipse along with their scan angle dependent orientation to the origin can then be used to define a mainbeam. Fig. 14 demonstrates this approach for a nadir (0°) scan angle. It also serves as an example of the scan dependent variations when comparing the contours to Fig. 13.

Two mainbeam efficiency definitions were considered during the design of the optics, both using the elliptical approximation of the mainbeam, but differing in the definition of the total power used:

$$mbe = \frac{P_{ellipse}}{P_{farfield}} \tag{4}$$

$$mbe = \frac{P_{ellipse}}{4 \cdot \pi} \tag{5}$$

Using (4), only the total power in the simulated farfield (30° x 30° grid) is considered and assumed to be 100%. Since AWS is calibrated via the main reflector, this definition is justified, if the spillover is constant for all scan angles and therefore does not affect calibration. However, (5) is required when spillover of the reflector and far sidelobes should be considered, which scales the mainbeam power by the total power radiated from the feedhorn.

While the ellipticity of the beams is a natural consequence of the instrument design, trade-off decisions were made to increase circularity for one band at the sacrifice of another. Evaluation of trade-offs is driven by the mission requirement on footprint size and allowable deviation. Fig. 15 shows the −3dB contours projected on ground in nadir in comparison to the maximum footprint size defined in the mission requirements. Each nominal maximum radius is given with a tolerance of ±25%. While the overall footprint size is driven by the horn and primary reflector, the ellipticity induced by the optics on the footprint may not infringe on these limits. Table 1 shows a summary of the farfield performance for all simulated frequencies.

VI. SUMMARY

The AWS mission is a prototype for the EPS-Sterna constellation consisting of a constellation of six satellites on two sun-synchronous orbital planes, which will improve global NWP in combination with the existing Met-OP and NOAA programmes. Furthermore it will increase the frequency of measurements in the high latitudes and achieve operational nowcasting capability in the arctic region. Each satellite will carry a single identical payload; A four band (54, 89, 183, 325 GHz) radiometer built by AAC Omnisys. Due to the large number of radiometers that are required for this mission they need to be smaller and less complex than previous operational radiometers (MWS, ATMS), but achieve similar performance. The AWS radiometer achieves this by using a feedcluster in a splitblock directly illuminating the primary (scanning) reflector, foregoing the need for other optical elements for beam co-alignment. The feedcluster contains four smooth-walled spline horns. As no horn is in focus of the primary reflector, this design decision results in asymmetries and scan angle dependent performance variations. Using the GRASP and CHAMP software from TICRA, the quasi-optics of the radiometer were simulated and optimised. Performance trade-offs were made during optimisation of the feedcluster configuration and positioning, maximising beam circularity and gain. The primary and calibration reflectors

TABLE 1. Performance summary in nadir for all simulated frequencies. Beam centers stated relative to pointing of primary reflector. Footprints stated as minor and major radius of ellipse. Mainbeam efficiencies stated for equation (4) without brackets and equation (5) in brackets.

Frequency	Beam center (nadir)	FWHM footprint	Mainbeam efficiency
50.3 GHz	x: 2.55°	15.2 km	96.4% (91.9%)
	y: -5.67°	18.5 km	
53.6 GHz	x: 2.54°	14.6 km	96.6% (92.7%)
	y: -5.68°	18.0 km	
57.3 GHz	x: 2.49°	14.2 km	96.9% (94.2%)
	y: -5.71°	17.4 km	
87.0 GHz	x: 2.96°	9.1 km	96.7% (93.0%)
	y: 0.32°	10.4 km	
89.0 GHz	x: 2.96°	8.6 km	96.8% (93.7%)
	y: 0.32°	10.4 km	
91.0 GHz	x: 2.95°	8.9 km	96.8% (93.8%)
	y: 0.32°	10.0 km	
165.5 GHz	x: -0.99°	4.7 km	96.4% (94.0%)
	y: 0.99°	5.5 km	
178.8 GHz	x: -0.99°	4.5 km	96.8% (94.6%)
	y: 0.99°	5.1 km	
182.3 GHz	x: -0.99°	4.5 km	96.6% (94.7%)
	y: 0.99°	5.1 km	
321.8 GHz	x: -1.13°	4.9 km	98.0% (97.7%)
	y: -2.38°	5.5 km	
325.1 GHz	x: -1.13°	4.8 km	98.0% (97.7%)
	y: -2.38°	5.5 km	
328.5 GHz	x: -1.13°	4.8 km	97.9% (97.6%)
	y: -2.38°	5.6 km	

were optimised to minimise overall spillover and its scan angle dependency. Farfield beam divergence, beam shape, beam pointing and their scan angle dependency was also simulated. Furthermore, a simple method of mainbeam definition for the elliptical beamshapes was detailed.

REFERENCES

[1] N. Bormann, H. Lawrence, and J. Farnan. "Global observing system experiments in the ECMWF assimilation system." Sep. 2019. [Online]. Available: https://www.ecmwf.int/node/18859

[2] K. Lean, N. Bormann, S. Healy, and S. English. "Final report: Study to assess earth observation with small satellites and their prospects for future global numerical weather prediction." Feb. 2022. [Online]. Available: https://status.ecmwf.int/en/elibrary/81324-final-report-study-assess-earth-observation-small-satellites-and-their-prospects

[3] Y. Wang et al., *Guidelines for Nowcasting Techniques*, World Meteorl. Org., Geneva, Switzerland, Nov. 2017.

[4] V. Kangas et al., "Microwave sounder instrument for MetOp second generation," in *Proc. 13th Specialist Meeting Microw. Radiometry Remote Sens. Environ. (MicroRad)*, 2014, pp. 232–235. [Online]. Available: https://ieeexplore.ieee.org/document/6878947

[5] R. Wylde. "MWS QON delivered to airbus U.K." 2018. [Online]. Available: http://terahertz.co.uk/news/mws-qon-delivered-to-airbus-uk

[6] C. Muth, P. Lee, J. Shiue, and W. A. Webb, "Advanced technology microwave sounder on NPOESS and NPP," in *Proc. IEEE Int. Geosci. Remote Sens. Symp. (IGARSS)*, vol. 4, 2004, pp. 2454–2458.

[7] W. J. Blackwell et al., "An overview of the TROPICS NASA earth venture mission," *Quart. J. Roy. Meteorol. Soc.*, vol. 144, no. S1, pp. 16–26, 2018. [Online]. Available: https://rmets.onlinelibrary.wiley.com/doi/abs/10.1002/qj.3290

[8] B. Lagaune, S. Berge, and A. Emrich, "Arctic weather satellite, a microsatellite constellation for improved weather forecasting in arctic and globally," in *Proc. 35th Annu. Small Satellite Conf.*, 2021, p. 2. [Online]. Available: https://digitalcommons.usu.edu/cgi/viewcontent.cgi?article=5087&context=smallsat

[9] A. Hammar et al., "THz smooth-walled spline horn antennas: Design, manufacturing and measurements," in *Proc. IEEE Int. Symp. Antennas Propag. (APSURSI)*, 2016, pp. 1341–1342.

[10] E. P. Cox, "A method of assigning numerical and percentage values to the degree of roundness of sand grains," *J. Paleontol.*, vol. 1, no. 3, pp. 179–183, 1927. [Online]. Available: http://www.jstor.org/stable/1298056

[11] F. Ulaby et al., *Microwave Radar and Radiometric Remote Sensing*. Ann Arbor, MI, USA: Univ. Michigan Press, Jan. 2014, ch. 8, pp. 317–328.

[12] K. Jacob, A. Schröder, and A. Murk, "Design, manufacturing, and characterization of conical blackbody targets with optimized profile," *IEEE Trans. THz Sci. Technol.*, vol. 8, no. 1, pp. 76–84, Jan. 2018.

ROLAND ALBERS received the B.Eng. degree in aerospace engineering from Brunel University, London, in 2015, and the M.Sc. degree in astronautics and space engineering from Cranfield University, Milton Keynes, in 2016. After working in the space industry on quasi-optical components, he is currently pursuing the Ph.D. degree in applied physics with the University of Bern, Switzerland. His research interests are spaceborne radiometry, hardware design, and calibration.

ANDERS EMRICH received the M.Sc. and Ph.D. degrees in electrical engineering from the Chalmers University of Technology, Göteborg, Sweden, in 1985 and 1992, respectively. In 1992, together with S. Andersson, he founded Omnisys Instruments AB, Västra Frölunda, Sweden, and was responsible for several subsystems for the ODIN radiometer payload and many development contracts toward ESA/ESTEC. He has been engaged in research collaborations with the Chalmers University of Technology and other research institutes and universities for more than 30 years. He has a Co-Supervisor for three Ph.D. students at Chalmers. He has been responsible for the design, development, and production of the 183-GHz Water Vapor Radiometer (58 units) for ALMA, the GAS radio interferometer demonstrator (ESA contract), and the STEAMR instrument. He proposed the Artic Weather Satellite project to end users, including Eumetsat, and the Swedish National Space Agency proposed to the development project the ESA council 2019. He is currently leading the design and development of the instrument and several subsystems.

AXEL MURK received the M.Sc. degree in physics from the Technical University of Munich, Munich, Germany, in 1995, and the Ph.D. degree in physics from the University of Bern, Bern, Switzerland, in 1999. Since then, he has been involved in the development and characterization of millimeter- and submillimeter-wave instrumentation for different ground-based and space-borne projects. Since 2018, he has been leading the IAP Microwave Physics Division, University of Bern. His research interests include digital real-time spectrometers and the radiometric calibration of remote sensing instruments.

IEEE TRANSACTIONS ON GEOSCIENCE AND REMOTE SENSING, VOL. 62, 2024 5301908

Development of the Onboard Calibration Target for the Arctic Weather Satellite

Roland Albers, Tobias Plüss, *Member, IEEE*, Lars Eggimann, and Axel Murk

***Abstract*— We present the design and characterization of the onboard calibration target (OBCT) for the arctic weather Satellite radiometer. The arctic weather satellite (AWS) is a single-instrument mission consisting of a cross-track scanning microwave radiometer. The radiometer optics consists of a feed cluster with four horns (54, 89, 183, and 325 GHz) directly illuminating a primary scanning mirror. The OBCT is a wedge-shaped cavity with an absorber consisting of an epoxy-based mixture, developed and produced by the University of Bern. The coupling into the target via a secondary mirror is simulated using Ticra Tools and the effects of the divergent beams are investigated. We present the development of the target and laboratory measurements of the flight model showing a return loss of 55 dB or better for all bands in TM mode. A worst case thermal simulation is presented, highlighting possible temperature gradients in the target.**

***Index Terms*— Absorber, blackbody, mm-wave, radiometer, remote sensing.**

I. Introduction

OBSERVATIONS from space-based microwave radiometers are a crucial component of global weather forecasting. Several national or international meteorological services operate their own satellites which include microwave radiometers, typically with decade-long service lives. To maintain accurate measurements, the microwave sounders need to be calibrated continuously, as gain variations in the receiver can occur on a second timescale. This is typically achieved by two-point calibration, using "cold" deep space measurements in combination with a "warm" onboard calibration target (OBCT), where the OBCT is made up of a periodic array of pyramidal elements. Such a target is used by all major meteorological operators such as metop second-generation (Metop-SG) [1], joint polar satellite system (JPSS) [2], and Fengyan-3 (FY-3) [3]. The pyramidal elements exploit multiple reflections between them to increase the return loss of the OBCT. They also offer consistent performance for both linear polarizations, which enables using polarizing grids to co-align beams in the quasi-optics. Another polarization agnostic option is a conical OBCT which is, for example, used in the submillimeter-wave instrument (SWI) on the Jupiter icy moons explorer (JUICE) [4], because the two bands' ($\sim$ 600 and $\sim$ 1100 GHz) polarizations are orthogonal. A cone requires a larger volume for equivalent aperture than an array of pyramids, but since the SWI bands measure at much higher frequencies (shorter wavelength) than for Met-OP, JPSS, and FY-3, it could be accommodated. In general, the main drawback of including an OBCT is the required additional mass and volume, but since these microwave sounders are part of a suite of instruments hosted on a large satellite platform this is permissible. On some CubeSat missions such as the 3U TROPICS constellation [5] where including an OBCT is not possible, noise diodes are used to generate a calibration source electrically, which is injected at the input of the receiver chain. However, one disadvantage of this method versus using an OBCT is that it cannot remove errors introduced by the quasi-optics such as reflector spillover. Other CubeSat missions such as TEMPEST-D [6] do include an OBCT for continuous calibration by scaling up to 6U. However, due to the limited volume, the OBCT size and positioning are restricted. This affects the number of usable samples and possible thermal gradients across the OBCT. The size of the arctic weather satellite (AWS) mission is in between these programs as a single payload mission with a cross-track scanning microwave radiometer, built by AAC Omnisys on a SmallSat platform from OHB Sweden. It is a prototype for a constellation of operational microwave sounders called EUMETSAT Polar System (EPS) Sterna. The constellation will consist of six satellites, improving global numerical weather prediction and providing frequent revisit times [7]. It uses four bands (54, 89, 183, and 325 GHz) with a total of 19 channels to retrieve temperature and water vapor profiles, as well as cloud liquid water content and precipitation. Since the AWS is designed with a constellation in mind, it is constrained in volume, cost, and complexity to keep building up to 20 copies affordable. Regarding quasi-optics, this is achieved by forgoing beam co-alignment and, consequently, any additional components typically needed, such as mirrors, dichroics, and polarizing grids. A split-block feed cluster with four horns directly illuminates the continuously rotating primary mirror. Since all the bands share one polarization, the OBCT is wedge-shaped. A wedge is simpler to manufacture, but offers optimal performance for only one polarization. To reduce the OBCT aperture size and hence its volume, a second mirror is used to refocus the beams. This article presents the development, simulation, and measurements of the OBCT.

II. Optics

A distinguishing feature of the AWS optics is the split-block feed cluster which illuminates the primary scanning mirror without any beam co-alignment. The scanning mirror is

Manuscript received 1 March 2024; revised 24 June 2024 and 24 July 2024; accepted 27 July 2024. Date of publication 1 August 2024; date of current version 15 August 2024. *(Corresponding author: Roland Albers.)*

The authors are with the Institute of Applied Physics, Bern University, 3012 Bern, Switzerland (e-mail: roland.albers@unibe.ch).

Digital Object Identifier 10.1109/TGRS.2024.3436517

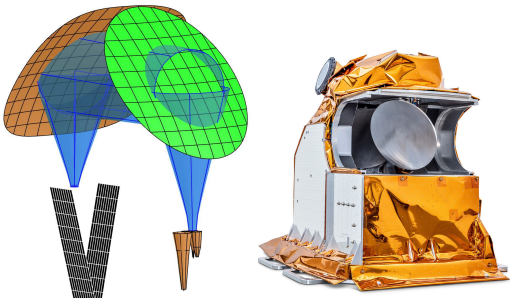

Fig. 1. Picture of relevant elements for OBCT simulation in Ticra Tools (left). Primary mirror (green) shown in zenith scan position, focusing mirror in orange, OBCT absorber surface in black. 20-dB Gaussian beam tube of 183-GHz feed for visualization only. Picture of AWS OBCT PFM (right), courtesy of AAC Omnisys. Approximate instrument size: 390 × 660 × 540 mm.

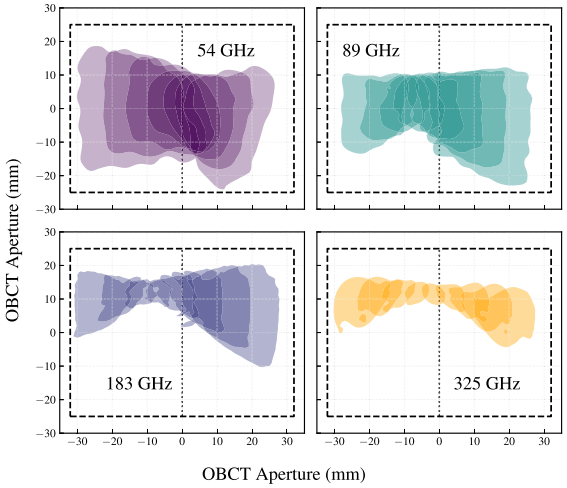

Fig. 2. Coverage of each beam as they track over the OBCT aperture (dashed line), shown as superposition of 30-dB contours for individual scan angles.

an offset parabolic mirror, rotating continuously at 0.84 Hz. Although the overall optics are simpler and more compact in this configuration compared with quasi-optical networks which include elements for co-alignment, the effect of each feed's lateral offset from the focal axis of the reflector in the feed cluster plane needs to be considered. Most importantly, the beams diverge from the outgoing focal axis of the reflector and rotate around it as a function of scan angle. A detailed assessment with regard to spillover, beam far-field performance, and optimization can be found in [8]. The primary scan mirror couples into the OBCT through a fixed parabolic mirror positioned in zenith. Both the mirrors consist of machined aluminum. The focusing mirror fills a minimum of 10° in the rotation of the primary mirror (Fig. 1). However, the exact position of this arc in the rotation of the primary mirror varies for each feed horn, due to the aforementioned beam divergence. Furthermore, the beams do not track across the OBCT aperture in a straight line, but in a curve due to their rotation around the reflector focal axis. Fig. 2 shows the track of each beam across the aperture of the OBCT as a superposition of 30-dB contours. The apex of the wedge is marked by the vertical dotted line dividing the aperture outline. It is also apparent that due to the beam divergence, each beam is illuminating different parts of the OBCT aperture. Furthermore, the sizes of the contours differ between channels, due to the different directivities of each horn. For a given scan angle, the 325-GHz band will illuminate a much smaller section of the wedge than the 52-GHz band. This should be considered if there are temperature gradients in the OBCT during operational use. Fig. 3 shows a comparison of the coupling into the OBCT aperture for each beam (dashed line) against a test measurement of the protoflight model (PFM). During normal operation, the scan range across the OBCT is only 10.6° over 15 samples, avoiding recording unnecessary data. The dataset shown here has a larger range, which is useful to compare the simulated coupling into the OBCT aperture with the as-built configuration. The measurement was taken in atmosphere while a liquid nitrogen (LN2) target was positioned in the nadir view of the instrument, making the OBCT the hottest object in view of the instrument. OBCT temperature data were also recorded during this test and used to scale the recorded counts. The measured counts have been calibrated by taking the typical Y-factor from other measurements and subtracting a system noise temperature for each channel so that the highest count value is equivalent to the peak temperature measured for the OBCT (302.4 K). While this is not a proper calibration, it converts the raw count data of each channel into a common and comparable scale. The gray area denotes the scan angle range where the coupling is equal or larger than 99%, which is larger than the required 10° for all beams. The 99% coupling factor does not consider the spillover occurring at the primary mirror. It refers only to the possible spillover at the calibration mirror and OBCT aperture. All the channels show temperature decreases when coupling decreases, since the fact that the AWS and its restricted viewport are metal causes any reflections to predominately view the LN2 target. The slope of the coupling decrease is a function of beam size and increases in steepness with frequency.

III. Onboard Calibration Target

The AWS OBCT consists of a wedge-shaped cavity with a rectangular aperture (Fig. 4). Aluminum backing plates hold the in-house developed absorber based on epoxy resin. Each backing plate is equipped with four resistance temperature detectors (RTDs) cast into the weight saving pockets on the back of the plates. A total of eight RTDs form two redundant sets of temperature sensors across both the wedge sides. Two thin aluminum plates with thermally absorbing paint close the wedge at either side. They are electrically reflective and do not contribute to the absorption of the OBCT. Two thick aluminum plates provide structural support and form the interface to the instrument base plate. They are gold-plated to minimize radiative thermal coupling with surrounding components, which could induce a temperature gradient across the OBCT. The OBCT is entirely passive and does not include any capability to control its temperature. The OBCT fits inside a footprint of 170 × 110 mm with a height of 163 mm and weighs just

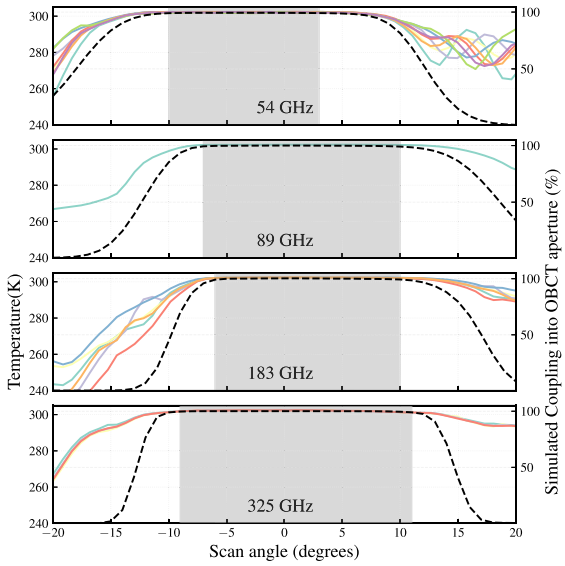

Fig. 3. Simulated coupling into the OBCT aperture (dashed lines) against measured brightness temperature on the PFM instrument (colored lines). The gray area denotes coupling $\geq$ 99%. Spillover at the primary mirror is not considered. Scan angles are relative to zenith position.

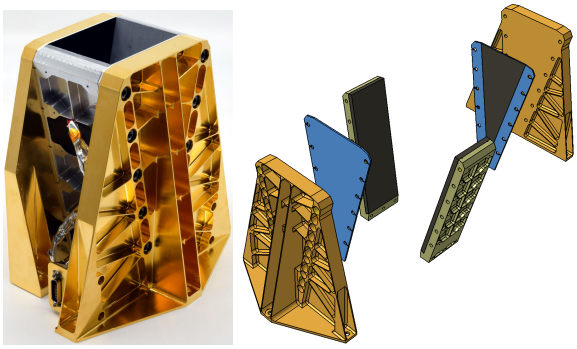

Fig. 4. Picture of assembled AWS OBCT (left). Exploded view on the right. The OBCT fits inside a 170 $\times$ 110 $\times$ 163 mm volume and weighs slightly less than 1 kg.

under 1 kg. The return loss requirement for the OBCT is 50 dB or better to minimize coherent backscatter inducing standing waves.

A. Absorber

As part of the Metop-SG program, other epoxy-based absorber mixtures have been developed at the University of Bern [9]. The Metop-SG absorber consisted of Stycast 2850FT mixed with carbonyl iron powder (CIP). Using a magnetic material was necessary to achieve the required absorption at the low end of the Metop-SG Microwave Sounder bands (23.8 and 31.4 GHz). The downside of the previous mixture is the high refractive index of Stycast 2850FT ($\epsilon_r > 5$) which increases with CIP loading. Low reflectivity is desirable as it enables higher absorption for the same number of reflections. Since the lowest AWS band starts at 50 GHz, it is possible

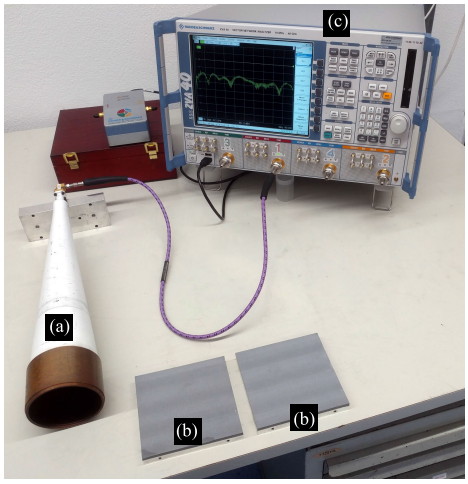

Fig. 5. Return loss measurement of absorber breadboard. (a) Ka-band corrugated horn antenna. (b) Material samples to be tested. (c) Rohde & Schwarz ZVA40 network analyzer.

to use other absorbing materials which are assumed to be nonmagnetic. Another downside of Stycast 2850FT in our experience is that a high concentration of absorber material mixed into the epoxy leads to difficulty in manufacturing due to the high viscosity. Finally, there is an issue with poor thermal conductivity of the absorber mixture, increasing potential temperature inhomogeneities between the temperature sensor in the aluminum backing plate and the epoxy, where absorption occurs. Consequently, another absorber mixture was developed with the aim of addressing the aforementioned issues. It consists of three parts, Stycast 1266 ($\epsilon_r = 3$) as the epoxy base, carbon black powder as the absorbing additive, and boron nitride as thermal conductivity influencing additive. Boron nitride is a common insulating additive for epoxies and often used to produce thermal paste among other applications.

Several iterations of absorber mixture were cast as breadboards. Using a vector network analyzer (VNA), the return loss of each sample was measured from 27 to 40 GHz, which is the upper limit of the VNA (Fig. 5) without extensions. The measurements were taken with the absorber layer contacted against the aperture of the horn and calibrated with a second measurement of the metal backing face, serving as a perfect reflector.

Fig. 6 shows return loss measurements of two breadboards with identical absorber mixtures, demonstrating good repeatability of the manufacturing process. The ripple on the measurements is caused by standing waves inside the horn antenna. Using these measurements, the relative permittivity of the absorber material can be determined using a nonlinear fitting procedure as follows.

The return loss of the samples is described by

$$S_{11} = \frac{\Gamma - z^2}{1 - \Gamma z^2} \tag{1}$$

where

$$\Gamma = \frac{\sqrt{\frac{1}{\hat{\epsilon}_r}} - 1}{\sqrt{\frac{1}{\hat{\epsilon}_r}} + 1} \tag{2}$$

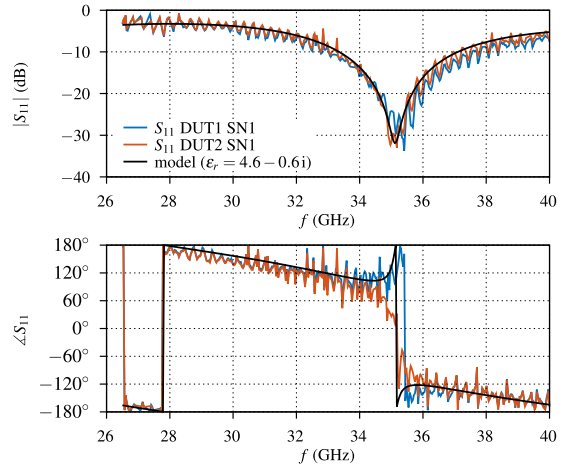

Fig. 6. S_{11} measurements of two breadboards with identical absorber.

is the reflection coefficient at the surface of the absorber layer, and

$$z = \exp\left(-\mathrm{i}\frac{\omega}{c}\sqrt{\hat{\epsilon}_r}\, d\right) \tag{3}$$

is the transmission coefficient inside the absorber and d is the material thickness [10], [11]. Finally, using

$$\hat{\epsilon}_r = \arg\min |S_{11,\text{measured}}(f) - S_{11,\text{calculated}}(f, \hat{\epsilon}_r)| \tag{4}$$

yields the relative permittivity used for the calculated return loss plot seen in Fig. 6. We assume the permittivity to be constant over the frequency range of our measurement to the top end of the AWS range.

With this assumption, using an in-house 2-D plane-wave tool, a simulation of the expected return loss for a wedge with a 12° opening angle and various thicknesses can be generated (Fig. 7). The simulation takes both transverse electric (TE) and transverse magnetic (TM) incidence into account. TE means that the electric field is polarized parallel to the apex of the wedge, whereas TM means that the electric field is polarized perpendicular to the apex. At lower frequencies, the return loss oscillates, as it depends on the constructive or destructive interference of the reflections at the air/absorber and absorber/metal interfaces. As the thickness increases, absorption inside the material dominates and the ripple disappears. The vertical solid white lines mark the centers of each AWS frequency band. The horizontal solid white lines indicate potential absorber thicknesses which provide return loss below 50 dB in the relevant bands. For the final wedge, an absorber thickness of 3.5 mm was chosen as a compromise between maximizing performance and minimizing mass.

B. Performance

The OBCT return loss (S_{11}) was measured in the lower three AWS frequency bands (54, 89, and 183 GHz). Due to lack of available hardware, the 325-GHz band measurement was replaced by a measurement at 400 GHz. Since the predicted performance of the OBCT is relatively constant above

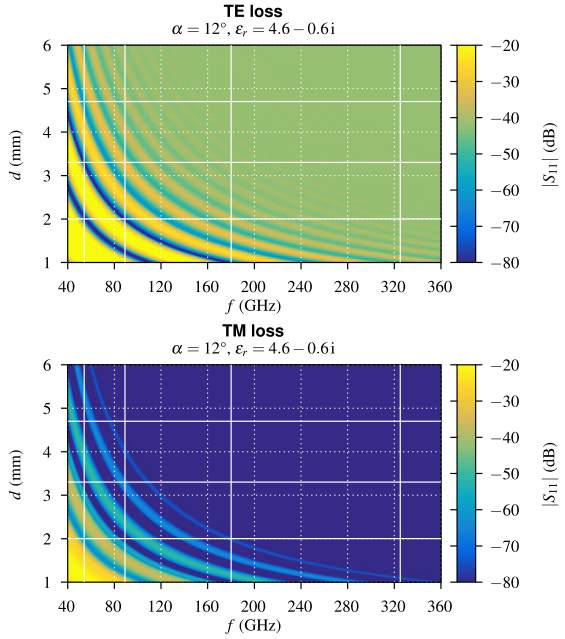

Fig. 7. Simulated return loss against thickness and frequency of the final absorber mixture for both the polarizations.

200 GHz, there should be no significant difference between these two bands. The measurements were performed prior to integration, without using the feed cluster of the instrument. Instead, each band was measured individually using corrugated feed horns aiming at the center of the OBCT aperture. Consequently, the beam size and positioning within the aperture were not identical to the final use case. For 54 and 89 GHz, a directional coupler was used in combination with the ABmm VNA and appropriate multipliers. Using a translation stage, the OBCT was moved along the symmetry axis of the feed, changing the phase of the backscatter. An identical method was performed using a metal plate instead of the OBCT which was also moved on the translation stage to perform a sliding load calibration. The test setup for 89 GHz is shown in Fig. 8. For 183 and 400 GHz, the directional coupler was replaced by a quasi-optical setup, shown in Fig. 9. More details of the measurement methodology, including the quasi-optical setup for 183 GHz and above, can be found in [9]. As simulations predicted the 54-GHz band to be the most critical, the OBCT was measured in TE, TM, and 45° polarizations (Fig. 10). The OBCT performance is below the targeted return loss of 50 dB for TM and 45° and slightly exceeding it for TE at the high end of the band. A summary of measurement results across all the bands is shown in Fig. 11. As predicted in the simulations (Fig. 7), the TM return loss is lower than for TE. Furthermore, despite assuming constant permittivity, the return loss minimum at the 54-GHz band was measured as predicted.

C. Thermal Error Sources

Aside from the optical aspects, the uncertainty of the OBCT temperature and its homogeneity drives the accuracy of AWS

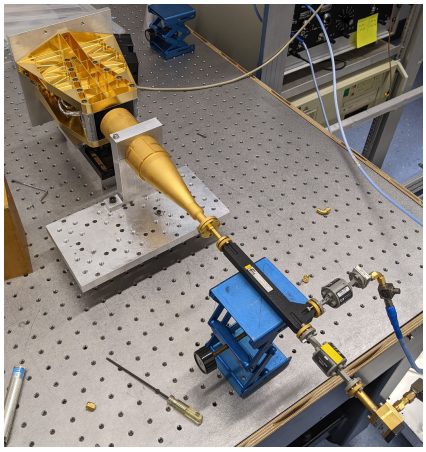

Fig. 8. AWS OBCT return loss measurement setup for 89 GHz.

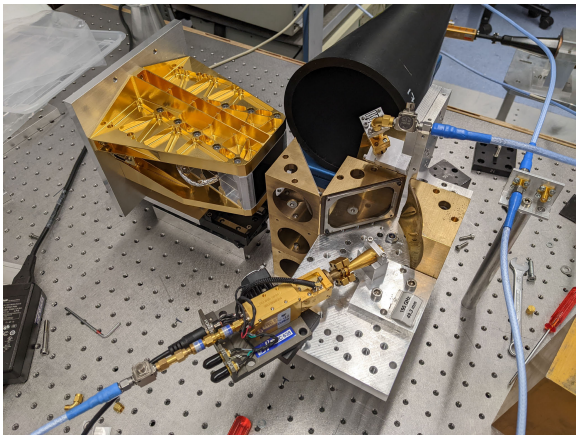

Fig. 9. AWS OBCT return loss measurement setup for 183 and 400 GHz using quasi-optical directional coupler.

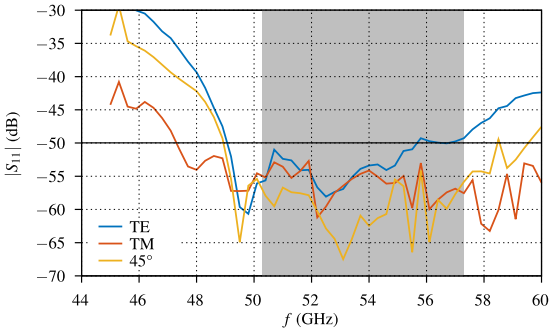

Fig. 10. Measured return loss of AWS OBCT when rotated.

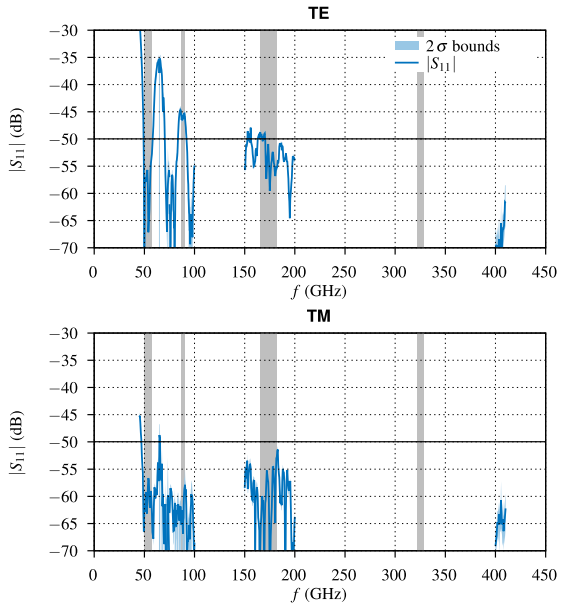

Fig. 11. Measured return loss of AWS OBCT for horizontal and vertical polarizations.

calibration. There are three factors to consider for the OBCT temperature. First, the accuracy of the RTDs themselves causes an error on calibration. For the AWS OBCT, the RTDs were procured according to tolerance class F of the international standard IEC60751. The standard states a tolerance of $\pm 0.15 + 0.002|t|$ where t is the temperature modulus in degree Celsius. The expected operating temperature of the radiometer is approximately 20 °C. Second, as can be seen in Fig. 2, the beams scan across the OBCT aperture, which means they are absorbed—at least for the primary incidence—at different sections of the wedge, depending on the frequency and scan angle. The different wedge sections can vary in temperature both horizontally and vertically. Due to the tall structure of the OBCT and being thermally clamped to the base plate and thermally "floating" at the top, vertical temperature gradients will dominate over horizontal gradients. To resolve these potential gradients, RTDs are located at two heights along the back of the wedge (Fig. 12). Furthermore, the RTDs are split into a nominal (set A) and redundant (set B) set of four. During normal operation, only one set will be read to retrieve OBCT temperature. The distribution shown in Fig. 12 was chosen to enable either set to resolve potential vertical and horizontal gradients independently. However, since the RTDs are located at the back of the aluminum plates and not in the absorber, as this would negatively affect absorption, there will be a difference between the temperature of the absorber and the RTD reading. This gradient is mitigated by maximizing the thermal conduction of the absorber (see Section III-A) and minimizing the thickness of the aluminum and absorber.

A further complication is that the depth at which the radiation is absorbed is frequency-dependent. Consequently, each AWS beam is biased differently by the temperature gradient through the absorber thickness. As a worst case scenario, the minimum absorption path is twice the absorber thickness or 7 mm, which is equivalent to perpendicular incidence. However, for the first reflection the incidence is very shallow. When the primary mirror is in the zenith position and coupling into the center of the OBCT aperture, the angle of incidence is half the wedge apex angle or 12° for the mirror boresight. This

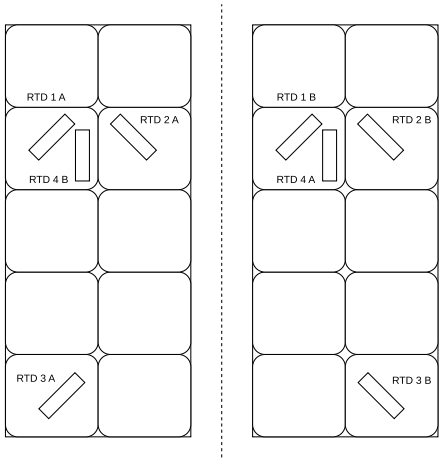

Fig. 12. Schematic of both AWS backing plates and their RTD distribution.

is the same incidence as during the return loss measurements shown in Figs. 8 and 9. However, since the absorber is a lossy material, the incident beams will be refracted [12]. The angle of transmission is

$$\chi_2 = \tan^{-1}\left[\frac{\sqrt{2}k_1 \sin\theta_1}{\sqrt{\sqrt{p^2+q^2}+q}}\right] \tag{5}$$

where k_1 is the wavenumber in free space, and θ_1 the angle of incidence. The abbreviations p and q are

$$p = 2\alpha_2\beta_2, \quad q = \beta_2^2 - \alpha_2^2 - k_1^2 \sin^2\theta_1 \tag{6}$$

where α_2 and β_2 are the absorber's attenuation constant and phase constant, respectively, as follows:

$$\alpha = k_1\sqrt{\frac{\epsilon_r'}{2}\left(\sqrt{1+\frac{\epsilon_r''^2}{\epsilon_r'}}-1\right)} \tag{7}$$

and

$$\beta = k_1\sqrt{\frac{\epsilon_r'}{2}\left(\sqrt{1+\frac{\epsilon_r''^2}{\epsilon_r'}}+1\right)}. \tag{8}$$

Assuming a constant permittivity ϵ for all frequency bands, the angle of transmission is 24.5° for all bands. This increases the worst case absorption path by a factor of $(1/\cos(24.5°)) = 1.09$. The beam divergence of the bands due to the feed offset is not considered, which puts them 1°–2° off the mirror boresight. At each reflection, a fraction of the beam intensity will be transmitted into the absorber. The skin depth δ_s defines the depth at which the electric field of a wave of a given frequency has decayed by a factor of $1/e$ and is given by [12]

$$\delta_s = \frac{1}{\alpha}. \tag{9}$$

This is equivalent to a power fraction of $1/e^2 \approx 14\%$, which is not large enough to make a judgment on whether and where in the absorber material the transmitted beam is sufficiently attenuated. $2.5\,\delta_s \approx 1\%$ is calculated to represent a more intuitive value

Frequency (GHz)	54	89	183	325
$2.5\,\delta_s$ (mm)	15.8	9.6	4.7	2.6

(10)

In the worst case scenario of perpendicular incidence (7-mm absorption path), only the 183-and 325-GHz bands meet the defined absorption threshold of 1%. At first reflection conditions with an absorption path of $1.09 \times 7\,\text{mm} = 7.63\,\text{mm}$, the other bands are still not sufficiently attenuated. Nevertheless, as absorption occurs deep in the material and after reflecting off the metal backing plate, a vertical temperature gradient in the absorber will affect all the four bands. Apart from the 183-and 325-GHz band, the beams will not attenuate sufficiently at first incidence and the energy transmitted into the absorber will propagate further into the wedge.

IV. OBCT Thermal Simulation

To gain an appreciation of the possible thermal gradients of OBCT during operation, thermal simulations were performed using the ANSYS thermal analysis software. A CAD model of the OBCT was imported and thermally clamped to a simplified base plate at a temperature of 35 °C. The environment was set at −10 °C, which is equivalent to a homogeneous minimum operating temperature of the instrument structure. This particular combination of temperatures represents the worst case condition during operation of the instrument. As the OBCT sits deep within the structure which is covered in multilayer insulation (MLI), it is assumed to be unaffected by thermal radiation external to the instrument, e.g., from the Earth or sun. The crescent-shaped shield seen on the right of the instrument in Fig. 4 offers further protection from direct sun intrusion. Emissivity measurements of the absorber material at infrared wavelengths are not available, and therefore the assumed value is 1 as a worst case value. The aluminum and gold plating of the OBCT have emissivities of 0.1 and 0.025, respectively [13].

Fig. 13 shows the extracted temperature profile along the vertical axis of the OBCT (upward direction in Fig. 4) for three different locations along the absorber backing plates. The x-axis shows the vertical distance from the bottom wedge up toward the wedge opening. The solid blue line denotes the temperature profile along the surface of the absorber. The dashed line is for the same horizontal location at the interface between the absorber and the aluminum backing plate holding it. The dotted line corresponds to the temperature along the backside of the aluminum backing plate, where the temperature sensors are located. The temperature profile is not an average of the whole plate but taken at the center line of the pockets on the back of the plate. Each line starts at a different z position, according to the vertical height at which the feature they represent begins. The crosses denote the positions where the RTDs are located.

Since the surroundings are at a lower temperature than the baseplate, the temperature decreases with distance from the base plate, as expected. The larger drop toward the wedge aperture in absorber temperature can be explained by the exponentially increasing viewing angle to the cold surrounding

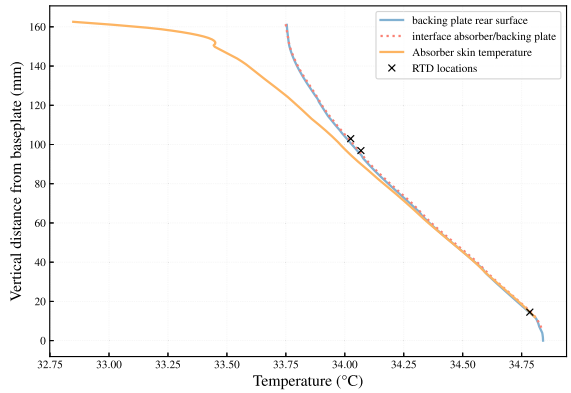

Fig. 13. Simulated temperature of OBCT absorber and its backing plate for minimum operating temperature.

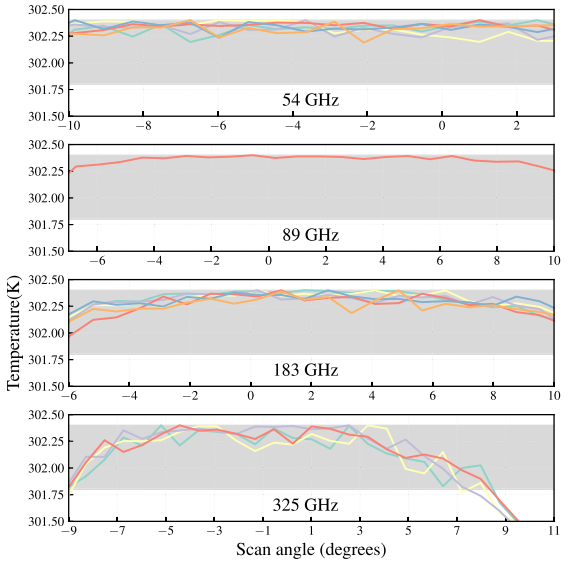

Fig. 14. Measured brightness temperatures for each band across OBCT aperture. Gray area denotes temperature range measured by OBCT sensors.

and the high absorber emissivity. The wedge temperature differs by 0.7 K between the lower and upper RTD locations, which is significant when considering how the beams track across the aperture (Fig. 2). Depending on the scan angles, the temperature of the OBCT absorber seen by each band can vary by this amount and should be compensated for. Furthermore, the difference between the simulated RTD temperature and the absorber surface temperature introduces another error during calibration. For any value of z, the vertical offset between the dotted and solid line expresses the maximum temperature difference at that height. The temperature offset between the RTD location and the metal/absorber interface is an error independent of frequency because it occurs through the aluminum. Since the thickness of the metal is minimal at RTD location, the offset is low for all RTD positions at 0.01 K. The offset from the interface to the absorber skin increases along the height of the OBCT, starting with a negligible difference (< 0.01 K) at the lower RTD location, close to the wedge apex. For higher RTD locations, the gradient is 0.05 K for both RTD positions. The temperature gradient along this offset is linear. Compared with the vertical gradient across the wedge, the error between the RTD and surface temperature is negligible on the whole. However, the offset becomes significant close to the wedge aperture, exceeding 0.25 K.

V. Discussion

While the simulated scenario has not been replicated during testing, other tests in a laboratory atmosphere show a gradient of 0.6 K between the bottom and top of the wedge. During thermal cycling in vacuum (TVAC), the recorded wedge gradients were around 0.3 K, with a more homogeneous temperature environment than simulated. When using the data presented in Fig. 3 and focusing on the readings taken inside the OBCT aperture (coupling $\geq$ 99%), a temperature gradient is apparent for higher frequencies. Fig. 14 shows a zoomed-in plot where only the samples inside the OBCT aperture are considered. The gray area represents the temperature spread of the OBCT's RTDs. For the 54-GHz band, there is no variation, but considering the large beam size covering more of the wedge, combined with the large skin depth meaning absorption of the transmitted wave occurs across many reflections, this is expected. The gradient becomes more apparent with the increase in frequency and decrease in beam size, consistent with the two aforementioned factors. The 325-GHz band exceeds the measured temperature range for scan angles +9 to +11° off zenith. When considering RTD accuracy, how high these measurements sit in the wedge (Fig. 2), and the large delta between surface temperature and RTD measurement at those heights, it can explain this deviation. To avoid large calibration errors, it is advisable to disregard the measurements high up the wedge and restrict the scan range to a ±5° range around the apex of the wedge. As these measurements are not calibrated properly, but scaled according to the highest temperature measured in the OBCT, the absolute brightness temperatures shown here will not be accurate. However, it shows that the relative variations are realistic and demonstrate the effects discussed in this article. If the vertical gradient during operation is sufficiently low, e.g. less than 0.2 K, combined with the uncertainty of the RTDs (±0.15 K) it may be acceptable to use the OBCT without any further corrections of the effective brightness temperature. If the vertical gradient in operation is closer to the worst case thermal simulation of 0.7 K, it is possible to combine the GRASP simulations with the calculations of transmission and skin depth to build a ray tracing model of the OBCT and generate a weighting table for the RTDs which is frequency- and scan-angle-dependent. A further improvement is to more accurately calibrate the RTDs, reducing their uncertainty.

VI. Conclusion

The AWS OBCT consists of a wedge-shaped nonmagnetic absorber. The absorber is a three-part epoxy mixture cast onto an aluminum structure. The three parts are Stycast 1266,

carbon black powder, and boron nitride. Permittivity measurements at 26–40 GHz were used to simulate performance across the AWS bands for different thicknesses of a wedge with a 24° opening angle. Subsequent measurements of the finished OBCT showed a return loss better than 50 dB for TM mode, as predicted. As the beams are not co-aligned in the quasi-optics of the AWS radiometer, each frequency band couples differently into the OBCT aperture. Simulations using GRASP showed that the scan range of the primary mirror over which the coupling into the OBCT is greater than 99% is different for each band. Second, due to the varying beam sizes and their divergence from the primary mirror boresight, each band illuminates different parts of the OBCT aperture for a given scan angle. Furthermore, skin depth calculations for each band show that for the lowest three frequency channels, one reflection is not sufficient to absorb 99% of the transmitted energy. If the OBCT was homogeneous in temperature, this would not affect the calibration, but thermal simulations show that this is not the case. In the worst case scenario presented in this article, a temperature gradient of 0.7 K between the apex and the aperture of the OBCT is predicted, but data from TVAC testing show smaller gradients closer to 0.3 K. Horizontal temperature gradients between the RTD and the absorber skin are negligible for the majority of the wedge, but do become significant near the wedge aperture. Measurements taken from the AWS radiometer flight model confirm the anticipated effect of beam size and skin depth on the measured brightness temperature of the OBCT when a temperature gradient is present. Appropriate compensation for these effects will depend on the temperature gradient measured during in-orbit operation.

ACKNOWLEDGMENT

The authors would like thank Kalle Kempe from AAC Omnisys for providing test data from AWS PFM. They would also like to thank Daniele Piazza, Mathias Brändli, and Martin Rieder for the mechanical design of OBCT.

REFERENCES

[1] A. Schröder et al., "Electromagnetic design of calibration targets for MetOp-SG microwave instruments," *IEEE Trans. Terahertz Sci. Technol.*, vol. 7, no. 6, pp. 677–685, Nov. 2017.

[2] Q. Liu and J. A. S. S. Team, "Joint Polar Satellite System (JPSS) advanced technology microwave sounder (ATMS) SDR calibration algorithm theoretical basis document (ATBD)," Center Satell. Appl. Res., College Park, MD, USA, Tech. Rep. D0001-M01-S01-001_JPSS_ATBD_ATMS_SDR_B, 2022.

[3] H. Yang et al., "The FengYun-3 microwave radiation imager on-orbit verification," *IEEE Trans. Geosci. Remote Sens.*, vol. 49, no. 11, pp. 4552–4560, Nov. 2011.

[4] K. Jacob, A. Schroder, M. Kotiranta, and A. Murk, "Design of the calibration target for SWI on JUICE," in *Proc. 41st Int. Conf. Infr., Millim., Terahertz Waves (IRMMW-THz)*, Sep. 2016, pp. 1–2.

[5] R. V. Leslie, W. J. Blackwell, A. Cunningham, M. DiLiberto, J. Eshbaugh, and I. Osaretin, "Pre-launch calibration of the nasa tropics constellation mission," in *Proc. IEEE Int. Geosci. Remote Sens. Symp.*, Sep. 2020, pp. 6441–6444.

[6] S. Padmanabhan et al., "TEMPEST-D radiometer: Instrument description and prelaunch calibration," *IEEE Trans. Geosci. Remote Sens.*, vol. 59, no. 12, pp. 10213–10226, Dec. 2021.

[7] EUMETSAT. (2024). *Towards EPS-Sterna*. Brochure: PRG. FS.03, V1. [Online]. Available: https://www.eumetsat.int/media/51305

[8] R. Albers, A. Emrich, and A. Murk, "Antenna design for the Arctic weather satellite microwave sounder," *IEEE Open J. Antennas Propag.*, vol. 4, pp. 686–694, 2023.

[9] K. Jacob, A. Schröder, and A. Murk, "Design, manufacturing, and characterization of conical blackbody targets with optimized profile," *IEEE Trans. Terahertz Sci. Technol.*, vol. 8, no. 1, pp. 76–84, Jan. 2018.

[10] R. F. Harrington, *Time-Harmonic Electromagnetic Fields*. Hoboken, NJ, USA: Wiley-IEEE Press, 2001.

[11] J. Baker-Jarvis, *Transmission/Reflection and Short-Circuit Line Permittivity Measurements*. Gaithersburg, MD, USA: National Institute of Standards and Technology, 1990.

[12] F. Ulaby et al., *Microwave Radar and Radiometric Remote Sensing Sensing*. Ann Arbor, MI, USA: Univ. of Michigan Press, 2014, ch. 2–4, pp. 46–47.

[13] (2023). *Table of Emissivity of Various Surfaces*. Transmetra Gmbh. [Online]. Available: https://www.transmetra.ch/images/transmetra_pdf/publikationen_literatur/pyrometrie-thermografie/emissivity_table.pdf

Roland Albers received the B.Eng. degree in aerospace engineering with Brunel University London, London, U.K., in 2015, and the M.Sc. degree in astronautics and space engineering from Cranfield University, Milton Keynes, U.K., in 2016. He is currently pursuing the Ph.D. degree in applied physics with the University of Bern, Bern, Switzerland.

Before starting the Ph.D degree, he worked in the space industry on quasi-optical components. His research interests include spaceborne radiometry, hardware design, and calibration.

Tobias Plüss (Member, IEEE) received the M.Sc. degree in electrical engineering from the Lucerne School of Engineering and Architecture, Lucerne, Switzerland, in 2017.

During his B.Sc., he worked part-time at Siemens Switzerland, Zürich, Switzerland. From 2016 to 2018, he worked as an RF Electronics Engineer at Albis Technologies AG, Zürich. He joined the Institute of Applied Physics, University of Bern, Bern, Switzerland, in 2018. His research interests include design, simulation, and measurement of RF components, measurement of material parameters, network analyzer measurement techniques, and precise frequency and time measurement.

Lars Eggimann received the B.Sc. degree in physics from the University of Bern, Bern, Switzerland, in 2023, where he is currently pursuing the M.Sc. degree in experimental physics.

His research interests include numerical simulations and general application of computer science in physics.

Axel Murk received the M.Sc. degree in physics from the Technical University of Munich, Munich, Germany, in 1995, and the Ph.D. degree in physics from the University of Bern, Bern, Switzerland, in 1999.

Since then, he has been involved in the development and characterization of millimeter- and submillimeter-wave instrumentation for different ground-based and spaceborne projects. Since 2018, he has been leading the IAP Microwave Physics Division, University of Bern. His research interests include digital real-time spectrometers and radiometric calibration of remote sensing instruments.

IEEE Open Journal of
Antennas and Propagation

Received XX Month, XXXX; revised XX Month, XXXX; accepted XX Month, XXXX; Date of publication XX Month, XXXX; date of current version XX Month, XXXX.

Digital Object Identifier 10.1109/OJAP.2023.XXXXXXX

Spillover analysis and mainbeam characterisation of Arctic Weather Satellite radiometer using method of moments

Roland Albers[1], **Mustafa Murat Bilgic**[2], **Karl-Erik Kempe**[3], **Alistair Bell**[1], **Axel Murk**[1]

[1]Institute of Applied Physics, Bern University, Bern, Switzerland
[2]TICRA, Copenhagen, Denmark
[3]AAC Omnisys, Augusta Barks Gata 6B, Västra Frölunda, Sweden

CORRESPONDING AUTHOR: Roland Albers (e-mail: roland.albers@unibe.ch).

ABSTRACT The Arctic Weather Satellite (AWS) is a single instrument mission consisting of a microwave sounder operating in the 54, 89, 183 and 325 GHz bands. The optical design of the instrument consists of a feedcluster directly illuminating a crosstrack scanning mirror, keeping the instrument compact. Due to the simple optics, the beams are not co-aligned and none are in the scanning mirror focal point, leading to beam divergence, asymmetry and scan angle dependent variations in spillover. Using Method of Moment (MoM) simulations of the optics as well as instrument structure, the complete farfield sphere of the instrument can be simulated up to 183 GHz. This paper contains detailed analysis of spillover, beam divergence and intercomparison of physical optics, MoM and nearfield antenna measurements for the mainbeam.

INDEX TERMS microwave radiometry, quasi-optics, remote sensing, Method of Moment (MoM), antenna patterns

I. Introduction

The Arctic Weather Satellite (AWS) is a crosstrack scanning radiometer on a SmallSat platform commissioned by the European Space Agency (ESA). AWS is a prototype for an operational constellation of identical satellites called EUMETSAT Polar System (EPS)-Sterna, which is currently being studied by the European Organisation for the Exploitation of Meteorological Satellites (EUMETSAT) [1]. The radiometer uses 19 channels across the 54, 89, 183 and 325 GHz bands, all in single polarisation. Six satellites on three sun-synchronous orbits are baselined for the constellation, with a projected global coverage of 90% in less than five hours [2]. Twenty satellites are required over the project lifetime, a much higher quantity than comparable operational radiometers like the Microwave Sounder (MWS) [3] and the Advanced Microwave Technology Sounder (ATMS) [4], which are part of a large and costly suite of instruments hosted on larger satellite platforms. In order to limit the cost, volume and mass the AWS radiometer optics are simplified and compacted compared to these other instruments. This enables hosting the instrument on a smaller, dedicated platform and keeping the constellation financially viable.

AWS uses a splitblock feedcluster with a smooth spline feedhorn for each band. A parabolic scanning mirror (see Fig. 1) is directly illuminated by the feedcluster without any additional optical elements. Consequently, the beams are not co-aligned and diverge from the pointing axis of the scanning mirror. The scanning mirror rotates continuously in the counter clock-wise direction from the perspective of the feedcluster. Two-point calibration is performed by cold space measurements in combination with a warm onboard calibration target (OBCT). The OBCT consists of a wedge shaped cavity coated with custom epoxy based absorber. A secondary static mirror in the zenith view of the instrument couples the scanning mirror into the OBCT aperture. A more detailed description of the optics can be found in [5], which also highlighted the significant spillover, especially at the lower frequencies and provided a breakdown of the spillover in the farfield of the instrument. However, the analysis was performed using physical optics (PO) in TICRA Tools [6] and did not consider the structure of the instrument. Since each reflection between components has to be manually considered in the PO analysis, it is not feasible to include the AWS structure. PO is only an

FIGURE 1. Picture of AWS Protoflight model. Flight direction is upwards in the image. Nadir view is out of page. Scan direction from right to left. Courtesy of AAC Omnisys.

approximation of the full wave solution, which makes it computationally lightweight and enabled simulation at the highest AWS frequency of 325 GHz. However, spillover compensation is critical for the performance of AWS and including the structure allows for a more accurate assessment of what is in view of the spillover. Therefore, further analysis was performed including the AWS structure in the ESTEAM software package from TICRA Tools [6] using Method of Moments (MoM). Typically, MoM analysis is used to assess the scattering impact of structural parts close to the reflector on the mainbeam of the instrument [7] [8]. While this analysis is also useful for AWS, the focus is to determine the fractions of spillover which see cold space, earth and added absorber on the structure so their effect can be compensated during operational use of the instrument. A description of the differences between PO and MoM in TICRA Tools and some early results for the 54 GHz band can be found in [9]. This paper provides new results up to 183 GHz, more details on the AWS structure, absorber terminations and a detailed breakdown of the spillover and its impact on the effective brightness temperature.

II. Simulation setup

A. Structural model setup

To ensure the MoM simulation was as representative as possible, the manufacturing Computer Aided Design (CAD) model of the instrument structure was used as a starting point. However, the model has to be simplified and cleaned up to keep simulation time within a practical duration. The model included many detailed features such as screwholes and weight saving pockets which are not relevant for the purposes of the simulation. To prevent increasing simulation time unnecessarily all small features in the structure were removed. Outward facing weight saving pockets not illuminated by the feedhorns were also removed. The mechanical structure is wrapped in electrically conductive Multilayer Insulation (MLI) before launch. The MLI was modelled as a thin flat plate covering the openings between the structural struts. The initial model also included larger objects such as the onboard computer and receivers. As these internal objects are electrically reflective and would not terminate any stray radiation, they have also been removed to reduce simulation time.

Prior to import into TICRA Tools all faces inside volumes have to be removed so all volumes are boolean bodies and duplicate or intersecting faces must be removed. Then the assembly CAD model was split into several submodels for inside faces, outside faces, absorber faces. It should be noted that the absorber in TICRA Tools is not modelled by assigning an arbitrary absorptivity to a face, but as a volume with dielectric properties. This volume is defined by the individual faces that constitute it. The absorber faces were imported twice to create two model variants. The first variant includes the absorber sheets, but they are modelled as a perfect electric conductors (PEC). All other faces in the model are also assumed to be PEC. The second model assigns the absorber sheets a relative permittivity ϵ and a dielectric loss tangent δ and keeps the structure as PEC. Lastly, the surface of the primary scan reflector was included in the model, which was defined inside TICRA Tools and used as the basis for the manufacturing drawing. Efforts were made to convert a point cloud from a coordinate measurement machine (CMM) to a CAD surface for an even more realistic simulation. Unfortunately, it was not possible to convert the irregular grid of the CMM point cloud (not recorded for this specific purpose) into a representative surface. The onboard calibration target and its static reflector were only included for the 180° scan angle measurement, where they are directly illuminated.

B. Absorber setup

The AWS model includes two kind of absorbers; the first absorber is attached to the structure of the AWS radiometer in order to terminate spillover at the scanning mirror. Using simple raytracing in TICRA Tools, several affected areas of the structure were identified. Specifically the slanted areas of the main support struts (covered in black absorber in fig. 1) were identified as critical since any incident radiation will be directed towards earth. As the feedcluster is positioned in the lower part of the instrument and facing upward, the immediate surroundings of the scan mirror will be the first surface that the spillover sees and also covered in absorber. These surfaces can be seen in black in fig. 3. Lastly, the flat surfaces below the roof of the instrument were also covered in absorber (visible on the right of the scan mirror in Fig.

IEEE Open Journal of
Antennas and Propagation

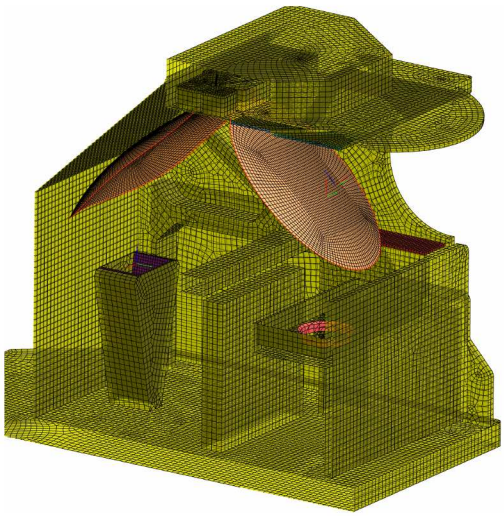

FIGURE 2. Section view of TICRA Tools mesh for the OBCT view (180°)

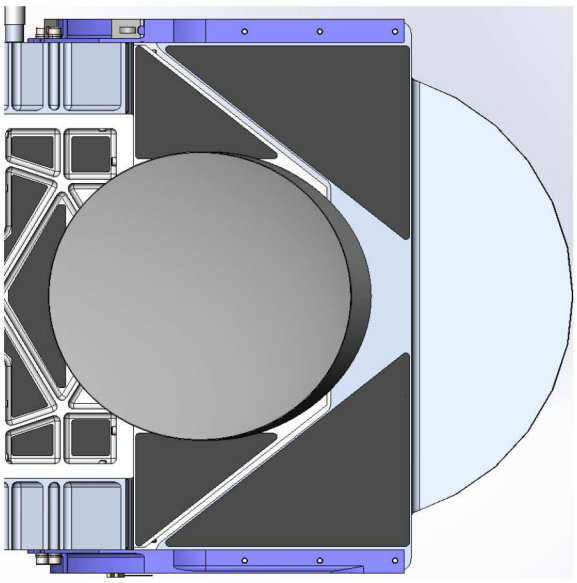

FIGURE 3. CAD Model of AWS roof underside from perspective of the feedcluster. Black surfaces show added absorber panels.

2) to terminate reflections from the roof. The absorber is a commercially available product with space heritage made of flexible sheets with an adhesive. TICRA Tools models absorber as a real volume with dielectric properties, which were not publicly available. A return loss of 5 dB across the AWS frequency bands was assumed for the simulations, based on available data and measurements. Prior to the AWS simulations, supplemental simulations were performed to find dielectric properties equivalent to the 5 dB return loss for each frequency band.

The second absorber is a custom made epoxy based mixture developed by the Institute of Applied Physics (IAP) from Bern University for the AWS OBCT. For this material the dielectric properties were known and could be used directly in the simulation. They equate to a return loss of 55 dB for the OBCT which corresponds to the measured performance. Further details of the OBCT can be found in [10].

C. Computational setup

Typically, optical simulations for electrically large structures are performed using PO which is a good approximation of the full wave solution and computationally lightweight. However, when considering complex reflections between different surfaces such as the AWS structure using PO each reflection has to be manually included in TICRA Tools. The MoM methodology directly calculates the surface currents of the entire model which gives a more accurate solution than the PO approach and automatically includes the reflections between components. Its downside is the large amount of computing resources required compared to PO. However, the MoM/multilevel fast multipole method (MLFMM) solver in TICRA Tools discretises the geometry using higher-order quadrilateral patches and surface currents using higher-order basis functions, which reduces the required computational resources and makes it possible to run a full-wave analysis on the complete structure in a short time. A distinction between the two approaches within TICRA Tools has previously been published [9]. The computing cost for the 325 GHz exceeds practical limitations with the available hardware and was not attempted. Since the 325 GHz band has very low spillover (≈0.2%) due to under-illumination of the scan mirror, it is also not relevant for the work in this paper. Further reduction in computing time was achieved by setting the external faces of the model (where little current is expected) to "reduced accuracy" [6]. This setting reduces the order of the polynomials (p) used to model the surface currents, reducing computational load. It is not related to the mesh size (h). For this paper simulations in the 54, 89 and 183 GHz bands were performed with three frequencies per band. The simulations covered five scan angles: -33° (earth), 0° (earth, nadir), +33° (earth), +90° (cold space), 180° (OBCT view). Two models were used for each scan angle, which are the aforementioned PEC and absorber models. In total 32 simulations (18 on PEC model and 18 on absorber included model) were performed per frequency band. Table 1 summarises the simulation properties for each frequency band and model. It should be noted that the listed simulation time is for one scan angle only. The details of the 54 GHz simulation setup have previously been published [9], but are included here for ease of reference. The simulations were run on two machines. An HPE ProLiant DL380 Gen 10 server with 64 logical cores and 1536 GB RAM made available by TICRA and a node of the UBELIX high performance

computing cluster of Bern University with 128 logical cores and 1000 GB RAM.

TABLE 1. Simulation Setup Details

54 GHz Band	PEC	Abs 5 dB
Expansion Accuracy (p)	Normal	Normal
Max Mesh Length (h)	1.3λ	1.3λ
Number of Unknowns	1.95 M	2.53 M
Required Memory	49 GB	121 GB
Simulation Time	$\approx$ 0.5 day	$\approx$ 2 days

89 GHz band	PEC	Abs 5 dB
Expansion Accuracy (p)	Normal	Normal
Max Mesh Length (h)	1.5λ	1.5λ
Number of Unknowns	4.19 M	5.15 M
Required Memory	104 GB	207 GB
Simulation Time	$\approx$ 2 days	$\approx$ 8 days

183 GHz Band	PEC	Abs 5 dB
Expansion Accuracy (p)	Normal	Normal
Max Mesh Length (h)	2λ	2λ
Number of Unknowns	17.49 M	18.52 M
Required Memory	644 GB	758 GB
Simulation Time	$\approx$ 8 days	$\approx$ 32 days

III. Results

A. Grid description

The full wave solution from each simulation was projected on an identical farfield sphere using a spherical coordinate system (Azimuth/Elevation) with a resolution of 0.25° centered on the scanning mirror. The origin of the grid was fixed in the nadir view of the satellite equivalent to 0° scan angle, irrespective of the scan angle in the simulation. The Elevation (Y) axis was aligned with the flight direction of the instrument, which is the upwards direction in Fig. 1. The Azimuth (X) axis was aligned with the scan plane of the mirror pointing left in Fig. 1.

B. Regions of interest

To assess the distribution of the spillover across the sphere it needs to be split into several regions of interest. The first distinction is between cold space and earth. This is achieved by plotting the earth outline in the spherical coordinate system for an assumed orbital height of 600 km. It can be seen in solid white in Fig. 4. It should be noted that the outline of earth for lower orbital heights is not circular in a spherical coordinate system. This is due to the deformation of the grid elements towards the poles of the coordinate system ($\pm$90° Elevation).

Since the objective is to quantify the spillover energy in these regions, the mainbeam needs to be isolated from these regions (depending on scan angle position). The mainbeam is determined by fitting an ellipse [11] to the full width half maximum (FWHM) contour of the beam and scaling it up

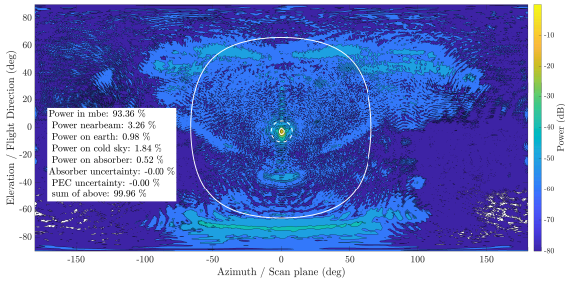

FIGURE 4. Full sphere projection of AWS farfield for 89 GHz. Scan direction from left to right. Earth outline in solid white. Nearbeam threshold in dashed white.

2.5 times. However, the area close to the mainbeam still contains a significant amount of power, as is expected for any real beam with sidelobes and aberrations from the mirror. It is labelled as the nearbeam in this paper. Furthermore, the nearbeam is also not spillover, but originates from the scanning mirror. Precisely isolating the nearbeam from the scattering of the structure is not straightforward and instead an approximation is used. The nearbeam is defined as a circular area around the peak of the mainbeam with a radius of 4 times the FWHM. In the case of the 180° scan angle simulation, there is no mainbeam or nearbeam since they are both terminated in the OBCT.

Lastly, the amount of power terminated by the absorber is of interest. But the absorption occurs before the farfield is projected and cannot be identified on the projection. Instead, its effect is spread across the sphere as an overall reduction in total power. The total power integral for the full sphere of the PEC model adds up to 4π as is expected for an electromagnetic simulation with no losses. For the Abs 5 dB model the total power integral will be less than 4π due to the losses induced by the absorber. Consequently, the terminated power is found by the difference between the total power of the two different models.

The total power in each aforementioned region is integrated and expressed as a percentage of 4π. For the mainbeam region, the power integral equates to the uncompensated mainbeam efficiency (MBE). There are two checks to ensure that the integration has been performed correctly. Firstly, the total power integral of both the PEC and Abs 5 dB model are compared to the native TICRA Tools output for the power integral. These are labelled as the uncertainties for the two models. Secondly, the sum of all the regions should add up to 100% since they fully describe the sphere.

Although the higher frequency simulations passed both checks, there was a power deficiency of up to 1% in the sum of the 54 GHz simulations. It could be traced back to a deficiency in total power of the PEC grid, shown by both the manual integration and TICRA Tools output. It was discovered this was due to parts of the AWS structure being in the nearfield of the spherical wave expansion (SWE) file used for the feedhorn. Fig. 2 shows the corresponding

IEEE Open Journal of
Antennas and Propagation

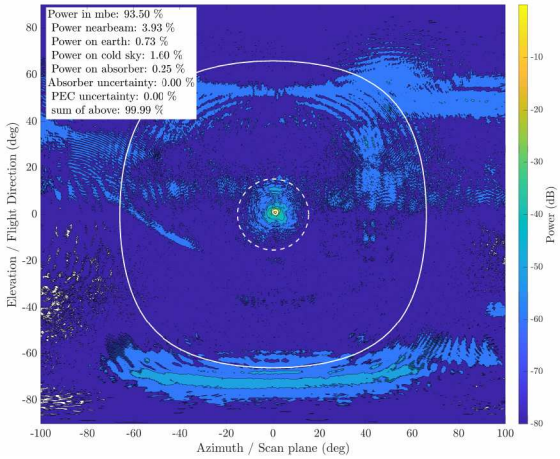

FIGURE 5. Full sphere projection of AWS farfield for 165.5 GHz. Scan direction from left to right. Earth outline in solid white. Nearbeam threshold in dashed white.

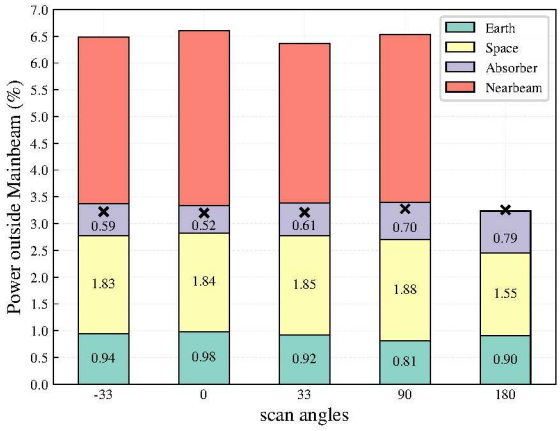

FIGURE 6. Breakdown of power in regions of interest for 89 GHz. Crosses indicate spillover from scanning mirror based on PO simulations.

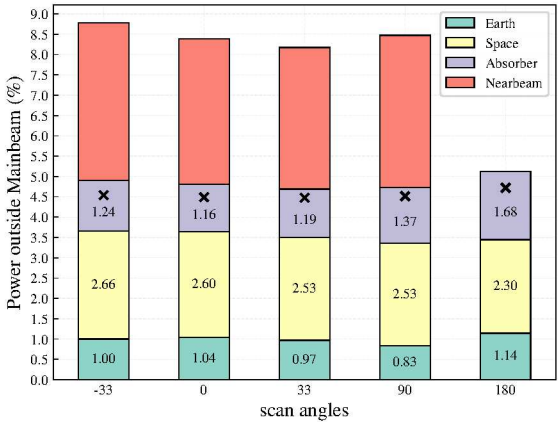

FIGURE 7. Breakdown of power in regions of interest for 50.3 GHz. Crosses indicate spillover from scanning mirror based on PO simulations.

structure in red below the scanning mirror. TICRA Tools automatically truncates the amount of modes used to form the antenna pattern which lead to a reduction in the total power of the pattern. The truncation was compensated by rescaling the 54 GHz farfields back to 4π. If the feedhorn was modelled as a scatterer in the simulation this truncation would not have occured.

C. Spillover breakdown

For the 183 GHz band it was not possible to simulate the same range of scan angles than for the lower channels. Instead conclusions on the scan angle behaviour from the two lower bands will be applied to the 183 GHz band. Fig. 5 shows the nadir farfield pattern for the 165.5 GHz channel. As expected the total spillover is less than that of the two lower bands. The most significant spillover region is cold space (1.6%) from the main spillover lobe in the lower part of the figure. The absorber terminates only a small amount of spillover (0.25%) and the earth spillover is less than half that of cold space at0.73%.

Fig. 7 and 6 show a summary of the integrated energy in the regions of interest outside the mainbeam for the worst case channel 50.3 GHz and the 89 GHz channel. This analysis has been performed for two further 54 GHz channels which are not shown here for the sake of brevity.

Firstly, as a cross check to the PO simulations the sum of the "Earth", "Sky" and "Absorber" components should be very close to the total spillover of the scanning mirror. This is based on the assumption that the energy in the mainbeam and nearbeam are solely due to the reflection of the scanning mirror and contained within those two regions. Naturally the beam tapers into the spillover energy and the hard cutoff used here is only an approximation. Furthermore, stray spillover energy will be included in the mainbeam and nearbeam. However, it is expected that the sum of regions and total spillover should be close. A good indication that the approach is valid can be seen in the 180° view for 89 GHz. Previous analysis showed that the spillover of the calibration mirror and OBCT aperture for this band is less than 0.1% and that the OBCT has a return loss of better than 55 dB [10]. Consequently, the beam is terminated to negligible energy levels and the farfield integral should be equal to the spillover of the scanning mirror. The total spillover for each scan angle is marked by the black cross in each plot. The absolute difference between the integral and the total spillover is 0.02%, which is negligible. For the other scan angles, the maximum difference is 0.18%. For 50.3 GHz there is a larger difference of 0.40%, but this can be due to the higher combined spillover of the calibration mirror and OBCT aperture, which is approximately 0.7%. Both the Sky and Earth regions are highest for the 180°

TABLE 2. Assumed Brightness temperatures for each region of interest

50.3 GHz	BT_{abs}	BT_{space}	BT_{earth}	BT_{sc}	BT_{obct}
	283.5 K	2.7 K	235.0 K	254.3 K	293.5 K
89.0 GHz	BT_{abs}	BT_{space}	BT_{earth}	BT_{sc}	BT_{obct}
	283.5 K	2.7 K	203.7 K	257.8 K	293.5 K

scan angle, further supporting that there is extra energy in the sphere from the spillover. Across the other scan angles the maximum difference is 0.36%.

Secondly, the variation of each region across the scan angles should be examined. If there is little variation, it might be sufficient to use a static correction factor independent of scan angle, reducing overall complexity of the spillover compensation. However, it is clear that the variation between the scene views (±33 and 0°) and the cold space and OBCT views (90° and 180°, respectively) is significant. The variations tend to be smaller between the scene views. Since not every scene view can be simulated, it is important to assess the error that is introduced by assuming a static correction factor for each region of interest across the scene views. For a first approximation each regions power fraction P can be multiplied by a Rayleigh-Jeans brightness temperature BT difference to the scene brightness temperature BT_{sc} to calculate the effective brightness temperature BT_{eff}:

$$BT_{eff} = P_{MB} \cdot BT_{sc} + P_{NB} \cdot BT_{sc} + P_{earth} \cdot BT_{earth} + P_{space} \cdot BT_{space} + P_{abs} \cdot BT_{abs} \quad (1)$$

Inevitably, some assumptions and simplifications are made for this calculation. Firstly, the absorber and cold space are assumed to have the same brightness temperature for both frequencies. The absorber brightness temperature is based on the minimum operating temperature of the instrument and the cold space on the cosmic background radiation. The brightness temperatures for the scene and earth spillover were determined using a 1D simulation of the atmosphere in the Atmospheric Radiative Transfer Simulator (ARTS) software [12]. All of the earth spillover is assumed to be on flat ocean with an emissivity of 0.6 based on a model developed by [13], while the scene is assumed to be wooded savannah with estimates of emissivity (0.95) taken from [14] and [15]. As a worst case scenario this is equivalent to the mainbeam and nearbeam fully illuminating an island. For atmospheric conditions no cloud cover was assumed. Lastly, for the OBCT temperature, which is the scene for the 180° scan angle, a frequency independent brightness temperature in the middle of the operating temperature range was chosen. Since the OBCT is positioned deep inside the instrument, it is anticipated that it will differ in temperature to the more exposed absorber on the structure. A summary of all brightness temperatures is provided in Table 2.

TABLE 3. Brightness temperature breakdown per scan angle

		50.3 GHz		
scan angle	BT (K)	diff to scene	mean (K)	delta mean
-33°	247.595	-6.705		-0.146
0°	247.715	-6.585	247.741	-0.027
33°	247.914	-6.386		0.172
90°	8.493	5.793		
180°	285.970	-7.530		
		89 GHz		
scan angle	BT (K)	diff to scene	mean (K)	delta mean
-33°	252.682	-5.118		-0.034
0°	252.618	-5.182	252.648	0.030
33°	252.645	-5.155		-0.003
90°	6.299	3.600		
180°	288.111	-5.389		

Table 3 shows the effective brightness temperatures (BT) per scan angle for both frequencies. The second column summarises the BT difference to the corresponding scene BT. It is clear that the spillover needs to be accounted for as the BT errors are very significant. For the earth scene the the third column shows the mean BT across the scene views. This mean is created by using equation 1, but for each region of interest the power fraction is averaged across the earth views. It is necessary to use this approach for the 183 GHz channel as the nadir simulation is the only available simulation. The rightmost column shows the difference of each scene view compared to the mean. For the 50.3 GHz channel the absolute difference is ≈0.15 K and 0.17 K for the ±33° views and significantly smaller for the nadir view (≈0.03 K). Considering Fig. 7, this is due to the asymmetrical change of the power fractions. Specifically the cold space view, which is far from the scene BT does not vary symmetrically about nadir, but instead decreases linearly with scan angle. Furthermore this channel has the highest variation in total spillover, which will be a contributing factor to the variation. Consequently, the spillover compensation for this channel should use a scan angle specific correction based on all available simulated scenes.

At 89 GHz the difference to the scene BT is still significant and spillover corrections must be included in the instrument data processing for operational use. However, the two off-nadir views behave similarly and the overall spillover amount and its variation is lower, thus yielding only a minor deviation from the mean BT (0.03 K or less). Previous analysis shows that the 183 GHz total spillover is lower than at 89 GHz by at least 1% and with little variation across scan angles, so the potential delta to the nadir BT can be assumed to be similar to what is shown for 89 GHz.

For the channels presented here the cold space spillover is the dominating factor, which is a straightforward and predictable to compensate. Likewise, the absorber spillover on the structure is relatively straightforward to compensate using onboard temperature sensors of the instrument. How-

IEEE Open Journal of
Antennas and Propagation

ever, the earth spillover at ≈1% power fraction remains. Both channels analysed here are window channels and in reality the intricacy of the earth's geography will make correction for the scene views less predictable. Coast lines and other high contrast scenes will have a more complex impact on the effective BT. Similarly, irregular cloud cover will complicate correction of the earth spillover. When considering Fig. 8, it is apparent that the earth spillover is concentrated in certain areas and varies as a function of scan angle. It is more homogeneous for the cold space and OBCT view (not shown), but for the earth views there is a concentration in the higher elevations which is a direct illumination from spillover missing the roof of the instrument. A second concentration is located at lower elevation angles just below the nearbeam which originates from secondary reflections off the roof of the instrument. Further work is necessary to combine these antenna patterns with a full scene simulation to accurately assess the impact of high contrast scenes.

D. Mainbeam comparison to measured pattern

In order to assess the suitability of the reduced PO model to calculate performance criteria such as FWHM and MBE, the mainbeam contour from the original PO simulations for nadir [5] was compared with the MoM output. If the inclusion of the structure would have a significant effect on the mainbeam shape it would require using MoM simulations for all mainbeam performance assessments. In addition, comparing measured antenna patterns to the simulations can give further credibility to the extensive amount of simulations performed. AAC Omnisys performed antenna measurements of the AWS flight model using an inhouse purpose built nearfield scanner. These nearfield scans were converted to a farfield pattern by fourier transform and then included in the comparison plots seen in Figs. 9, 10 and 11. There are known misalignment errors with the particular measurements used for this comparison which have not been rigorously compensated and thus the plots are not an accurate assessment of absolute pointing. The primary objective of the contour analysis was to evaluate the similarity of the contour shape. To that end, the measured patterns were shifted so their beam center (peak power) coincided with that of the simulations.

The 54 GHz plot (Fig. 9) shows impressive agreement between all three contours, with minor deviations between the measurement and simulations at the -30 dB level. PO and MoM simulations show very close agreement, apart from a small feature at -30 dB outside the mainbeam which is not present in the MoM simulation. The measurement was taken at 50.0 GHz while the simulation data shown is for 50.3 GHz (lowest channel), but the change in antenna pattern is negligible. For 89 GHz (Fig. 10) there is no visible difference between the two simulations. The measured pattern shows good agreement down to -20 dB with a noticeable deviation at the -30 dB contour. Overall the measured pattern seems compressed in the y-axis at all levels compared to the

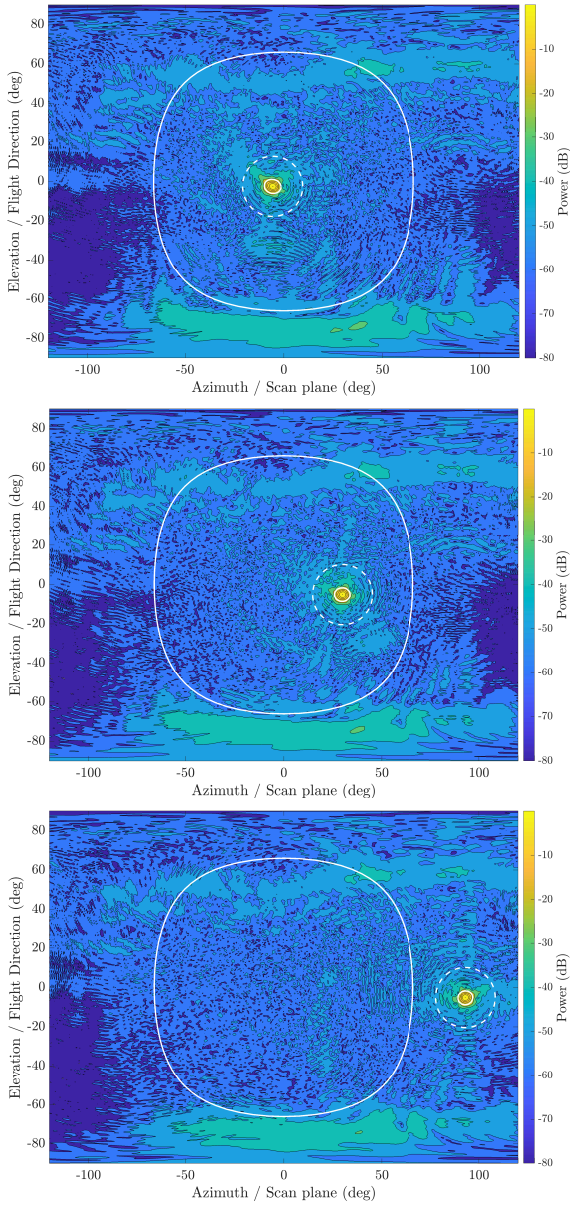

FIGURE 8. Full sphere projection of AWS farfield for 50.3 GHz. Scan angles 0, 33, 90° in descending order. Scan direction from left to right. Earth outline in solid white. Nearbeam threshold in dashed white.

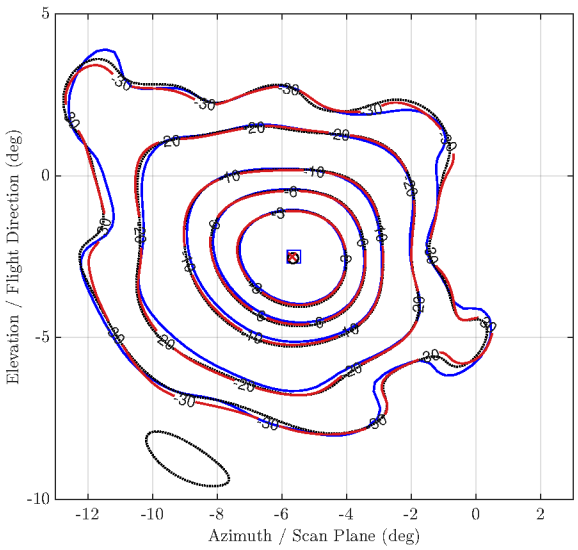

FIGURE 9. Comparison of MoM (red) vs PO (dotted) vs measured (blue) antenna pattern for 54 GHz. Contours are -3, -6, -10, -20, -30 dB. Previously in [9].

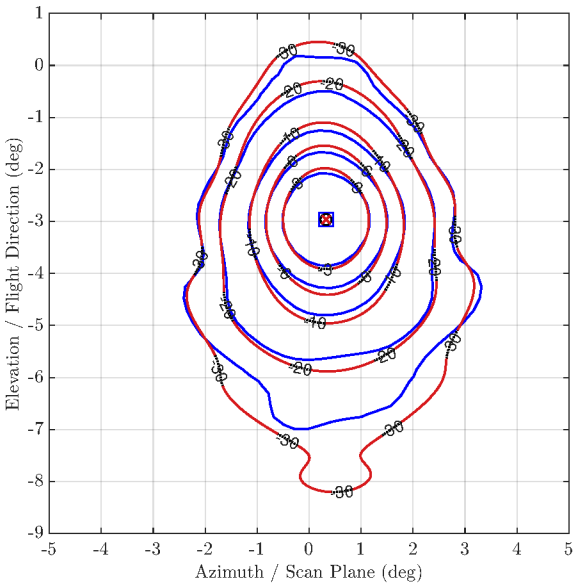

FIGURE 10. Comparison of MoM (red) vs PO (dotted) vs measured (blue) antenna pattern for 89 GHz. Contours are -3, -6, -10, -20, -30 dB.

simulations, pointing to a systematic error in this particular measurement. Like the previous plot, there is negligible difference in frequency between the simulation (89 GHz) and the measurement (88.8 GHz). Lastly, the 165.5 GHz (Fig. 11) comparison shows no visible difference between the two simulations down to -20 dB. There are negligible differences at the -30 dB level. The measured pattern also shows close agreement with the simulations down to -20 dB. However, at -30 dB there is a noticeable difference in the distinctive feature on the left side of the simulated contour. The frequency discrepancy between the measurement (165.0 GHz) and simulations (165.5 GHz) is 0.5 GHz.

E. Mainbeam rotation

The key distinguishing feature of the AWS optics is the beams' offset from the scanning mirror boresight, which were shown to rotate around the mirror boresight in [5], but did not contain a precise definition of this rotation. For accurate geolocation it is crucial to know the beam pointing for every sample. Simulating every single scan angle in PO would be possible but cumbersome and does not lend itself to lightweight and fast processing. Instead, using a combination of MoM and PO simulations, the rotation of each beam can be plotted in the fixed coordinate system described earlier in this paper, shown in Fig. 12. For each scan angle the beam center of each beam is identified, using the peak power in the pattern. A circular fit is generated from these beam centers. Fig. 12 shows such a fit for the 54 GHz beam in red. Importantly, a fit needs to be made not only for the elevation offset, but also the azimuth offset since the beams' angle in the scan plane never corresponds to the pointing angle of the

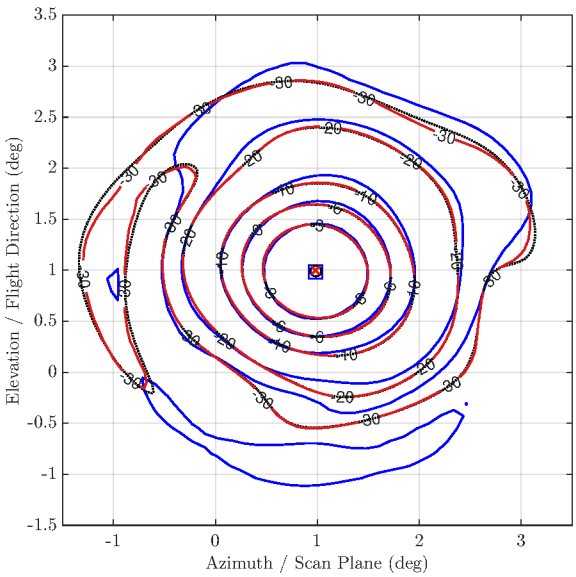

FIGURE 11. Comparison of MoM (red) vs PO (dotted) vs measured (blue) antenna pattern for 165.5 GHz. Contours are -3, -6, -10, -20, -30 dB.

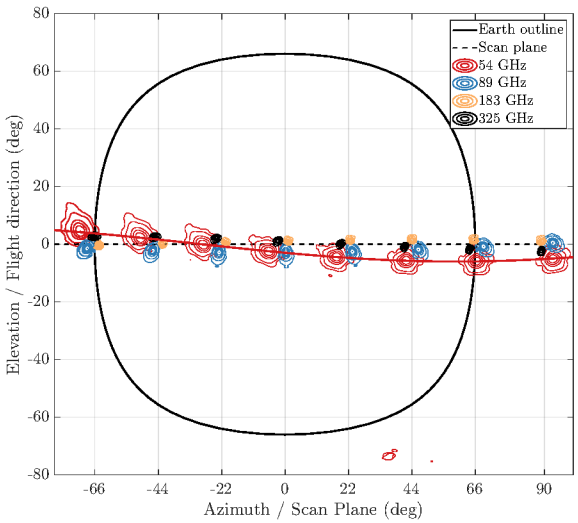

FIGURE 12. Mainbeam of all four bands for ±66, ±44, ±22, 0 and 90° scan angles. Patterns for 89 GHz and above are based on PO simulations. Red line shows circular fit for 54 GHz beam center.

TABLE 4. Circular fit coefficients for each beam

Freq (GHz)	x_0	y_0	r	β
54	-0.073	0.162	6.183	-154.385
89	0.018	-0.002	2.995	-83.216
183	-0.005	0.002	1.371	44.782
325	0.012	0.066	2.596	156.083

scanning mirror. They can then be expressed as:

$$Azimuth = \theta + x_0 + r \cdot cos(\theta + \beta) \tag{2}$$

$$Elevation = y_0 + r \cdot sin(\theta + \beta) \tag{3}$$

where θ is the scan angle position of the mirror, x_0, y_0 the center coordinates of the circle and r its radius. β is the phase offset so that the fit yields the correct coordinates for 0° scan angle. Table 4 summarises the coefficients for each beam. As expected, the center coordinates are very close to 0, which is the scanning mirror pointing axis. This confirms the beams are rotating around the pointing axis. There is a small offset present for the 54 GHz which is most likely due to the more asymmetric nature of the pattern making it more likely for the peak power to shift. The radii are proportional to the offset of the horns in the feedcluster [5] and describe the total pointing error for each beam. When examining Fig. 12 it becomes apparent that the offset for the 54 GHz is large enough to push the mainbeam into the limb at -55° scan angle, which is the angle for the first sample. For +55° the mainbeam is still positioned inside the earth outline, since the rotation of the beam is not as disadvantageous as for negative scan angles.

IV. Conclusion

A MoM simulation was performed on a CAD model of the AWS radiometer using TICRA Tools. Based on previous analysis using physical optics it was known that the total spillover of the scanning mirror is significant. With MoM it was possible to project the full sphere farfield of the instrument, including the effect of the structure and additional absorber. By dividing the farfield into regions of interest and integrating their power fraction it was possible to show the individual contribution per region. Using a simplified approach based on one dimensional ARTS simulations, an effective brightness temperature per simulated scan angle was calculated for 50.3 GHz and 89 GHz window channels. For both frequencies the effective brightness temperature differed by more than 5 K from the scene temperature, demonstrating that spillover correction is necessary for operational use of the data. Using a mean value for each region's contribution across the scene views (±33 and 0°) produces a negligible error of less than 0.03 K for the 89 GHz. However, for the 50.3 GHz channel the total spillover is higher and has a stronger variability with the scan angle. In this case the mean contribution approach results in a significant systematic bias of approximately 0.17 K or less, and a more detailed correction should be considered for this frequency band. For both channels the cold space view is the largest error contributor and is straightforward to correct, reducing the BT error. Mitigation of these effects is part of the planned level 1B processing of the instrument. The MoM simulations will be verified after launch using a series of attitude maneuvers to prove the existence of the primary spillover lobe.

A comparison between the MoM, PO and measured mainbeam patterns shows close agreement between simulated patterns for all bands and also with the measured pattern for the 54 GHz band. At 89 GHz and above there is some discrepancy between the measured and simulated pattern at the -20 dB contours and below, but there is good agreement with the overall shape and structure of the mainbeam. This gives credibility to the detailed simulation approach for spillover correction and antenna pattern characterisation for AWS.

Using a mixture of PO and MoM simulations projected on a static farfield sphere, the rotation of the beams around the pointing axis of the mirror can be expressed as a circular fit. The fit is necessary for determining geolocation and orientation of each beam for each sample across the earth view.

High contrast complex scenes for window channels have not been considered in this publication and will be part of future work.

Acknowledgments

Calculations were partly performed on UBELIX, the HPC cluster at the University of Bern. Thanks go to Catalina Medina Porcile for contributing to the ARTS simulations.

REFERENCES

[1] K. Lean, N. Bormann, and S. Healy, *Task 1.1 Evaluation of initial future EPS-Sterna constellations with 50 and 183 GHz*, 10/2023 2023. [Online]. Available:

[2] *Towards EPS-Sterna*, EUMETSAT Std., 2024, brochure: PRG.FS.03, V1. [Online]. Available: https://www.eumetsat.int/media/51305

[3] G. Tennant, D. Hurd, and V. Kangas, "The nwp contribution from the microwave sounder (mws) on metop-second generation," in *2016 14th Specialist Meeting on Microwave Radiometry and Remote Sensing of the Environment (MicroRad)*, 2016, pp. 115–120.

[4] F. Weng, X. Zou, X. Wang, S. Yang, and M. D. Goldberg, "Introduction to suomi national polar-orbiting partnership advanced technology microwave sounder for numerical weather prediction and tropical cyclone applications," *Journal of Geophysical Research: Atmospheres*, vol. 117, no. D19, 2012. [Online]. Available: https://agupubs.onlinelibrary.wiley.com/doi/abs/10.1029/2012JD018144

[5] R. Albers, A. Emrich, and A. Murk, "Antenna design for the arctic weather satellite microwave sounder," *IEEE Open Journal of Antennas and Propagation*, vol. 4, pp. 686–694, 2023.

[6] TICRA, *TICRA Tools manual version 24.0*, 2024. [Online]. Available: https://www.ticra.com/software/all-software/

[7] P. Focardi, D. Gonzalez, J. A. Harrell, and S. T. Brown, "Cowvr instrument antenna, performance verification and test results," in *2016 IEEE International Symposium on Antennas and Propagation (APSURSI)*, 2016, pp. 1375–1376.

[8] P. G. Nicolaci, C. Cappellin, R. Mizzoni, V. Lubrano, S. Contu, and B. Fiorelli, "Platform scattering analysis of the copernicus imaging microwave radiometer," in *2024 18th European Conference on Antennas and Propagation (EuCAP)*, 2024, pp. 1–5.

[9] R. Albers, M. M. Bilgic, M. Whale, and A. Murk, "Method of moment simulation of full arctic weather satellite structure," in *2024 18th European Conference on Antennas and Propagation (EuCAP)*, 2024, pp. 1–4.

[10] R. Albers, T. Plüss, L. Eggimann, and A. Murk, "Development of the onboard calibration target for the arctic weather satellite," *IEEE Transactions on Geoscience and Remote Sensing*, 2024.

[11] M. Fitzgibbon, A.W.and Pilu and R. Fisher, "Direct least-squares fitting of ellipses," *IEEE Pattern Analysis and Machine intelligence*, vol. 21, no. 5, pp. 476–480, may 1999.

[12] S. A. Buehler, R. Larsson, O. Lemke, S. Pfreundschuh, M. Brath, I. Adams, S. Fox, F. E. Roemer, P. Czarnecki, and P. Eriksson, "The atmospheric radiative transfer simulator arts, version 2.6 — deep python integration," *Journal of Quantitative Spectroscopy and Radiative Transfer*, 2024. [Online]. Available: https://ssrn.com/abstract=4815661

[13] L. Kilic, C. Prigent, C. Jimenez, E. Turner, J. Hocking, S. English, T. Meissner, and E. Dinnat, "Development of the surface fast emissivity model for ocean (surfem-ocean) based on the parmio radiative transfer model," *Earth and Space Science*, vol. 10, no. 11, p. e2022EA002785, 2023.

[14] C. Prigent, W. B. Rossow, and E. Matthews, "Microwave land surface emissivities estimated from ssm/i observations," *Journal of Geophysical Research: Atmospheres*, vol. 102, no. D18, pp. 21 867–21 890, 1997.

[15] R. Xu, Z. Pan, Y. Han, W. Zheng, and S. Wu, "Surface properties of global land surface microwave emissivity derived from fy-3d/mwri measurements," *Sensors*, vol. 23, no. 12, p. 5534, 2023.

Biographies

Roland Albers received a BEng in Aerospace Engineering at Brunel University in London in 2015, followed by an MSc in Astronautics and Space Engineering at Cranfield University in Milton Keynes in 2016. After working in the space industry on quasi-optical components, he is now pursuing a PhD in Applied Physics at the University of Bern, Switzerland. His research interests are spaceborne radiometry, hardware design and calibration.

Mustafa Murat Bilgic received a M.Sc. degree in Electrical Engineering from Istanbul Technical University/Istanbul in the field of power electronics in 2007 and a Ph.D. in the field of antennas and propagation from Yeditepe University/Istanbul in 2014. Since then he has worked in various fields as an engineer ranging from power converter and electric motor designs to metrology of biomedical devices. Currently he is working as a member of the Applied Electromagnetic Team at TICRA as an antenna engineer.

Karl-Erik Kempe received a M.Sc. degree in Complex Adaptive Systems from Chalmers University of Technology, Gothenburg, Sweden, in 2009. He has been with Omnisys Instruments since 2009, working on projects for both ground- and space-based instruments. His research interests include signal processing algorithms, development of spectrometers and optimization.

Alistair Bell received his BSc from the University of Bristol in 2015 in Physics and Philosophy, after which he went on to study for an MSc in Applied Meteorology at the University of Reading which he completed in 2017. He then pursued a PhD in Ocean, Weather and Climate with the Université Paul Sabatier in Toulouse at the Centre National de Recherches Météorologiques, on the synergy of cloud radars and microwave radiometers. He currently works as a Postdoctoral researcher in the Microwave physics group at the Institute of Applied Physics at the University of Bern. His research interests revolve around atmospheric remote sensing and radiative transfer.

Axel Murk received the M.Sc. degree in physics from the Technical University of Munich, Munich, Germany, in 1995, and the Ph.D. degree in physics from the University of Bern, Bern, Switzerland, in 1999. Since then, he has been involved in the development and characterization of millimeter- and submillimeter-wave instrumentation for different ground-based and space-borne projects. Since 2018 he is leading the IAP Microwave Physics Division at the University of Bern.His research interests include digital real-time spectrometers and the radiometric calibration of remote sensing instruments.

Supplemental plots

Section 3.4 Scanning mirror optimisation

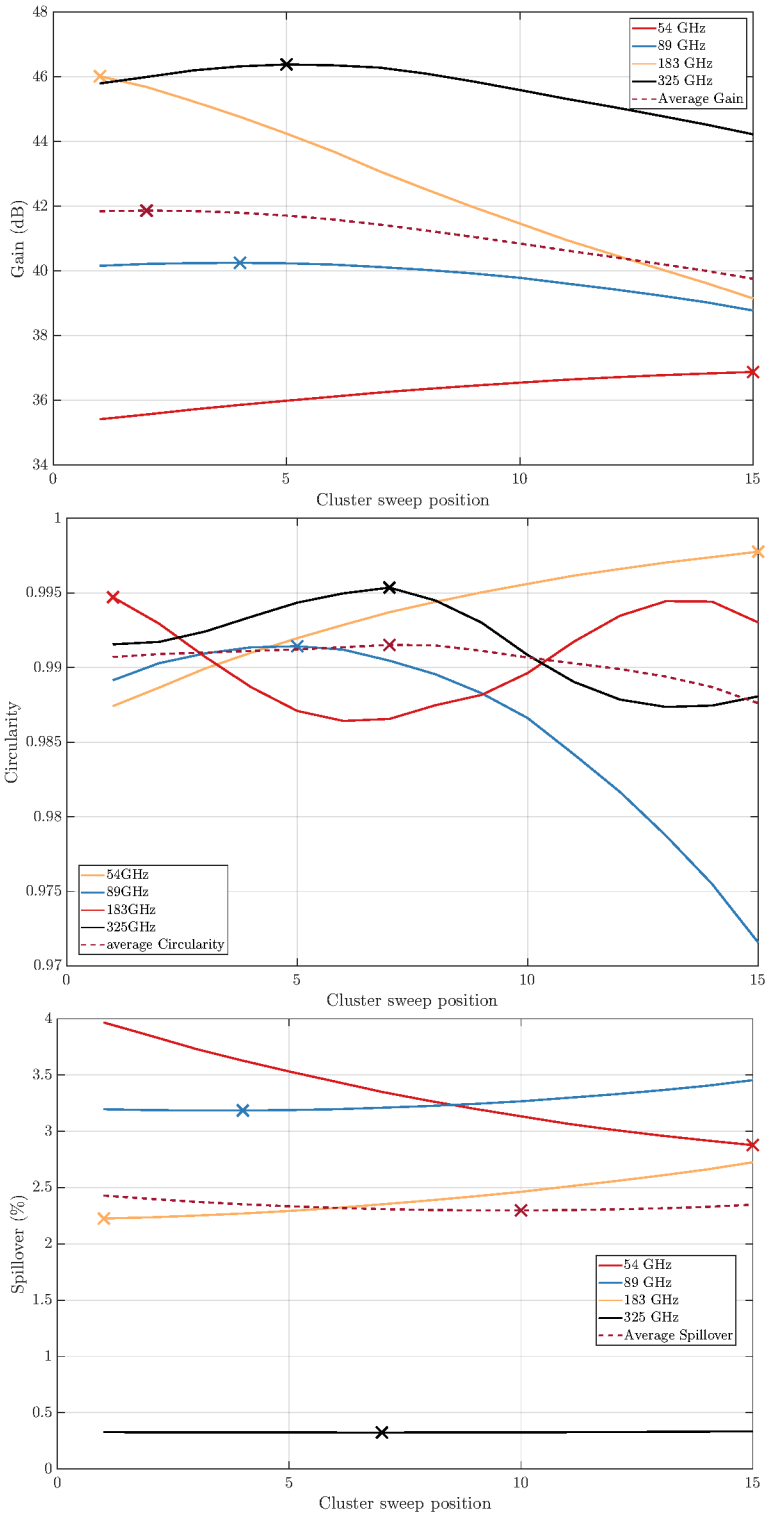

FIGURE 6.1: Peak gain, circularity and spillover for cluster sweep in mid band.

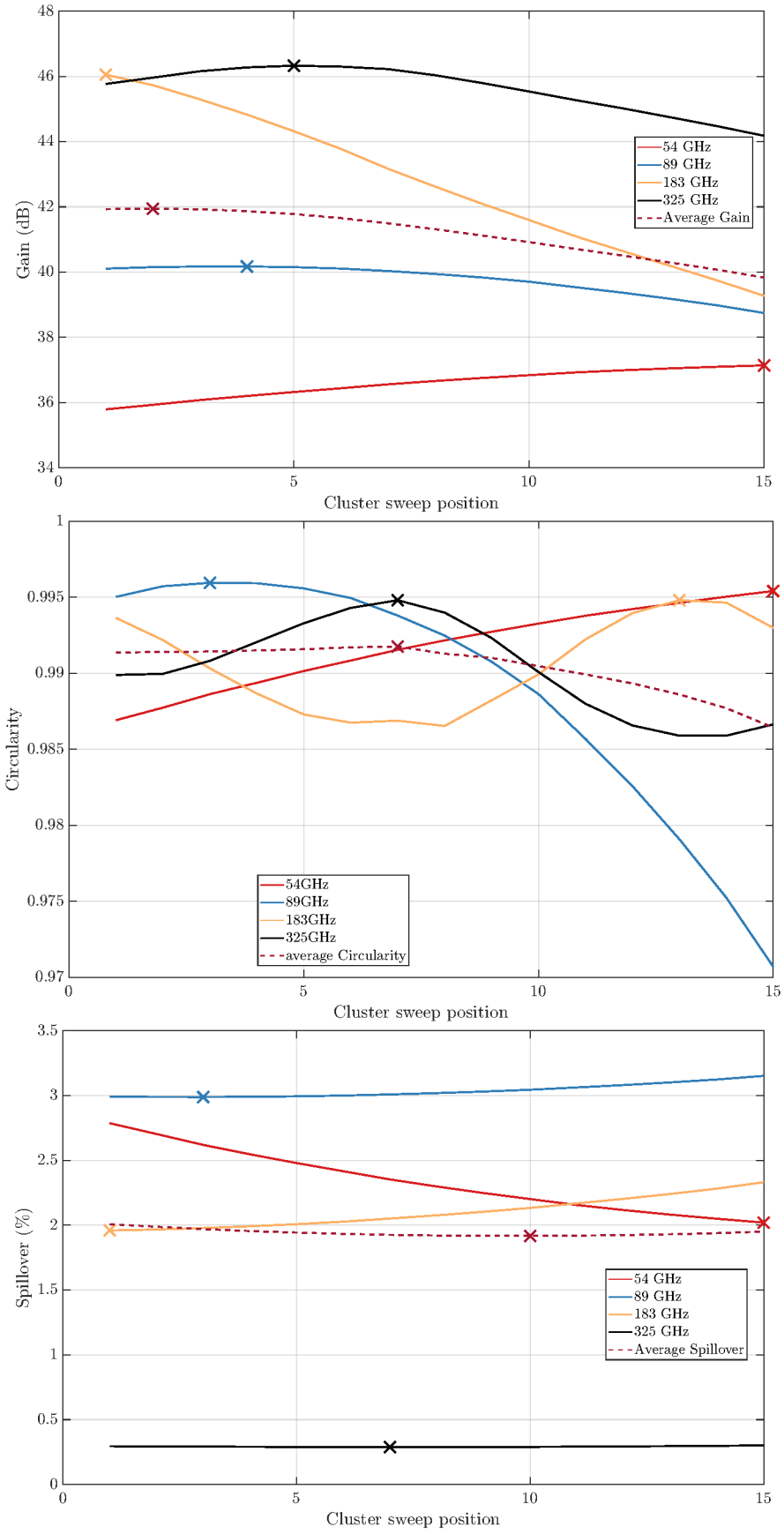

FIGURE 6.2: Peak gain, circularity and spillover for cluster sweep in high band.

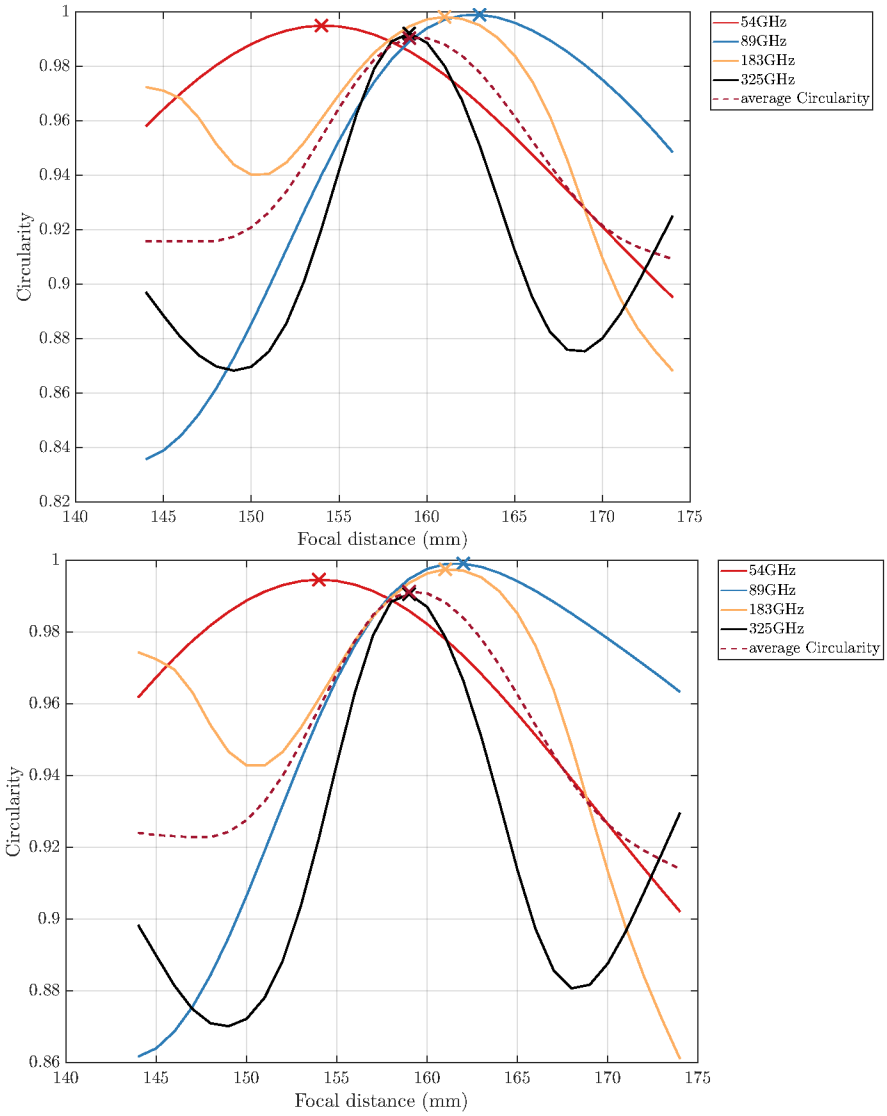

FIGURE 6.3: Circularity against distance to scanning reflector for mid and high band.

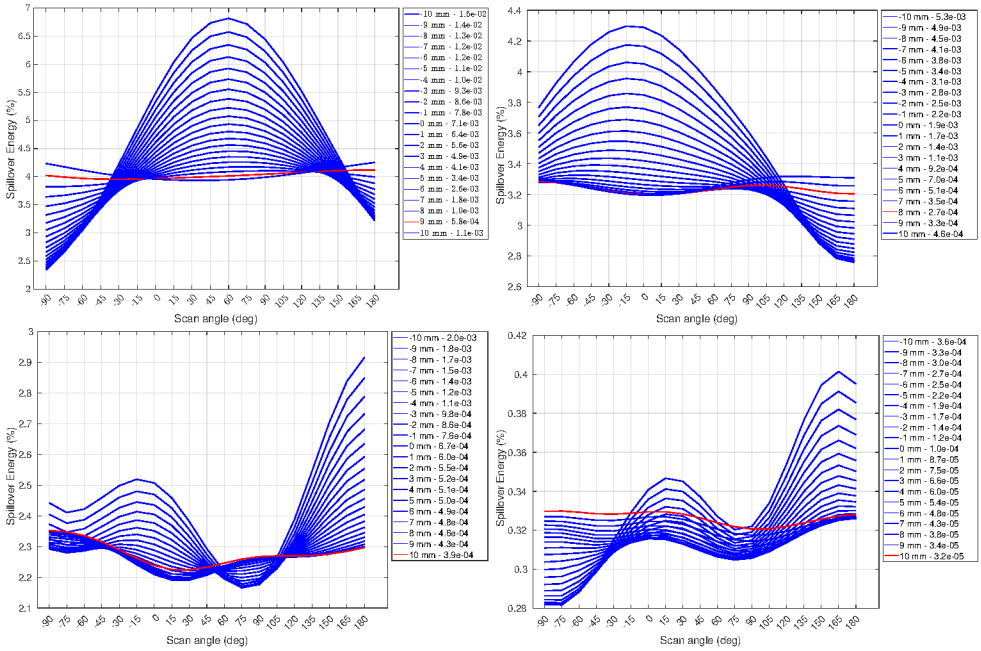

FIGURE 6.4: Spillover against mirror scan angle for different rim offsets for mid band.

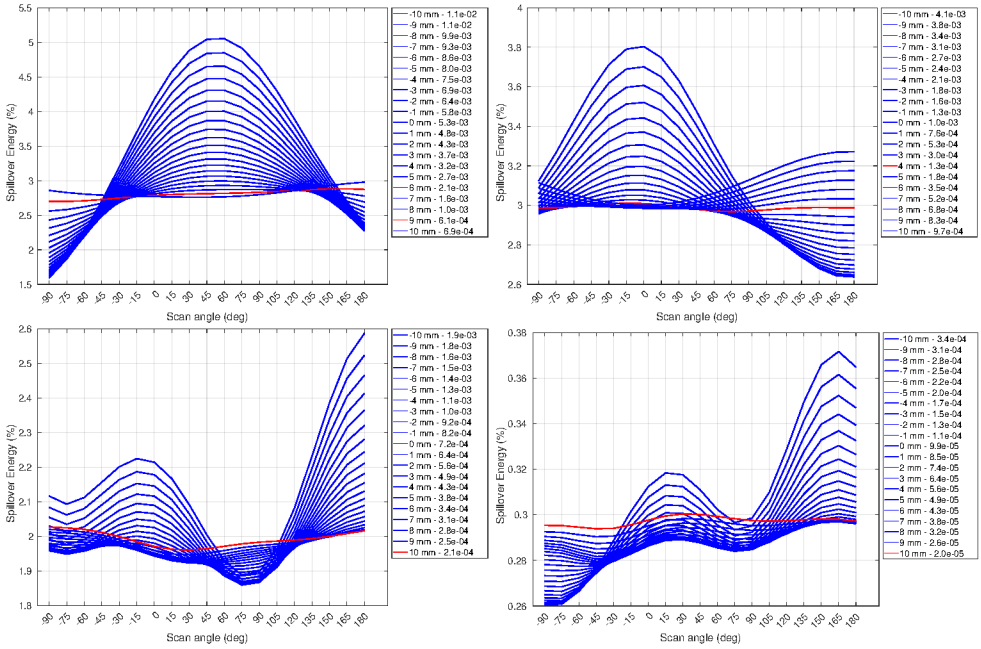

FIGURE 6.5: Spillover against mirror scan angle for different rim offsets for high band.

Section 3.8.1 Footprints

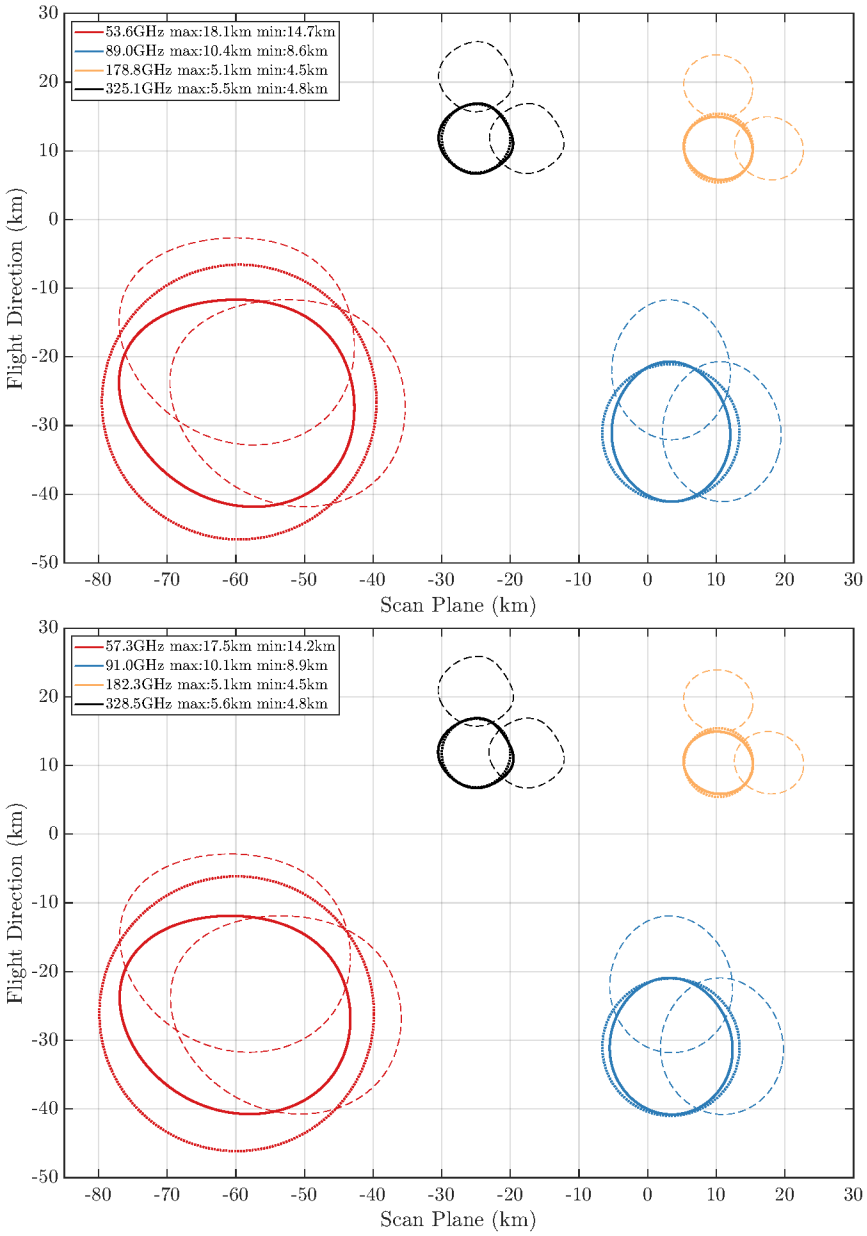

FIGURE 6.6: Mid and High band beam footprints for 600km orbital height against requirements. Dashed lines show next beam along track and next scan rotation. Dotted line shows baseline beam size.

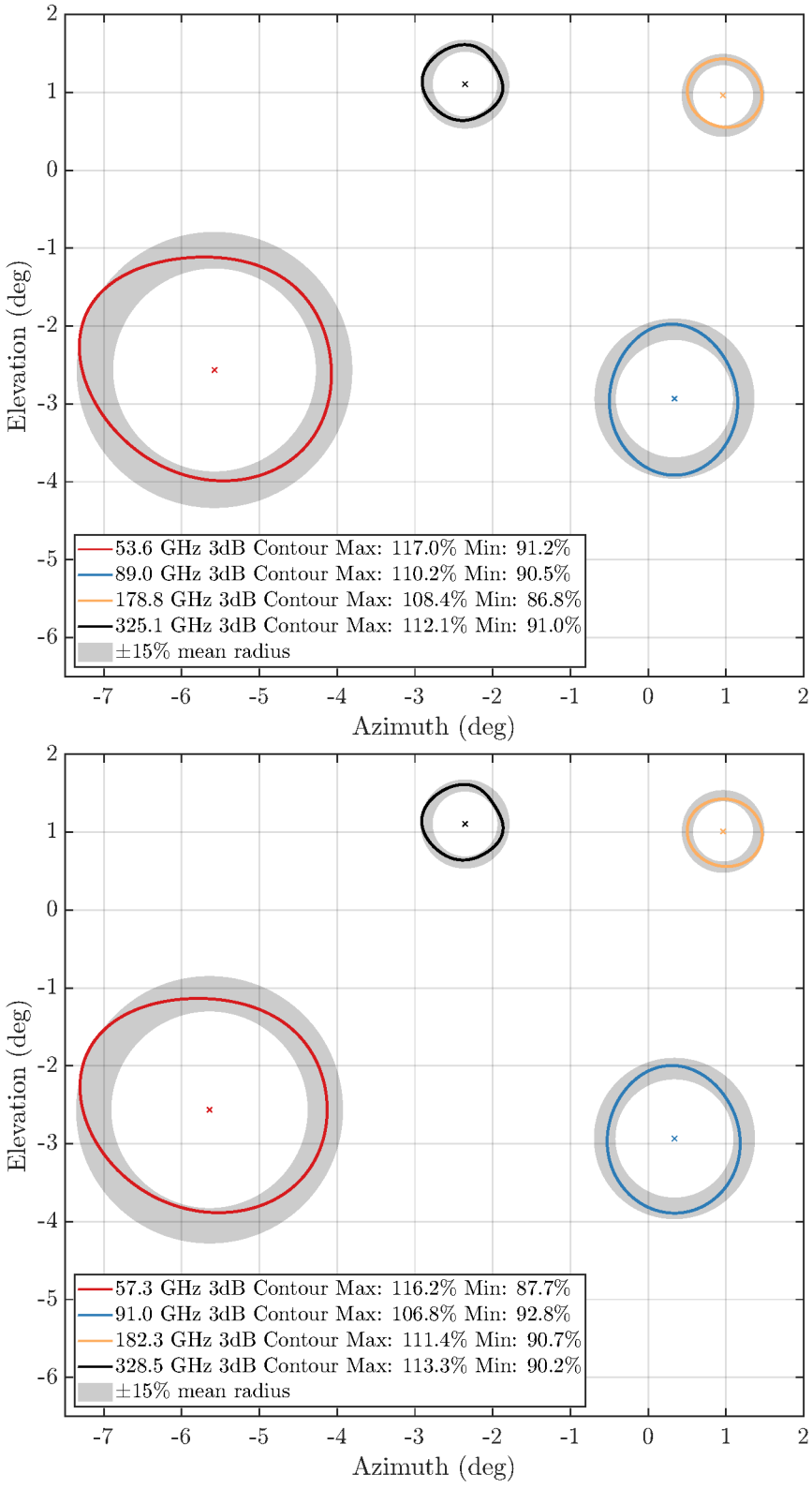

FIGURE 6.7: Mid and High band beam symmetricity against requirements

Section 3.8.2 Mainbeam efficiency

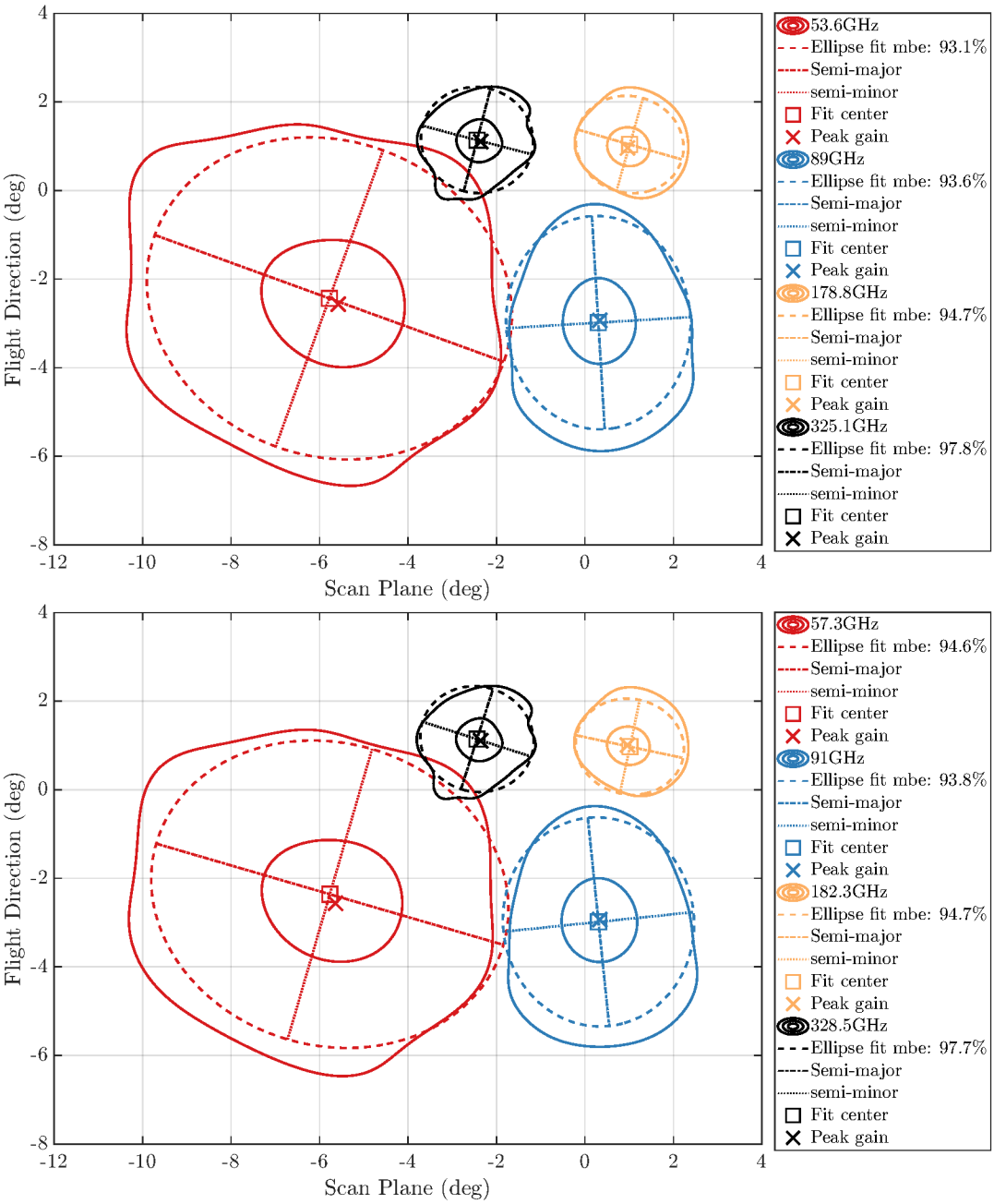

FIGURE 6.8: Mainbeam efficiencies for nadir mid and high band plotted with -3dB and -20dB contours.

Section 3.9 Full farfield sphere

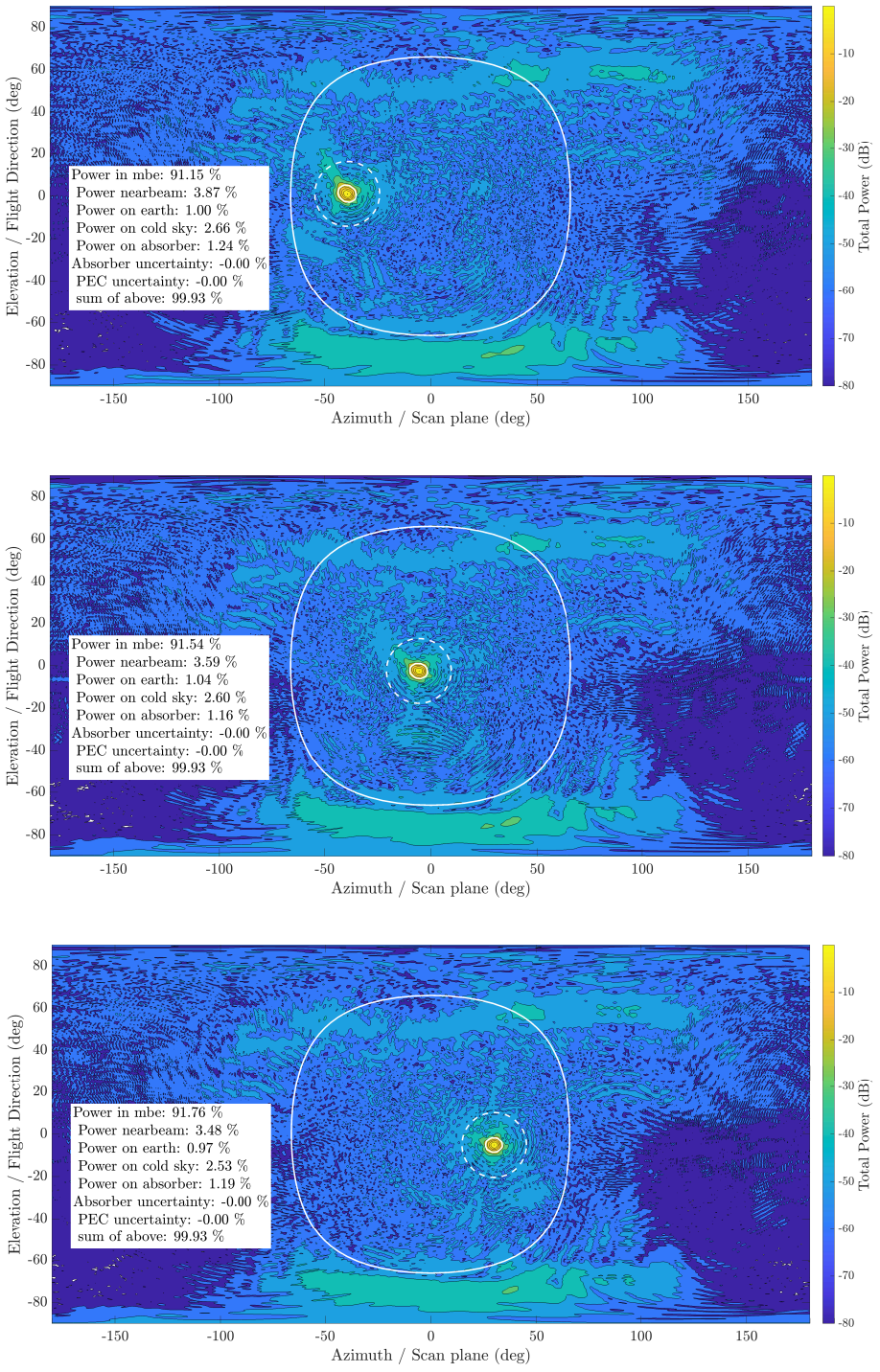

FIGURE 6.9: Full farfield sphere for 50.3 GHz for -33, 0, 33° scan angle.

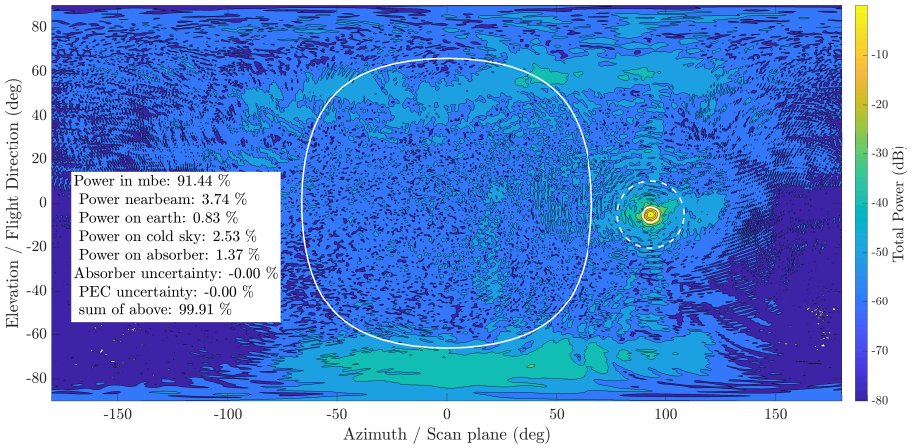

FIGURE 6.10: Full farfield sphere for 50.3 GHz for 90° scan angle.

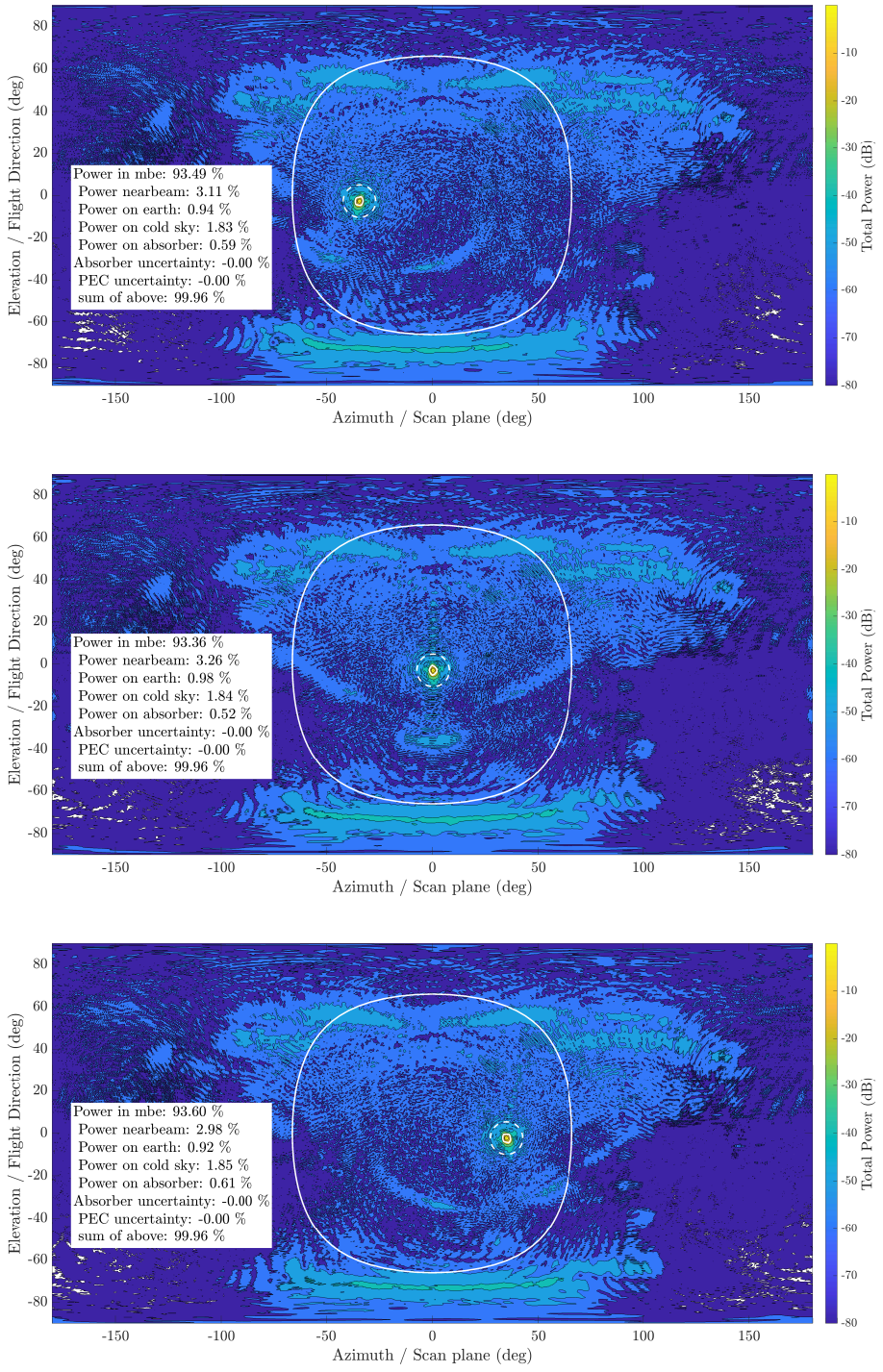

FIGURE 6.11: Full farfield sphere for 89.0 GHz for -33, 0, 33°scan angle.

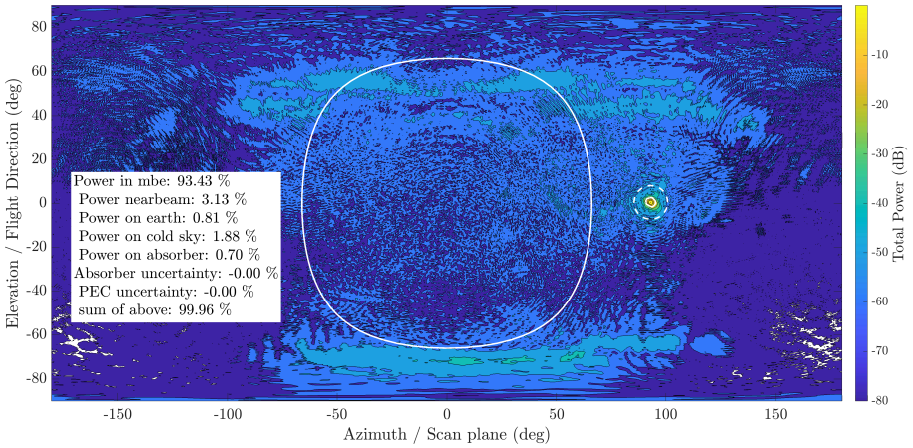

FIGURE 6.12: Full farfield sphere for 89.0 GHz for 90° scan angle-

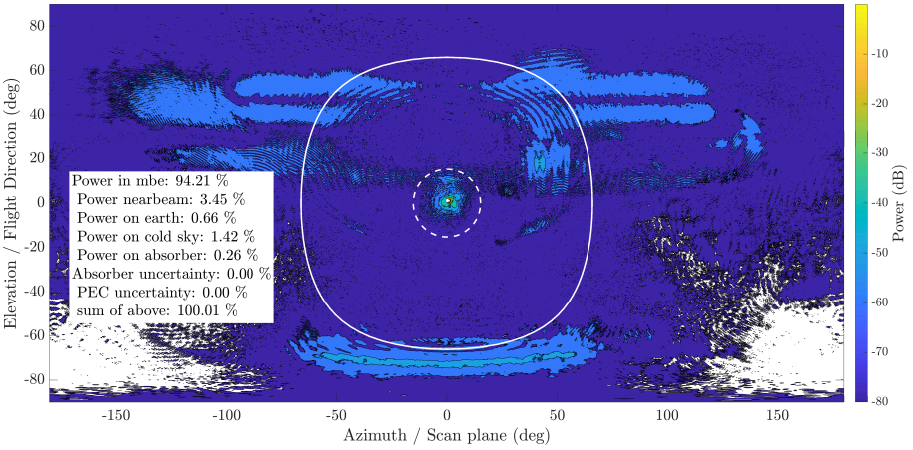

FIGURE 6.13: Full farfield sphere for 182.3 GHz for 0° scan angle.

Bibliography

[1] F. Ulaby et al. *Microwave Radar and Radiometric Remote Sensing*. Jan. 2014. ISBN: 978-0-472-11935-6.

[2] P. F. Goldsmith. *Quasioptical systems: Gaussian Beam Quasioptical propagation and applications*. Wiley-IEEE Press, 1998. ISBN: 978-0-780-33439-7.

[3] D. M. Pozar. *Microwave Engineering, 4th edition*. Wiley, 2012. ISBN: 978-1-118-21363-6.

[4] S. A. Buehler et al. 'ARTS, the Atmospheric Radiative Transfer Simulator'. In: *Journal of Quantitative Spectroscopy and Radiative Transfer* 91.1 (Feb. 2005), pp. 65–93. ISSN: 0022-4073. DOI: 10.1016/j.jqsrt.2004.05.051. (Visited on 20/09/2024).

[5] S. A. Buehler et al. *The Atmospheric Radiative Transfer Simulator Arts, Version 2.6 — Deep Python Integration*. SSRN Scholarly Paper. Rochester, NY, May 2024. DOI: 10.2139/ssrn.4815661. (Visited on 18/09/2024).

[6] P. Rosenkranz. 'Shape of the 5 Mm Oxygen Band in the Atmosphere'. In: *IEEE Transactions on Antennas and Propagation* 23.4 (July 1975), pp. 498–506. ISSN: 1558-2221. DOI: 10.1109/TAP.1975.1141119. (Visited on 20/09/2024).

[7] H. J. Liebe. 'MPM—An Atmospheric Millimeter-Wave Propagation Model'. In: *International Journal of Infrared and Millimeter Waves* 10.6 (June 1989), pp. 631–650. ISSN: 1572-9559. DOI: 10.1007/BF01009565. (Visited on 20/09/2024).

[8] P. W. Rosenkranz. 'Water Vapor Microwave Continuum Absorption: A Comparison of Measurements and Models'. In: *Radio Science* 33.4 (1998), pp. 919–928. ISSN: 1944-799X. DOI: 10.1029/98RS01182. (Visited on 20/09/2024).

[9] A. G. Peter Weston. 'Investigations into the Assimilation of AMSU-A in the Presence of Cloud and Precipitation'. In: *EUMETSAT/ECMWF Fellowship Programme Research Report* (Sept. 2019). DOI: 10.21957/ewahn9ce. (Visited on 20/09/2024).

[10] A. J. Geer et al. 'The Growing Impact of Satellite Observations Sensitive to Humidity, Cloud and Precipitation'. In: *Quarterly Journal of the Royal Meteorological Society* 143.709 (2017), pp. 3189–3206. ISSN: 1477-870X. DOI: 10.1002/qj.3172. (Visited on 20/09/2024).

[11] D. I. Duncan and N. Bormann. *On the Addition of Microwave Sounders and NWP Skill, Including Assessment of FY-3D Sounders*. Research Report 55. ECMWF, Sept. 2020. URL: https://www.ecmwf.int/sites/default/files/elibrary/2020/19760-addition-microwave-sounders-and-nwp-skill-including-assessment-fy-3d-sounders.pdf (visited on 16/09/2024).

[12] *Arctic Weather Satellite System Requirements Document (SRD)*.

[13] R. S. Anwar, L. Mao and H. Ning. 'Frequency Selective Surfaces: A Review'. In: *Applied Sciences* 8.9 (Sept. 2018), p. 1689. ISSN: 2076-3417. DOI: 10.3390/app8091689. (Visited on 16/09/2024).

[14] K. Jacob, M. Kotiranta and A. Murk. 'Transmission and Reflection Characterization of Polarizing Beam Splitters at Submillimeter Wavelengths'. In: *IEEE Transactions on Terahertz Science and Technology* 9.3 (May 2019), pp. 272–281. ISSN: 2156-342X, 2156-3446. DOI: 10.1109/TTHZ.2019.2911033. (Visited on 19/09/2024).

[15] H. Masunaga. 'Satellite Orbit and Scan'. In: *Satellite Measurements of Clouds and Precipitation: Theoretical Basis*. Ed. by H. Masunaga. Singapore: Springer Nature, 2022, pp. 29–52. ISBN: 978-981-19224-3-5. DOI: 10.1007/978-981-19-2243-5_3. (Visited on 17/09/2024).

[16] W. M. Organisation. *Observing Systems Capability Analysis and Review Tool*. Website. 2024. (Visited on 18/09/2024).

[17] *{AIRS} Project Algorithm Theoretical Basis Document Level 1b, Part3: Microwave Instruments*. Tech. rep. JPL D-17005. Jet Propulsion Laboratory, Nov. 2000. URL: https://eospso.gsfc.nasa.gov/sites/default/files/atbd/atbd-airs-L1B_microwave.pdf (visited on 17/09/2024).

[18] H. Yang et al. 'ATMS Radiance Data Products' Calibration and Evaluation'. In: *IEEE Transactions on Geoscience and Remote Sensing* 60 (2022), pp. 1–11. ISSN: 0196-2892, 1558-0644. DOI: 10.1109/TGRS.2021.3123576. (Visited on 09/01/2024).

[19] Q. Liu. *Joint Polar Satellite System ({JPSS}) Advanced Technology Microwave Sounder ({ATMS}) {SDR} Calibration Algorithm Theoretical Basis Document {ATBD}*. Tech. rep. : D0001-M01-S01-001_JPSS_ATBD_ATMS_SDR_B. National Oceanic and Atmospheric Administration, Apr. 2022. URL: https://www.star.nesdis.noaa.gov/jpss/documents/ATBD/D0001-M01-S01-001_JPSS_ATBD_ATMS-SDR_B.pdf (visited on 09/01/2024).

[20] J. Yang et al. 'Improvements on Global Meteorological Observations from the Current Fengyun 3 Satellites and Beyond'. In: *International Journal of Digital Earth* 5.3 (May 2012), pp. 251–265. ISSN: 1753-8947. DOI: 10.1080/17538947.2012.658666. (Visited on 19/09/2024).

[21] V. Kangas et al. 'Microwave Sounder Instrument for MetOp Second Generation'. In: *2014 13th Specialist Meeting on Microwave Radiometry and Remote Sensing of the Environment (MicroRad)*. Mar. 2014, pp. 232–235. DOI: 10.1109/MicroRad.2014.6878947. (Visited on 17/09/2024).

[22] A. Schroder et al. 'Electromagnetic Design of Calibration Targets for MetOp-SG Microwave Instruments'. In: *IEEE Transactions on Terahertz Science and Technology* 7.6 (Nov. 2017), pp. 677–685. ISSN: 2156-342X, 2156-3446. DOI: 10.1109/TTHZ.2017.2757442. (Visited on 16/01/2024).

[23] U. Klein et al. 'The ICI Instrument Onboard MetOp Second Generation'. In: ().

[24] X. Xie et al. 'In-Orbit Calibration of FengYun-3C Microwave Radiation Imager: Characterization of Backlobe Intrusion for the Hot-Load Reflector'. In: *IEEE Journal of Selected Topics in Applied Earth Observations and Remote Sensing* PP (Apr. 2021), pp. 1–1. DOI: 10.1109/JSTARS.2021.3075969.

[25] T. S. Bird. 'Definition and Misuse of Return Loss [Report of the Transactions Editor-in-Chief]'. In: *IEEE Antennas and Propagation Magazine* 51.2 (Apr. 2009), pp. 166–167. ISSN: 1558-4143. DOI: 10.1109/MAP.2009.5162049. (Visited on 27/09/2024).

[26] M. S. V. Dusen. 'PLATINUM-RESISTANCE THERMOMETRY AT LOW TEMPERATURES'. In: *Journal of the American Chemical Society* 47.2 (Feb. 1925), pp. 326–332. ISSN: 0002-7863, 1520-5126. DOI: 10.1021/ja01679a007. (Visited on 07/10/2024).

[27] J. Wu. *A Basic Guide to RTD Measurements*. Tech. rep. SBAA275. Texas Instruments, June 2018. URL: https://docs.ampnuts.ru/ti.com.datasheet/ADS1261/Application_note_SBAA275.PDF.

[28] T. Rose and H. Czekala. *{RPG-HATPRO} Operating Manual*. Mar. 2011. URL: https://www.radiometer-physics.de/download/PDF/Radiometers/HATPRO/Operating_manual.pdf (visited on 19/09/2024).

[29] K. Ostojic et al. 'Blackbody Calibration Targets for the Microwave Sounder Instruments: Control Methods and Modelling Techniques'. In: (July 2021). URL: https://hdl.handle.net/2346/87042 (visited on 19/09/2024).

[30] G. Maschwitz et al. 'Investigation of Ground-Based Microwave Radiometer Calibration Techniques at 530 hPa'. In: *Atmospheric Measurement Techniques* 6.10 (Oct. 2013), pp. 2641–2658. ISSN: 1867-8548. DOI: 10.5194/amt-6-2641-2013. (Visited on 21/09/2024).

[31] S. Crewell and U. Löhnert. 'Accuracy of Cloud Liquid Water Path from Ground-based Microwave Radiometry 2. Sensor Accuracy and Synergy'. In: *Radio Science* 38.3 (June 2003), 2002RS002634. ISSN: 0048-6604, 1944-799X. DOI: 10.1029/2002RS002634. (Visited on 24/09/2024).

[32] N. Patel et al. 'Evaluation of the Amazon Rain Forrest as a Distributed Target for Satellite Microwave Radiometer Calibration'. In: *2006 IEEE International Symposium on Geoscience and Remote Sensing*. July 2006, pp. 85–88. DOI: 10.1109/IGARSS.2006.27. (Visited on 21/09/2024).

[33] M. J. Burgdorf, S. A. Buehler and M. Prange. 'Calibration and Characterization of Satellite-Borne Microwave Sounders With the Moon'. In: *Earth and Space Science* 8.7 (2021), e2021EA001725. ISSN: 2333-5084. DOI: 10.1029/2021EA001725. (Visited on 21/09/2024).

[34] B. Yan, C. Cao and N. Sun. 'Effects of Solar Intrusion on the Calibration of the Metop-C Advanced Microwave Sounding Unit-A2 Channels'. In: *Remote Sensing* 16.5 (Jan. 2024), p. 864. ISSN: 2072-4292. DOI: 10.3390/rs16050864. (Visited on 04/06/2024).

[35] R. V. Leslie and M. DiLiberto. *TROPICS Level-1 Radiance Algorithm Theoretical Basis Document*. Tech. rep. TRPCS- ATBD-034. NASA Goddard Earth Science Data Information and Services Center. URL: https://ntrs.nasa.gov/api/citations/20210018919/downloads/TRPCS-ATBD-034_L1rad_V2pt0.pdf (visited on 21/09/2024).

[36] I. Corbella et al. 'One-Point Microwave Radiometer Calibration'. In: *IEEE Geoscience and Remote Sensing Letters* 17.3 (Mar. 2020), pp. 461–463. ISSN: 1545-598X, 1558-0571. DOI: 10.1109/LGRS.2019.2923539. (Visited on 10/01/2024).

[37] C. R. Parashare et al. 'Noise Sources for Internal Calibration of Millimeter-Wave Radiometers'. In: *2014 13th Specialist Meeting on Microwave Radiometry and Remote Sensing of the Environment (MicroRad)*. Mar. 2014, pp. 157–160. DOI: 10.1109/MicroRad.2014.6878930. (Visited on 21/09/2024).

[38] EUMETSAT. *RESOLUTION EUM/C/105/24/Res.I ON THE EUMETSAT POLAR SYSTEM STERNA PROGRAMME*. draft resolution. 2024. URL: https://www.eumetsat.int/media/52140.

[39] *EPS Second Generation - Facts and Figures | EUMETSAT*. URL: https://www-cdn.eumetsat.int/files/2020-04/pdf_br_prgfs02_en.pdf (visited on 21/09/2024).

[40] *Joint Polar Satellite System (JPSS) National Environmental Satellite, Data, and Information Service (NESDIS) Environmental Satellite Processing Center (ESPC) Requirements Document (JERD) Volume 2: Science Requirements*. Tech. rep. JPSS-REQ-1004. National Oceanic and Atmospheric Administration, Apr. 2018. URL: https://www.nesdis.noaa.gov/s3/2022-03/JERDV2_Version_3_Updated_11292019-mcl-FinalDRAFT-mcl.pdf (visited on 21/09/2024).

[41] Y. Shao et al. 'System Design and Technical Characteristics of Fengyun-3E Meteorological Satellite'. In: *Advances in Astronautics Science and Technology* 5 (Aug. 2022). DOI: 10.1007/s42423-022-00128-2.

[42] D. I. Duncan, N. Bormann and E. V. Hólm. 'On the addition of microwave sounders and numerical weather prediction skill'. In: *Quarterly Journal of the Royal Meteorological Society* 147.740 (2021), pp. 3703–3718. DOI: https://doi.org/10.1002/qj.4149. eprint: https://rmets.onlinelibrary.wiley.com/doi/pdf/10.

1002/qj.4149. URL: https://rmets.onlinelibrary.wiley.com/doi/abs/10.1002/qj.4149.

[43] N. B. Katie Lean. *Task 1.1 Evaluation of Initial Future EPS-Sterna Constellations with 50 and 183 GHz*. Text. Oct. 2023. URL: https://www.ecmwf.int/en/elibrary/81511-task-11-evaluation-initial-future-eps-sterna-constellations-50-and-183-ghz (visited on 11/06/2024).

[44] L. Rivoire et al. 'A Global Observing-System Simulation Experiment for the EPS–Sterna Microwave Constellation'. In: *Quarterly Journal of the Royal Meteorological Society* n/a.n/a (). ISSN: 1477-870X. DOI: 10.1002/qj.4747. (Visited on 13/06/2024).

[45] K. Lean et al. *Final Report: Study to Assess Earth Observation with Small Satellites and Their Prospects for Future Global Numerical Weather Prediction*. Text ESA 4000130590/20/NL/IA. Oct. 2022. URL: https://status.ecmwf.int/en/elibrary/81324-final-report-study-assess-earth-observation-small-satellites-and-their-prospects (visited on 01/03/2023).

[46] *Towards EPS-Sterna - Facts and Figures*. Sept. 2023. URL: https://www-cdn.eumetsat.int/files/2023-09/EPS-SternaFactSheet_en.pdf (visited on 23/09/2024).

[47] C. Accadia et al. *An Overview of the EPS Sterna Programme*. Tokyo, June 2024. URL: https://www.eorc.jaxa.jp/IPWG/meetings/tokyo-2024/pdf/Session09/9.2_Overview_EPS_Sterna%20Christophe%20Accadia.pdf (visited on 23/09/2024).

[48] *Contract Signed to Build Arctic Weather Satellite*. URL: https://www.esa.int/Applications/Observing_the_Earth/Meteorological_missions/Arctic_Weather_Satellite/Contract_signed_to_build_Arctic_weather_satellite (visited on 13/06/2024).

[49] R. A. Varley. *The Social and Economic Benefits of EPS-Aeolus and EPS-Sterna*. Tech. rep. EUMETSAT, Nov. 2023.

[50] S. A. Buehler et al. 'A Concept for a Satellite Mission to Measure Cloud Ice Water Path, Ice Particle Size, and Cloud Altitude'. In: *Quarterly Journal of the Royal Meteorological Society* 133.S2 (2007), pp. 109–128. ISSN: 1477-870X. DOI: 10.1002/qj.143. (Visited on 23/09/2024).

[51] 'UK Secures Key Metop Weather Satellite Contract'. In: *BBC News* (July 2013). URL: https://www.bbc.com/news/science-environment-23313153 (visited on 13/06/2024).

[52] *Storm Boris: Italy Braces for Rain as 21 Killed in Europe Floods*. URL: https://www.bbc.com/news/articles/ckgmrnwgm7zo (visited on 04/10/2024).

[53] *Arctic Weather Satellite's First Images Capture Storm Boris*. URL: https://www.esa.int/Applications/Observing_the_Earth/Meteorological_missions/Arctic_Weather_Satellite/Arctic_Weather_Satellite_s_first_images_capture_Storm_Boris (visited on 24/09/2024).

[54] TICRA. *TICRA Tools manual version 24.0*. 2024. URL: https://www.ticra.com/software/all-software/.

[55] **Albers, R.**, A. Emrich and A. Murk. 'Antenna Design for the Arctic Weather Satellite Microwave Sounder'. In: *IEEE Open Journal of Antennas and Propagation* 4 (2023), pp. 686–694. ISSN: 2637-6431. DOI: 10.1109/OJAP.2023.3295390.

[56] **Albers, R.** et al. 'Spillover analysis and mainbeam characterisation of Arctic Weather Satellite radiometer using method of moments'. In: *IEEE Open Journal of Antennas and Propagation* (2024), pp. 1–1. DOI: 10.1109/OJAP.2024.3462601.

[57] J. E. McKay et al. 'Compact Wideband Corrugated Feedhorns With Ultra-Low Sidelobes for Very High Performance Antennas and Quasi-Optical Systems'. In: *IEEE*

Transactions on Antennas and Propagation 61.4 (Apr. 2013), pp. 1714–1721. ISSN: 1558-2221. DOI: 10.1109/TAP.2013.2243097. (Visited on 24/09/2024).

[58] E. P. Cox. 'A Method of Assigning Numerical and Percentage Values to the Degree of Roundness of Sand Grains'. In: *Journal of Paleontology* 1.3 (1927), pp. 179–183. ISSN: 00223360, 19372337. URL: http://www.jstor.org/stable/1298056 (visited on 20/04/2022).

[59] K. Jacob, A. Schroder and A. Murk. 'Design, Manufacturing, and Characterization of Conical Blackbody Targets With Optimized Profile'. In: *IEEE Transactions on Terahertz Science and Technology* 8.1 (Jan. 2018), pp. 76–84. ISSN: 2156-342X, 2156-3446. DOI: 10.1109/TTHZ.2017.2762309. (Visited on 16/01/2024).

[60] **Albers, R.** et al. 'Development of the Onboard Calibration Target for the Arctic Weather Satellite'. In: *IEEE Transactions on Geoscience and Remote Sensing* (2024), pp. 1–1. DOI: 10.1109/TGRS.2024.3436517.

[61] Y. M. Salomon et al. 'Qualification of Acktar Black Coatings for Space Application'. In: (). URL: http://esmat.esa.int/materials_news/isme09/pdf/4-New/S7%20-%20Miron-Salomon.pdf.

[62] *Industrial Platinum Resistance Thermometers and Platinum Temperature Sensors*. Jan. 2022. DOI: 978-2-8322-1069-2. (Visited on 19/09/2024).

[63] E. J. Wollack et al. 'Electromagnetic and Thermal Properties of a Conductively Loaded Epoxy'. In: *International Journal of Infrared and Millimeter Waves* 29.1 (Jan. 2008), pp. 51–61. ISSN: 1572-9559. DOI: 10.1007/s10762-007-9299-4. (Visited on 15/01/2024).

[64] D. A. Houtz. 'NIST Microwave Blackbody: The Design, Testing, and Verification of a Conical Brightness Temperature Source'. PhD thesis. University of Colorado at Boulder, Jan. 2017.

[65] A. Cox and M. Janezic. 'Preliminary Studies of Electromagnetic Properties of Microwave Absorbing Materials Used in Calibration Targets'. In: *2006 IEEE International Symposium on Geoscience and Remote Sensing*. Denver, CO, USA: IEEE, July 2006, pp. 3467–3469. ISBN: 978-0-7803-9510-7. DOI: 10.1109/IGARSS.2006.889. (Visited on 21/09/2024).

[66] S. Sandeep and A. Gasiewski. 'Effect of Geometry on the Reflectivity Spectrum of Radiometer Calibration Targets'. In: *IEEE Geoscience and Remote Sensing Letters* 11.1 (Jan. 2014), pp. 84–88. ISSN: 1558-0571. DOI: 10.1109/LGRS.2013.2246914. (Visited on 21/09/2024).

[67] D. A. Houtz et al. 'Electromagnetic Design and Performance of a Conical Microwave Blackbody Target for Radiometer Calibration'. In: *IEEE Transactions on Geoscience and Remote Sensing* 55.8 (Aug. 2017), pp. 4586–4596. ISSN: 1558-0644. DOI: 10.1109/TGRS.2017.2694319. (Visited on 21/09/2024).

[68] *Loctite Stycast 2850 FT Datasheet*. May 2019. URL: https://datasheets.tdx.henkel.com/LOCTITE-STYCAST-2850FT-CAT-27-1-en_GL.pdf (visited on 19/09/2024).

[69] *Loctite Stycast 1266 Datasheet*. Dec. 2016. URL: https://webaps.ellsworth.com/edl/Actions/GetLibraryFile.aspx?document=7975&language=en.

[70] *{WAVASORB}-{VHP} Datasheet*. Nov. 2022. URL: https://www.ecanechoicchambers.com/pdf/WAVASORB%20-%20VHP.pdf (visited on 19/09/2024).

[71] *Plastazote LD15 Datasheet*. Jan. 2004. URL: http://www.qualityfoam.com/docs/147_LD15.pdf (visited on 24/09/2024).

[72] G. E. Reesor, I. R. Dagg and S. Mohabir. 'The Complex Dielectric Constant of Liquid Nitrogen in the Region 18 to 26 GHz'. In: *Canadian Journal of Physics* 53.23 (Dec. 1975), pp. 2611–2612. ISSN: 0008-4204. DOI: 10.1139/p75-318. (Visited on 24/09/2024).

[73] D. Winter. *On-Ground Calibration Target for the MetOp-SG Ice Cloud Imager – the TCS from First Idea to Operation*. Oct. 2023. URL: https://indico.esa.int/event/446/contributions/8763/ (visited on 24/09/2024).

Acronyms

LN_2	liquid nitrogen.
ADC	analogue-to-digital converter.
AMSU	Advanced Microwave Sounding Unit.
ARTS	Atmospheric Radiative Transfer Simulator.
ATMS	Advanced Technology Microwave Sounder.
AWS	Arctic Weather Satellite.
BN	boron nitride.
BPF	bandpass filter.
CAD	computer aided design.
CHAMP	Corrugated Horn Analysis by Modal Processing.
CIP	Carbonyl Iron Powder.
CMA	China Meteorological Administration.
DSB	double sideband.
EPP	expanded polypropylene.
EPS	EUMETSAT Polar System.
EPS-Sterna	EUMETSAT Polar System Sterna.
ESA	European Space Agency.
ESTEAM	Electromagnetic Simulation Tool for Electrically large Antenna models.
EUMETSAT	European Organisation for the Exploitation of Meteorological Satellites.
FFS	frequency selective surface.
FWHM	full width half maximum.
FY-3	Fēngyún-3.
GRASP	General Reflector Antenna Software Package.
IAP	Institute of Applied Physics.
ICI	Ice Cloud Imager.
IF	intermediate frequency.
IR	infrared.
JPSS	Joint Polar Satellite System.
LNA	low noise amplifier.
LO	local oscillator.

LSB	lower sideband.
MBE	mainbeam efficiency.
METOP-SG	Meteorological Operational Satellite - Second Generation.
MGSE	mechanical ground support equipment.
MLI	multilayer insulation.
MoM	Method of Moments.
MWHS	Micro-Wave Humidity Sounder.
MWR	Microwave Radiometer.
MWS	Microwave Sounder.
NOAA	National Oceanic and Atmospheric Administration.
NWP	numerical weather prediction.
OBCT	Onboard Calibration Target.
OGCT	Onground Calibration Target.
PEC	perfect electric conductor.
PO	Physical Optics.
POM	polyoxymethylene.
PRT	Platinum Resistance Thermometer.
QON	Quasi-Optical Network.
RF	radio frequency.
RTD	Resistance Temperature Detector.
SSB	single sideband.
TM	transverse magnetic.
USB	upper sideband.
VTT	variable temperature target.

Acknowledgment

I am very grateful to have made it this far, which would not have been possible without the support of a large group of people.

My supervisor Axel Murk for his guidance, support and most of all patience with my questions. It is thanks to his push and faith in me that I got to this point.

Tobias Plüss and Mikko Kotiranta for answering all the questions I was too shy to ask Axel, sharing their measurement expertise and for their very thorough and attentive feedback for any manuscript I showed them, including this one.

Kalle Kempe for his feedback, teaching me more about the receiver side of AWS and the great working atmosphere throughout this project.

Witali, Eric, Alistair, Lorenzo, Yue, Adrianos, Res and Renaud for the great support at work, as well as outside of it.

My parents, who always supported and enabled me. Ihr seid toll.

Rachel for her love and encouragement through all the ups and downs, despite the distance.